Doklady Physics, Vol. 50, No. 2, 2005, pp. 100–105. Translated from Doklady Akademii Nauk, Vol. 400, No. 5, 2005, pp. 630–635.

MECHANICS

Numerical Analysis of the Impact Resistance of Targets and Simple Constructions

G. A. Erokhin[1], G. I. Kanel'[2], V. F. Tolkachev[3], Academician V. E. Fortov[2], and I. E. Khorev[1]

Received July 23, 2004

The problem of the high-velocity interaction of various technogenic bodies with targets and constructions usually consisting of a set of simple targets (layered, screened, and spaced) made of various materials is of special importance in the general problem of high-velocity impact phenomena. It is a scientific basis for solving practical problems concerning the development of double-purpose technologies and permanent advancements in the protection of civil, marine, aviation, and space equipment against penetrating impacts of various technogenic bodies. Complex experimental and numerical investigations into the damages caused to finite-thickness targets by projectiles show that mechanisms of the destruction of targets change significantly with variation in the initial conditions of interaction (increase in the collision velocity of bodies, change in the materials of targets and projectiles, their shape, etc.) [1]. Since a high-velocity impact proceeds very quickly (over a time period of about 10^{-4}–10^{-7} s) and results in destructive action, experimental information on the dynamics of the entire impact process is primarily obtained by high-speed optical shooting (ordinary and laser), pulsed multiple radiography [2], and recording of pressures and velocities by differential laser interferometry, manganin, capacity, and piezoelectric and electret sensors [3]. In addition, mathematical simulation by modern numerical methods is an important source of information immediately from any zone of active deformation, prefracture and fracture of materials of interacting bodies [4].

[1] *Tomsk State University of Control Systems and Radioelectronics, pr. Lenina 40, Tomsk, 634050 Russia*
e-mail: khorev@main.tusur.ru

[2] *Research Institute of Applied Mathematics and Mechanics, Tomsk State University, pr. Lenina 36, Tomsk, 634050 Russia*

[3] *Institute of High Temperatures Scientific Association (IVTAN), Russian Academy of Sciences, ul. Izhorskaya 13/19, Moscow, 127412 Russia*
e-mail: fortov@ras.ru

Computer simulation of the interaction of projectiles with targets and simple constructions was performed by the numerical finite-element method, which was efficiently applied to various impact problems [5]. The physical–mathematical model of colliding solids that is used in this work is generally represented by a compressible strong medium whose behavior under extreme impact loads is described by a broadband semiempirical equation of state [6], elastoplastic model, dynamic yield stress, shear modulus, and constants of the kinetic fracture model [7]. The last model describes the local formation, development, and target evolution of microdamages, which continuously change the properties of the materials in contact and induce a relaxation of stresses.

The spall–shear fracture process was simulated based on the concept of a continuous accumulation of damages characterized by the specific volume of cracks [7]. The rate of increase in the specific volume of cracks or pores was specified as a function of acting pressure and the volume of damages attained according to relations obtained in [7, 8]. These relations take into account the possibility of partial or complete closure of microdamages upon change in the sign of tensile stresses and the appearance of compressive stresses [9], which is very important for analysis of the perforation of spaced constructions. Step-by-step analysis of contours of the specific volume of cracks (at different times) at the stage of prefracture of materials makes it possible to locally determine the general developmental tendencies of fracture both qualitatively and quantitatively, as well as its mechanism, the local damage degree of a material, and the behavior of the main spall crack and adiabatic shift due to decrease in the strength of the material that is caused by its adiabatic heating [10]. In addition, the formation and evolution of different fracture mechanisms and their interference are revealed. In particular, analysis of a mechanism of the perforation of plates by deformable projectiles revealed that the formation of a separated disc in the upper and lower halves of a plate occurred through different mechanisms [11].

A high-velocity impact is mathematically simulated by a system of equations that describes the unsteady spatial adiabatic motions of a continuum and includes

1028-3358/05/5002-0100$26.00

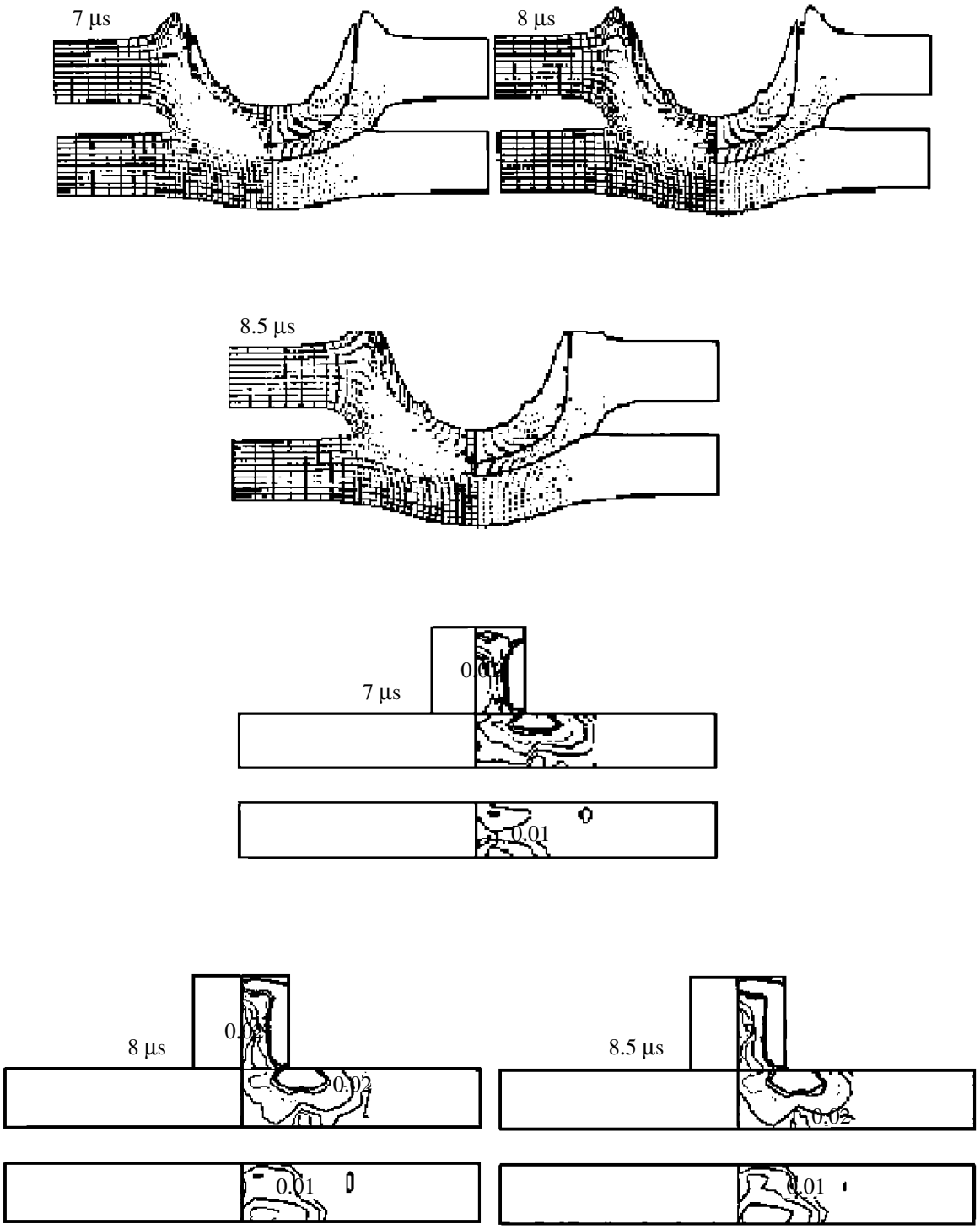

Fig. 1. (Upper part) Chronograms of the 2500-m/s collision of a steel cylinder 8 mm in both diameter and height with a double-layer steel target (the thicknesses of the plates is equal to 5 mm and the gap between them was equal to 3 mm) at times 7, 8, and 8.5 μs. (Lower part) The chronograms of the accumulation of damages in the plates at the same times.

equations for continuity, motion, energy, and change in the specific volume of cracks.

In this work, we numerically analyze the results of the perforation of monolithic finite-thickness targets and simple constructions consisting of separate plates of identical thickness that are made of the same material as a monolithic target. In the general case, such constructions have the same specific weight (weight of a

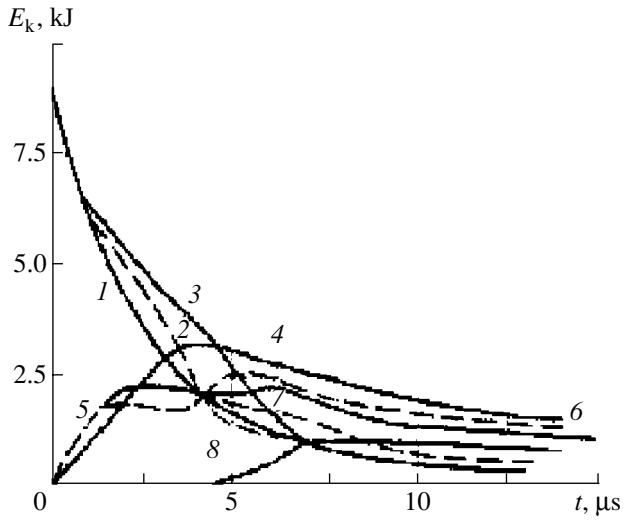

Fig. 2. Time variations in the kinetic energy of the projectile colliding with an initial velocity of 2500 m/s with the (line *1*) monolithic plate and weight-equivalent double-layer target with an interlayer gap of (line *2*) 1 and (line *3*) 3 mm. Time variations in the kinetic energy of the (line *4*) monolithic target and double-layer target with an interlayer gap of (line *5*) 1 and (line *6*) 3 mm. Time variations in the kinetic energy of the (line *7*) first and (line *8*) second plates of the double-layer target with a gap of 3 mm.

construction per unit surface). The numerical scheme for the realization of the finite element method for substantially unsteady problems in the mechanics of a deformable solid is taken from [4]. The velocity at which a projectile penetrates behind the back surface of the last target of the construction with a certain velocity that induces a minimum behind-target shock effect (velocity of about 50 m/s) is generally taken as the limiting velocity of the perforation of a separate target or spaced construction. In this work, we analyze the results from the perforation of spaced targets, because screened targets were considered in [11] and their efficiency is based on the Whipple shield [12]. It is based on the use of thin screens that are placed in front of the basic target and that give rise to the intense fragmentation of projectiles into smaller fragments upon high-velocity interaction. This leads to a dispersion of impact momentum over the larger surface of the basic target and, finally, to a significantly smaller penetration (perforation thickness). The protection of spacecrafts with thin screens was practically implemented in the Vega international project [13].

For spaced targets for which the distance between plates does not noticeably affect the perforation process in contrast to the discontinuity in the denseness of materials, numerical calculations show and experiments corroborate that a monolithic steel plate is the most efficient protection against high-strength (undeformable) fragments. The latter ensures maximum resistance to an impressing projectile (maximum absorption of the kinetic energy of a fragment) compared to any weight-equivalent spaced target consisting of two, three, etc. components with the same physical and mechanical characteristics. The result is different for the penetration of compact deformable elements into such targets [14].

We simulate the interaction of a steel cylinder 8 mm in both diameter and height with targets consisting of one, two, three, etc. steel layers with a yield stress of 10.1×10^2 MPa and a shear modulus of 7.9×10^2 MPa. Figure 1 (the upper part) shows the chronograms calculated for the process of impressing a fragment in a double-layer construction consisting of two plates 5 mm thick with a gap of 3 mm between them. The initial collision velocity was equal to 2500 m/s. The configurations of the interacting bodies correspond to times 7, 8, and 8.5 μs. Analysis of the process of the perforation of both plates, the step-by-step penetration of the deformed projectile into the first and second plates, and the accumulation of damages in them shows that the fracture of the plates occurs via different mechanisms. Figure 1 (lower part) shows the chronograms of the accumulation and evolution of damages in the projectile and both plates at the same times 7, 8, and 8.5 μs, which are discrete (drawn with a certain step) contours of the specific volume of cracks. More detailed analysis of the prefracture of both plates shows that the first plate breaks through the knockout of a disc whose diameter is only slightly larger than the diameter of the deformed projectile [9]. The separation of the disc is completed after the confluence of the fracture nuclei propagating from the front and back surfaces of the plate. Parametric calculations show that the knockout of the disc (adiabatic shift) is accompanied by a considerable release of thermal energy due to intense shear strains in the upper half of the plate. This release gives rise to the local heating of the material in this domain, which is accompanied by a local decrease in the strength of the medium. The fracture of the second plate, which is subjected to tension for nearly the entire interaction process, occurs due to the development of cracks, which initially arise near the symmetry axis on the back surface under the action of rarefaction waves. Therefore, the energy required for the perforation of the second plate in the construction is higher than that required for the first plate. This property represents one of the main reasons why a target consisting of two plates of the same thickness displays greater efficiency than a monolithic target or any other spaced target consisting of three or more components. In particular, the velocity of the deformed projectile behind the target is equal to 45, 75, and 90 m/s when the above compact steel projectile with a velocity of 2500 m/s collides with a double-layer spaced steel target, monolithic target, and triple-layer spaced target, respectively.

To analyze mechanisms of the perforation of monolithic and double-layer spaced targets in detail, we draw a number of parametric dependences characterizing the development of the penetration process. In particular, Fig. 2 shows time variations in the kinetic energy of the

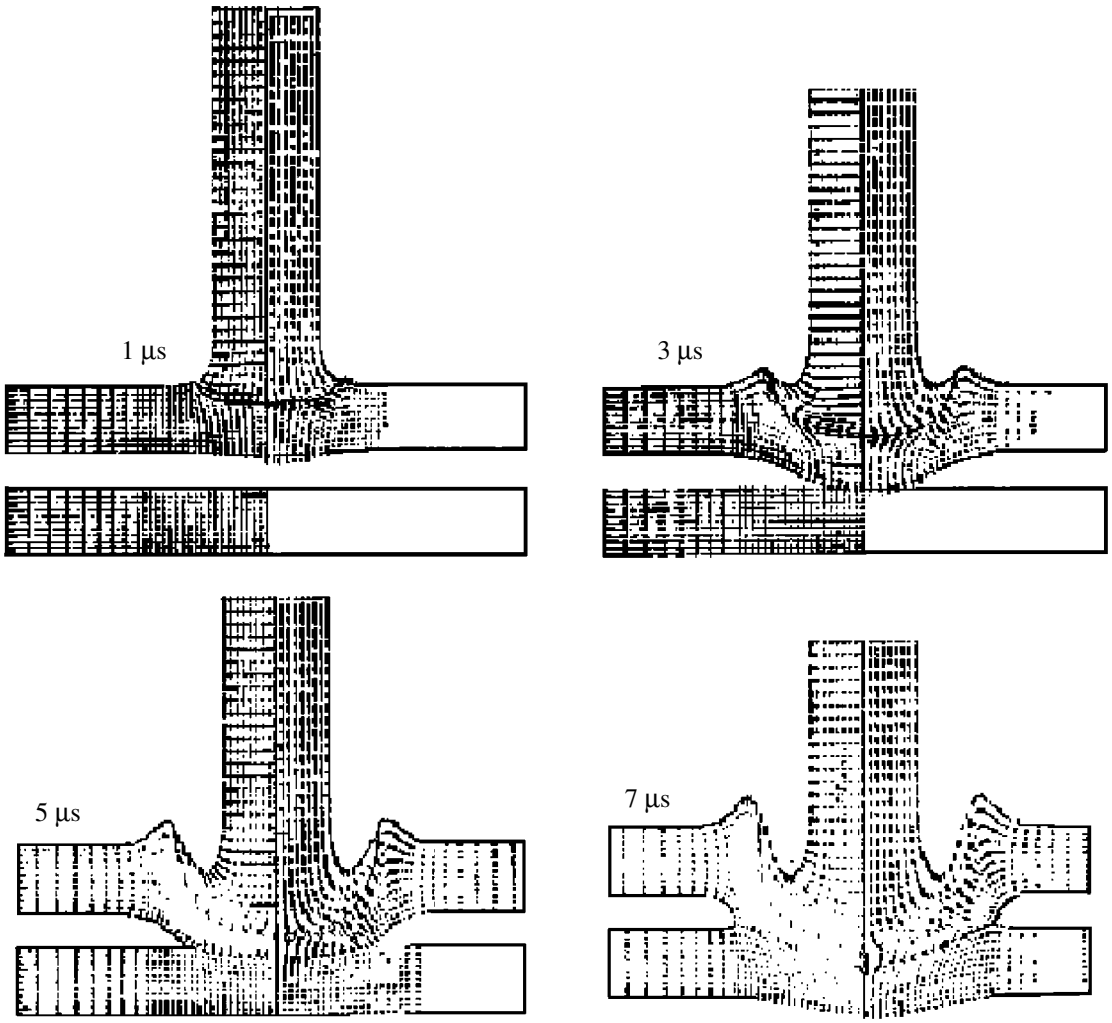

Fig. 3. Chronograms for the penetration of the extended cylindrical steel projectile with an initial velocity of 2500 m/s into the double-layer target at times 1, 3, 5, and 7 μs.

projectile colliding with a velocity of 2500 m/s with the (line *1*) monolithic plate and weight-equivalent double-layer target with an interlayer gap of (line *2*) 1 and (line *3*) 3 mm. In addition, Fig. 2 shows time variations in the kinetic energy of the (line *4*) monolithic target and double-layer target with an interlayer gap of (line *5*) 1 and (line *6*) 3 mm change. Time variations in the kinetic energy of the (line *7*) first and (line *8*) second plates of the double-layer target with a gap of 3 mm are also shown. The kinetic energy of the projectile is first lost upon collision with the monolithic plate. However, after interactions between the plates of the target, the values of the kinetic energy of the projectile begin to approach each other. For the double-layer target with a gap of 1 and 3 mm, approaching occurs to 4 and 7 μs, respectively. Lines *4–6* show that the kinetic energy acquired by the double-layer target is larger than that acquired by the monolithic plate for nearly the entire interaction process. Therefore, double-layer targets generally provide for more efficient protection. The impact resistance of targets decreases with an increase in the number of plates in the mass-equivalent construction, because the spall mechanism of the fracture of individual plates is nearly absent in this case.

Similar numerical investigations show that a triple-layer spaced construction provides for the most efficient protection against the penetration of an extended deformable projectile with an elongation of about 10 (the ratio of the cylinder length to its diameter) as compared to a mass-equivalent continuous monolithic construction or any other spaced construction. In this case, the gain in limiting penetration velocity reaches 10%. Figure 3 shows the chronograms for the penetration of the extended cylindrical steel projectile with an initial velocity of 2500 m/s into the spaced construction consisting of two plates of the same thickness at times 1, 3,

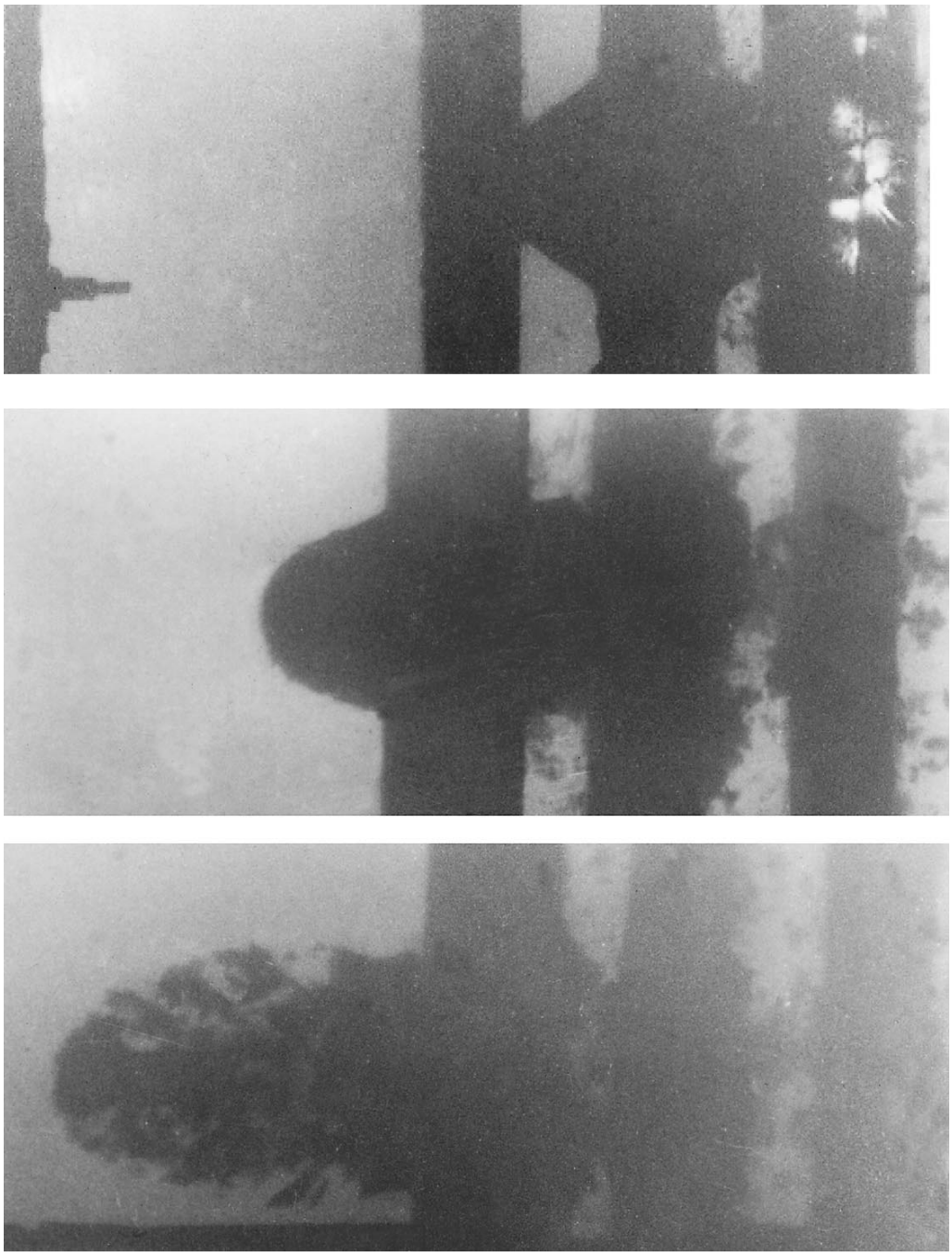

Fig. 4. X-ray patterns for the penetration of the projectile (elongation of 10) with an initial velocity of 2016 m/s into the spaced construction consisting of three steel plates of the same thickness at times 23, 29, and 40 μs.

5, and 7 μs. Theoretical investigations are compared with basic experiments carried out with various combinations of colliding bodies on special racks including powder and light-gas ballistic setups, a target setup with an x-ray pulsed system of detecting the behavior of colliding bodies, and equipment for the storage of necessary samples [15]. Figure 4 shows X-ray patterns for the penetration of the projectile (elongation of 10) with an initial velocity of 2016 m/s into the spaced construction consisting of three steel plates of the same thickness at times 23, 29, and 40 μs. They show that the velocity of the projectile residual behind the target is minimal as compared to the perforation of the continuous target and target consisting of two plates of the same thickness (velocities 650, 740, and 710 m/s, respectively).

Analysis of the problem of the collision of projectiles with various elongations with combined (layered–

spaced) constructions for the normal impact and particularly oblique impact is more complicated. Experimental and numerical investigations of such phenomena are complicated and expensive. They will be conducted step-by-step.

ACKNOWLEDGMENTS

This work was supported by the Russian Foundation for Basic Research, project no. 03-01-00386.

REFERENCES

1. I. E. Khorev, Khim. Fiz. **21** (9), 16 (2002).
2. *Ballistic Setups and Their Application in Experimental Investigations*, Ed. by N. A. Zlatina and G. I. Mishina (Nauka, Moscow, 1974) [in Russian].
3. G. I. Kanel', S. V. Razorenov, A. V. Utkin, and V. E. Fortov, *Shock–Wave Phenomena in Condensed Media* (Yanus-K, Moscow, 1996) [in Russian].
4. G. R. Johnson, J. Appl. Mech. **44** (1), 95 (1977).
5. I. E. Khorev and V. A. Gorel'skiĭ, in *Proceedings of 2nd All-Union Conference on Detonation* (Otd. Inst. Khim. Fiz. AN SSSR, Chernogolovka, 1981), Issue 2, p. 149 [in Russian].
6. A. V. Bushman and V. E. Fortov, Usp. Fiz. Nauk **140** (2), 177 (1983) [Sov. Phys. Usp. **26**, 465 (1983)].
7. G. I. Kanel' and V. V. Shcherban', Fiz. Goreniya Vzryva **5** (4), 93 (1980).
8. G. I. Kanel', S. G. Sugak, and V. E. Fortov, Probl. Prochnosti, No. 8, 40 (1983).
9. A. N. Dremin, I. E. Khorev, V. A. Gorel'skiĭ, and V. F. Tolkachev, Dokl. Akad. Nauk SSSR **290** (4), 848 (1986) [Sov. Phys. Dokl. **31**, 841 (1986)].
10. I. E. Khorev and V. A. Gorel'skiĭ, Dokl. Akad. Nauk SSSR **271** (3), 623 (1983) [Sov. Phys. Dokl. **28**, 588 (1983)].
11. A. V. Radchenko, V. E. Fortov, and I. E. Khorev, Dokl. Akad. Nauk **389** (1), 49 (2003) [Dokl. Phys. **48**, 126 (2003)].
12. F. I. Whipple, *Vistas in Astronautics 1958* (Pergamon, New York, 1958), pp. 115–119.
13. V. E. Fortov, Priroda, No. 3/4, 146 (1996).
14. V. A. Gorel'skiĭ, A. V. Radchenko, and I. E. Khorev, Izv. Akad. Nauk SSSR, Mekh. Tverd. Tela **3** (7), 185 (1988).
15. V. F. Tolkachev, A. A. Konyaev, A. G. Nazarov, and I. E. Khorev, in *Investigations on Ballistics and Adjacent Problems of Mechanics* (Izd. Tomskogo Universiteta, Tomsk, 1997), p. 70 [in Russian].

Translated by R. Tyapaev

Doklady Physics, Vol. 50, No. 2, 2005, pp. 106–111. Translated from Doklady Akademii Nauk, Vol. 400, No. 6, 2005, pp. 758–763.

MECHANICS

Model of the Gravitational-Tidal Mechanism of Exciting Oscillations of the Earth's Pole

L. D. Akulenko*, S. A. Kumakshev*, and Yu. G. Markov**

Presented by Academician V.V. Kozlov June 29, 2004

Received July 5, 2004

The perturbed rotational–vibrational motion of the Earth in the gravitational fields of the Sun and Moon has been investigated using the linear mechanical model of a viscoelastic solid. The tidal mechanism of exciting the oscillations of the poles, i.e., the angular-velocity vector in the Earth-fixed coordinate system, has been revealed. It is attributed to the rotational–translational motion of the Earth–Moon barycenter around the Sun. It has been found that the basic characteristics of the oscillations do not significantly change over time intervals much longer than the period of the precession of the Earth's axis. A simple mathematical model involving two frequencies, Chandler and annual, has been developed by the celestial mechanics methods. It is adequate to the astronomical measurements of the International Earth Rotation Service (IERS). The parameters of the model have been fitted by the least squares method with the use of spectral analysis of IERS data. A statistically convincing interpolation of the process has been obtained over time intervals from several months to 15–20 yr. A precision forecast for 0.5–1 yr and a reliable forecast for 1–3 yr, which are corroborated by observations for several recent years, are presented for the first time. The results are of theoretical interest for geodynamics and celestial mechanics, and they are important for applications in astrometry, navigation, and geophysics.

1. The very complex process of pole oscillations includes components with strongly different frequency and amplitude characteristics [1–6]. In particular, the small oscillations of the angular-velocity vector in the Earth-fixed coordinate system (reference system) involve the main component with an amplitude of 0.20″–0.25″ and a period of about 430–440 sidereal days (S. Chandler, 1891). It was necessary to explain the strong deviation of the Chandler period from the value predicted by the rigid-body theory (Euler precession period of 305 days). Such an explanation was partially given using the model of the deformable Earth [2–6]. A noticeable component with an amplitude of 0.07″–0.08″ and a period of 1 yr (about 365.25 sidereal days) was found to exist (as noted by Chandler). The observed oscillations of the pole are beating. The pole motion trajectory on the ground is a spiral folding and unfolding with a period close to 6 yr.

The analysis and forecast of the pole trajectory are of considerable interest in scientific and application aspects. The development of a precision theoretical model of the rotation of the deformable Earth, the determination of its parameters on the basis of IERS data, and a reliable forecast of pole motion are very important for navigational purposes over time intervals sufficiently long for practical goals and for investigation of astronomical, geodynamical, and geophysical problems [1–6].

The rotation of the deformable Earth and oscillations of its pole are described in a simplified mechanical model of a viscoelastic body [7]. To include gravitational-tidal actions, the planet can be treated as an almost axisymmetric two-layer body consisting of the rigid core (ball) and viscoelastic mantle. Any complication of the model of the Earth's shape is not justified, because the required geometric and physical characteristics of the planet cannot be determined by statistically processing indirect measurement data with the required accuracy and completeness. The obvious, logically justified point of view is that the complexity of the model must strictly correspond to the problem under consideration and measurement accuracy. Comparison with measurements and further analysis show that the accepted simplifications are justified.

At the initial stage of investigation of the pole motion and its evolution under the action of perturbing moments, a spatial variant of the two-body problem is considered [7, 8]. The center of mass of the deformable planet (Earth) and pointlike satellite (Moon) rotate about the common center of mass (barycenter), which moves along an elliptic orbit around the Sun.

* *Institute for Problems in Mechanics, Russian Academy of Sciences, pr. Vernadskogo 101-1, Moscow, 119526 Russia*
e-mail: kumak@ipmnet.ru

** *Moscow State Aviation Institute (University of Aerospace Technology), Volokolamskoe sh. 4, Moscow, 125080 Russia*

1028-3358/05/5002-0106$26.00

On the basis of asymptotic analysis of equations of motion in the osculating variables action–angle, the stable characteristics of the rotational–vibrational motion of the deformable Earth with respect to the center of mass are determined in the quasi-static approximation. The refined periods (frequencies) of the axial rotation and Chandler oscillation are found and compared with the spectral-analysis data [1, 2]. The amplitudes of the natural oscillations of the angular-velocity vector in the Earth-fixed coordinate system are estimated and compared with observable values.

A first-approximation mathematical Chandler model and annual oscillations of the pole under the action of gravitational-tidal forces from the Sun and Moon is developed on the basis of Euler's kinematic equations and Euler–Liouville dynamic equations. The parameters of motion are numerically determined by the least squares method with the use of the daily measurement data, and the results are given in conclusion. Moreover, the trajectories of the Earth's pole are plotted, and a forecast of this motion is given in comparison with the IERS astronomical data [1].

2. To develop a mathematical model of the perturbed rotation of the deformable Earth with respect to the center of mass, we represent equations in the form of the classical Euler–Liouville dynamic equations with the variable tensor of inertia J [2–6, 8, 9]

$$J\dot{\boldsymbol{\omega}} + \boldsymbol{\omega} \times J\boldsymbol{\omega} = \mathbf{M}, \quad \boldsymbol{\omega} = (p, q, r)^T,$$
$$J = J^* + \delta J, \quad J^* = \text{const}, \quad J^* = \text{diag}(A^*, B^*, C^*), \quad (1)$$
$$\delta J = \delta J(t), \quad \|\delta J\| \ll \|J^*\|.$$

Here, $\boldsymbol{\omega}$ is the angular velocity in the coordinate system fixed to the Earth in 1900 (reference system [5]), which approximately coincides with the principal central axes of inertia J^* of the "frozen" Earth including the "equatorial bulge" [1–7]. Additional perturbation terms, which appear due to the differentiation of the kinetic-moment vector of the deformable Earth, are assigned to the perturbing force moment $\mathbf{M}$ with a very complex structure. It is thought that small variations in the tensor of inertia δJ can involve various harmonic components associated with the effect of diurnal solar and lunar gravitational tides and maybe other components (annual, semiannual, monthly, semidiurnal, etc. [1–5]). Gravitational-tidal actions with an annual period and a period close to the Chandler period (see below) are taken as the basic factors of perturbing external force moments $\mathbf{M}$ inducing nutations. We first discuss a simple mechanism of generation and support of annual nutations. Euler kinematic equations specifying the orientation of the Earth-fixed axes with respect to the orbital coordinate system have the form [8, 9]

$$\dot{\theta} = p\cos\varphi - q\sin\varphi - \omega_0(\nu)\sin\psi,$$
$$\dot{\nu} = \omega_0(\nu) = \omega_*(1 + e\cos\nu)^2,$$
$$\dot{\psi} = \frac{p\sin\varphi + q\cos\varphi}{\sin\theta} - \omega_0(\nu)\cot\theta\cos\psi, \quad (2)$$
$$e = 0.0167,$$
$$\dot{\varphi} = r - (p\sin\varphi + q\cos\varphi)\cot\theta + \omega_0(\nu)\frac{\cos\psi}{\sin\theta}.$$

Here, $\nu(t)$ is the true anomaly, e is the orbit eccentricity, and ω_* is the constant determined by the gravitational and focal parameters. When system of equations (1) and (2) is studied for the case corresponding to the motion of the pole, those terms in Eqs. (2) that are proportional to ω_0 are much larger than p and q (by a factor of about 300), and they are determining for $\dot{\theta}$ and $\dot{\varphi}$. This important property was not mentioned in the published works, and the above terms were disregarded without appropriate justification (orbital and rotational motions are separated) [1–6].

3. Let us consider the annual component of the oscillations of the Earth's pole. The components of the gravitational-force moment from the Sun have the structure $M^S_{p,q} \sim \sin\theta\cos\theta$ [9]. Analysis of expressions $M^S_{p,q}$ shows that there are annual perturbation components that are associated with the terms containing products of the direction cosines. In the first approximation (for $p = q = 0$), they are calculated by integrating Eqs. (2)

$$r = r^0, \quad \varphi \approx rt + \varphi^0, \quad \nu \approx \omega_* t + \nu^0,$$
$$\cos\theta(\nu) = a(\theta^0, \psi^0)\cos\nu,$$
$$\theta(0) = \theta^0 = 66°33', \quad 0.4 \le a \le 1, \quad 0 \le \psi^0 \le 2\pi, \quad (3)$$
$$\cos\theta\sin\theta = b(\theta^0, \psi^0)\cos\nu + d\cos 3\nu + \ldots,$$
$$0.4 \le b \le \frac{4}{3\pi}, \quad |d| \ll 1.$$

The second and higher harmonics of ν provide values that are equal to 0.001–0.01 of the main components. For this reason, they are disregarded. The quantity $B^*–A^*$ is also much lower than $C^*–A^*$ (by a factor of about 160). Estimating terms of Eqs. (1) for p and q with allowance for Eqs. (3) after averaging over the fast

phase φ, we arrive at the simplified model

$$\begin{gathered}\dot p + N_p q = \kappa_q r^2 + 3b\omega_*^2\chi_p^{\mathrm{S}}\cos\nu,\\ N_{p,q} \approx N = \frac{2\pi}{T_1} \approx (0.84\text{–}0.85)\omega_*,\\ \dot q - N_q p = -\kappa_p r^2 - 3b\omega_*^2\chi_q^{\mathrm{S}}\cos\nu,\\ p(0) = p^0, \quad q(0) = q^0.\end{gathered} \tag{4}$$

Here, κ_p and κ_q are the average values of $\dfrac{\delta J_{pr}}{B^*}$ and $\dfrac{\delta J_{qr}}{A^*}$, which can be slow-varying functions. The quantities χ_p^{S} and χ_q^{S} are obtained by φ-averaging the coefficients of $\cos\nu$ in the components of the Sun gravitational-force moment.

Moon gravitational-force moments with a monthly period of 27.55 days are disregarded because their effect on nutations is relatively small due to significant difference in frequencies. These effects become important only for detailed analysis of the extrema of the pole deflection in each component. The effect of monthly perturbations is most pronounced in beating (minimum oscillation amplitudes).

The right-hand sides of Eq. (4) explicitly involve an annual-period harmonic action that explains the mechanism of nutations detected by the IERS observations. The sensitivity of the $\kappa_{p,q}$ coefficients is five orders of magnitude higher than the sensitivity of $\chi_{p,q}^{\mathrm{S}}$. This circumstance is a reason for the geophysical seasonal treatment of the annual component of oscillations. However, the explicit regular mechanism of an annual (force–moment) action with an estimated required amplitude of $M_h \sim 10^{20}$ kg m^2 s^{-2} caused by internal geophysical factors (atmospheric actions, oceanic flows, seasonal phenomena on the ground, etc.) seems to be invalid in the mechanical aspect. The spectral analysis of the annual component of the oscillations (the sharpness of the peak in the spectral density of time series), as well as analysis of the phase shifts of various processes, shows that the geophysical interpretation is invalid [2].

4. Let us analyze a mechanism of excitation of the pole oscillations with a frequency close to the Chandler frequency. The potential of the lunar gravitational-tidal action involves components with the diurnal period and six-year modulation [2–6] caused by the precession of its orbit. Taking into account the annual motion of the barycenter of the Earth–Moon system, the projections of the force moment onto the Earth-fixed axes can be represented in the following form similar to $M_{p,q}^{\mathrm{S}}$:

$$\begin{aligned}M_p^{\mathrm{M}} &= [Q_p\cos(\varphi - l) - Q_q\sin(\varphi - l)]\cos\theta\sin\theta,\\ M_q^{\mathrm{M}} &= [Q_p\sin(\varphi - l) + Q_q\cos(\varphi - l)]\cos\theta\sin\theta.\end{aligned} \tag{5}$$

Here, φ is the angle defined according to Eq. (3), l is the average longitude of the Moon, and $Q_{p,q}$ are the components of the tidal force moment in the barycentric rotating coordinate system. They are expressed in terms of unknown gravitational-tidal coefficients $X_{p,q}^{\mathrm{M}}$ and the measurable angle ψ_{M} of the lunar–solar precession as

$$\begin{gathered}Q_p = X_p^{\mathrm{M}}\cos\psi_{\mathrm{M}}, \quad X_{p,q}^{\mathrm{M}} = X_{p,q}^{\mathrm{M}}(\varphi - l),\\ Q_q = X_q^{\mathrm{M}}\cos\psi_{\mathrm{M}}, \quad \psi_{\mathrm{M}} = p_{\mathrm{M}} + \Omega_{\mathrm{M}}.\end{gathered} \tag{6}$$

Here, p_{M} is the average longitude of the perigee of the Moon's orbit and Ω_{M} is the longitude of the ascending node of the Moon. The periods of varying p_{M} and Ω_{M} are equal to 8.85 and 18.61 yr, respectively. The angular variable ψ_{M} is representable as

$$\begin{gathered}\psi_{\mathrm{M}} = \omega_{\mathrm{M}}\tau + \psi_{\mathrm{M}}^0, \quad \omega_{\mathrm{M}} = \frac{2\pi}{8.85} + \frac{2\pi}{18.61} \simeq \frac{2\pi}{6.00},\\ \psi_{\mathrm{M}}^0 \approx \mathrm{const},\end{gathered} \tag{7}$$

where τ is measured in years.

The substitution of Eqs. (3), (6), and (7) into Eq. (5) yields the multifrequency expressions for $M_{p,q}^{\mathrm{M}}$ with significantly different periods that are close to day, year, and six years. This circumstance allows both the application of the asymptotic methods of the separation of motions and averaging of the corresponding coefficients $X_{p,q}^{\mathrm{M}}\cos(\varphi - l)$ and $X_{p,q}^{\mathrm{M}}\sin(\varphi - l)$ with respect to the fast phase $\varphi - l$.

As a result, we obtain the following equations of the pole oscillations under the action of the force moments given by Eqs. (5) of form (4)

$$\begin{gathered}\dot p + Nq + \sigma p = \mu_p\cos\alpha, \quad \alpha = \nu - (\psi_{\mathrm{M}} + \beta),\\ \dot q - Np + \sigma q = \mu_q\cos\alpha, \quad \mu_{p,q}, \beta \approx \mathrm{const}.\end{gathered} \tag{8}$$

The quasi-constant parameters $\mu_{p,q}$ and β are expressed in terms of the above average coefficients $X_{p,q}^{\mathrm{M}}$. In Eqs. (8), similar terms with a phase of $\nu + (\psi_{\mathrm{M}} + \beta)$ are rejected, and dissipative terms with a coefficient of σ are introduced. This is fundamentally important for the reported procedure of developing the gravitational-tidal model of oscillations with the Chandler period T_1. According to the spectral-analysis data

and calculations, T_1 is estimated as T_1 = 410–440 d (average value $T_1 \approx 433 \pm 2$ d); i.e., the coefficient N of the frequency of the natural nutations is equal to $N \simeq$ 0.89–0.83 (average value $N \simeq$ 0.845–0.850). The frequency N of natural oscillations of system (8) is independent of a quite small σ value. It should be taken into account due to the resonant action of the gravitational-force moments with a phase of $\alpha \simeq \frac{5}{6}\tau + \alpha^0$ and a frequency of $\gamma \simeq 0.833$. Terms rejected in Eqs. (8) have the same amplitude and phase varying with a frequency of $\frac{7}{6} \approx 1.17$, which is far from eigenvalue N. The amplitudes of steady-state oscillations with the indicated frequencies are significantly different (by two orders of magnitude).

The desired quasi-stationary solution of system (8) has the form

$$\begin{aligned} p_{\text{ch}} &= d^{-1}(a^c \cos\alpha + a^s \sin\alpha), \\ q_{\text{ch}} &= d^{-1}(b^c \cos\alpha + b^s \sin\alpha), \end{aligned} \tag{9}$$

where the coefficients d, $a^{c,s}$, and $b^{c,s}$ are defined in the standard manner. The structural properties of the model given by Eqs. (5)–(8) are manifested approximately for $\delta = N - \gamma$ and σ values much smaller than N and γ, respectively. In this case, we obtain the expressions

$$\begin{aligned} a^c \approx 2N^2(\sigma\mu_p + \delta\mu_q), \quad a^s \approx 2N^2(\delta\mu_p - \sigma\mu_q), \\ b^c \approx -a^s, \quad b^s \approx a^c; \quad d \simeq 4N^2(\delta^2 + \sigma^2). \end{aligned} \tag{10}$$

The amplitude of the steady-state oscillations have small modulation with a period of about 0.6 yr corresponding to a frequency of $2\gamma \approx 1.7$, which is explicitly observed on the spectral-density line [1]. In the first approximation in δ and σ, the amplitude A_{ch} of the oscillations with a frequency of γ close to the Chandler frequency is estimated as

$$A_{\text{ch}} = \sqrt{p_{\text{ch}}^2 + q_{\text{ch}}^2} \approx \frac{1}{2}(\mu_p^2 + \mu_q^2)^{1/2}(\delta^2 + \sigma^2)^{-1/2}. \tag{11}$$

According to Eqs. (9)–(11), the components and amplitude of the oscillations are highly sensitive to variations in the frequency difference δ and dissipation factor σ. Structural property (10) of the forced oscillations is similar to that determined previously for the model of the free oscillations with the Chandler frequency, as well as for annual nutations. This property is clearly corroborated [8, 9] by the independent statistical processing of the measurement data and solution to the problem of the model identification, i.e., the determination of unknown coefficients $\frac{a^{c,s}}{d}$ and $\frac{b^{c,s}}{d}$ by the least squares method [10]. Moreover, the amplitude changes in dependence of the composition of used measurements—the length, number of points, and position of the interval of IERS data on the time axis.

5. We present the results of numerical simulation of the pole motion on the basis of linear equations with additive entry of unknown perturbing actions—quasi-static, annual (4), and Chandler (8). The introduced parameters are assumed to be constant over short time intervals (several years). However, the model must be refined for long time intervals of about 10–20 yr or longer: interpolation errors of the quasi-stationary model can be partially compensated by introducing secular terms. The developed theoretical model has restrictions in the accuracy of the approximation of the process and duration of the intervals, which are determined by numerical simulation using the measurement data. The duration of the forecast and its accuracy are significantly determined by the indicated factors.

We present the results of calculations based on a simplified procedure of the least squares method [10]. It is applied to variables $x(\tau)$ and $y(\tau)$ independently in the form of the 6D approximations

$$\begin{aligned} x(\tau) = (\xi, f(\tau)), \quad y(\tau) = (\eta, f(\tau)), \\ \xi = (\xi_1, \xi_2, \ldots, \xi_6)^T, \quad \eta = (\eta_1, \eta_2, \ldots, \eta_6)^T, \\ f(\tau) = (1, \tau, \cos 2\pi N\tau, \sin 2\pi N\tau, \cos 2\pi\tau, \sin 2\pi\tau)^T, \\ N \approx 0.845\text{–}0.850. \end{aligned} \tag{12}$$

The 6D vectors ξ and η must be determined. It is of interest to analyze the efficiency of interpolation and forecast of the pole motion in a very simple mathematical model given by Eqs. (12) with the use of the known daily IERS data [1].

In 2001, we performed the optimum interpolation of the 1994–2000 observation data [7]. The following optimum parameters ξ^* and η^* of model (12) and rms deviations σ_x and σ_y are obtained:

$$\begin{aligned} \xi^* = (0.039, 0.0001, 0.015, 0.161, -0.046, -0.076)^T, \\ \sigma_x = 0.024; \\ \eta^* = (0.334, 0.0005, 0.162, -0.014, -0.068, 0.043)^T, \\ \sigma_y = 0.025. \end{aligned} \tag{13}$$

A biannual forecast of the pole motion (for 2001 and 2002) was given using the interpolation results. The dashed line in Fig. 1 is the theoretical (x^*, y^*) curve, which for convenience is plotted as two annual segments (2001 and 2002). The solid lines are parts of the experimental curve corresponding to the IERS data. Comparison of the measured trajectory of the pole motion with the theoretical trajectory given by Eqs. (12) and (13) shows that the developed model is consistent with the observation data.

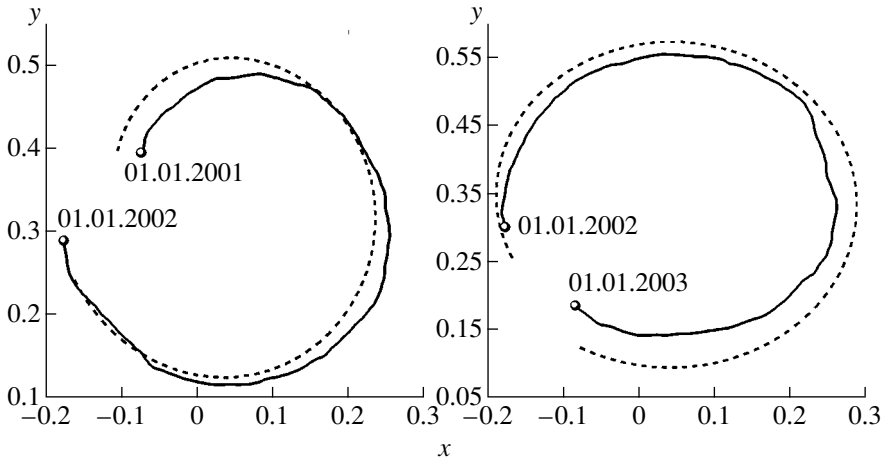

Fig. 1. (Dashed line) Forecast of the Earth's-pole motion for 2001 and 2002 and (solid line) the IERS data. The points mark the beginning and end of a year.

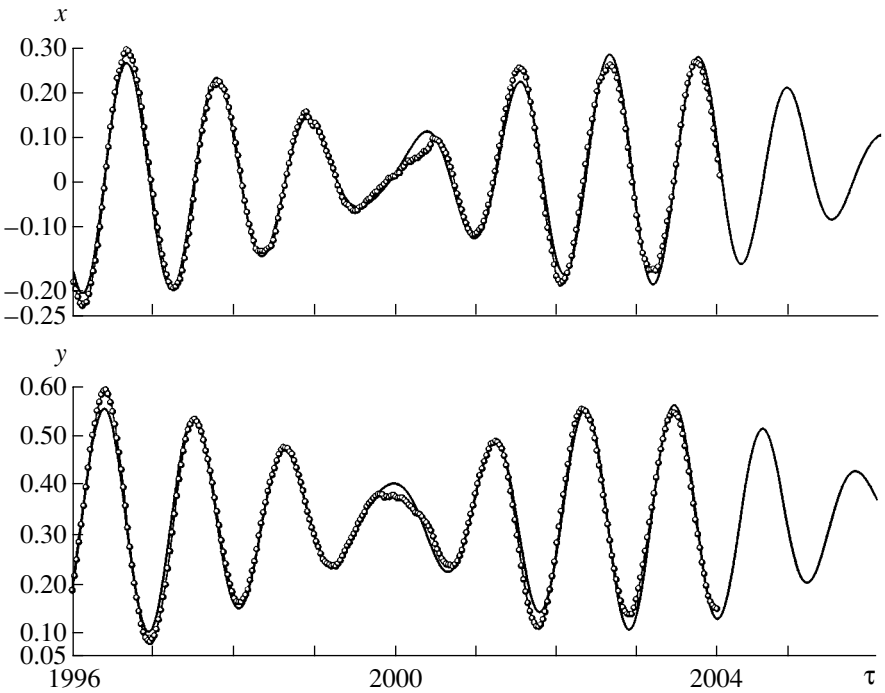

Fig. 2. (Line) Interpolation and forecast of the components of the oscillations of the Earth's pole for 2004 and 2005 as obtained using (points) 1996–2003 IERS data.

Using the operative IERS data, the Washington Naval Observatory forecasts pole motion for 100–150 days (IERS, EOP Product Center, http://hpiers.obspm.fr/eoppc/eop/eopc04/eopc04-xy.gif). The model and procedure accepted by IERS provide an inaccurate and unstable forecast that requires weekly correction.

Figure 2 shows the interpolation of the observed process and a biannual forecast (up to the end of 2005) of pole oscillations. This interpolation and forecast are based on eight-year IERS data (1996–2003). The following optimum parameters ξ^* and η^* and rms deviations σ_x and σ_y have been obtained:

$$\begin{aligned}\xi^* &= (0.0314, 0.0027, -0.1347, -0.0596,\\ &-0.0494, -0.0741)^T, \quad \sigma_x = 0.0175;\\ \eta^* &= (0.3315, 0.001, -0.0613, 0.1341,\\ &-0.0679, 0.0426)^T, \quad \sigma_y = 0.0175.\end{aligned} \tag{14}$$

Comparison of the components of the vectors ξ^* and η^* given by Eqs. (14) shows that the approximate

equalities characterizing the properties of the model are valid.

ACKNOWLEDGMENTS

This work was supported by the Russian Foundation for Basic Research (project nos. 04-02-16303, 02-01-00252, and 02-01-00157) and the Council of the President of the Russian Federation for Support of Young Russian Scientists and Leading Scientific Schools (project nos. NSh-1627.2003.1 and MK-2093.2003.01).

REFERENCES

1. *IERS Annual Reports 2000–2003*, Ed. by W. R. Dick and B. Richter (Verlag des Bundesamts für Kartographie und Geodäsie, Frankfurt am Main, 2001–2003).
2. W. H. Munk and G. J. F. MacDonald, *The Rotation of the Earth* (Cambridge Univ. Press, Cambridge, 1960; Mir, Moscow, 1964).
3. P. Melchior, *Physique at Dynamique Planetaires* (Vander, Bruxelles, 1971; Mir, Moscow, 1975), Vol. 2.
4. H. Moritz and I. I. Mueller, *Earth Rotation: Theory and Observation* (Ungar, New York, 1987; Naukova Dumka, Kiev, 1992).
5. Yu. N. Avsyuk, *Tidal Forces and Natural Processes* (OIFZ RAN, Moscow, 1996) [in Russian].
6. N. S. Sidorenkov, *Physics of Earth's Rotation Instabilities* (Nauka, Moscow, 2002) [in Russian].
7. L. D. Akulenko, S. A. Kumakshev, Yu. G. Markov, and L. V. Rykhlova, Astron. Zh. **79** (1), 81 (2002).
8. L. D. Akulenko, S. A. Kumakshev, Yu. G. Markov, and L. V. Rykhlova, Astron. Zh. **79** (10), 952 (2002).
9. L. D. Akulenko, S. A. Kumakshev, and Yu. G. Markov, Dokl. Akad. Nauk **382** (2), 199 (2002) [Dokl. Phys. **47**, 78 (2002)].
10. V. S. Gubanov, *Generalized Least Squares Method. Theory and Application to Astrometry* (Nauka, St. Petersburg, 1997) [in Russian].

Translated by R. Tyapaev

Doklady Physics, Vol. 50, No. 2, 2005, pp. 112–114. Translated from Doklady Akademii Nauk, Vol. 400, No. 6, 2005, pp. 764–766.

MECHANICS

On the Forcing of an Elastoviscoplastic Material Through an Inflexible Circular Cylindrical Die

L. V. Kovtanyuk

Presented by Academician G.G. Chernyĭ October 23, 2004

Received October 4, 2004

Analytical solutions to similar problems have been found in [1, 2] for the case of viscoplastic flows of a Shvedov–Bingham material. In this paper, we solve the problem, taking into consideration the elastic properties of the material under examination.

1. We assume that a deformable material initially fills in a circular cylindrical die of radius R and length l. The material is in equilibrium under the boundary conditions

$$\sigma_{zz}\big|_{\substack{r=0\\ z=u|_{r=0}}} = -p_0(t), \quad \sigma_{zz}\big|_{\substack{r=0\\ z=l+u|_{r=0}}} = 0, \tag{1}$$

$$u|_{r=R} = 0. \tag{2}$$

Here, σ_{zz} is the component of the stress tensor in the cylindrical coordinates (r, θ, z), with the z axis along the die axis; $u = u_z(r)$ is the only nonzero component of the displacement vector; and $p_0(t)$ is the applied pressure. The initial time of the forcing process coincides with the start of the plastic flow at the boundary $r = R$. Both the stress and strain distributions, as well as the initial moment, are determined by the properties of the material. The material is treated as incompressible, and its viscosity is manifested only in the course of the plastic flow. Following [3, 4], we describe the elastic properties of the material by the tensors in the rectangular coordinates:

$$\begin{aligned} d_{ij} &= \frac{1}{2}(u_{i,j} + u_{j,i} - u_{k,i}u_{k,j}) \\ &= e_{ij} + p_{ij} - \frac{1}{2}e_{ik}e_{kj} - e_{ik}p_{kj} - p_{ik}e_{kj} + e_{ik}p_{ks}e_{sj}, \\ \sigma_{ij} &= -p\delta_{ij} + \frac{\partial W}{\partial d_{ik}}(\delta_{kj} - 2d_{kj}) \quad \text{for} \quad p_{ij} \equiv 0, \\ \sigma_{ij} &= -p\delta_{ij} + \frac{\partial W}{\partial e_{ik}}(\delta_{kj} - e_{kj}) \quad \text{for} \quad p_{ij} \neq 0, \end{aligned} \tag{3}$$

$$\begin{aligned} W &= -2\mu I_1 - \mu I_2 + bI_1^2 + (b-\mu)I_1I_2 - \theta I_1^3, \\ I_1 &= d_{kk}, \quad I_2 = d_{ik}d_{kj}. \end{aligned}$$

Here, d_{ij} is the Almansi strain tensor with reversible and irreversible components e_{ij} and p_{ij}, respectively; σ_{ij} is the stress tensor; p is the hydrostatic pressure; and $W(I_1, I_2)$ is the elastic potential. The potential W is written in Eq. (3) for the case of $p_{ij} \equiv 0$. If $p_{ij} \neq 0$, the elastic potential depends on the invariants J_1 and J_2 of the reversible strain tensor e_{ij} $\left(J_1 = e_{kk} - \frac{1}{2}e_{st}e_{ts},\ J_2 = e_{st}e_{ts} - e_{sk}e_{kt}e_{ts} + \frac{1}{4}e_{sk}e_{kt}e_{tn}e_{ns}\right)$. We choose the invariants J_1 and J_2 such that the Murnaghan formula with $p_{ij} \neq 0$ in the limit of zero plastic strains reduces to the corresponding correct expression. The form of $W(I_1, I_2)$ given above is the Taylor series expansion of this formula in the neighborhood of the free state under the condition of antiplane motion [5]. We take the load function in the form

$$\left|\sigma_i - \eta\varepsilon_i^{\mathrm{p}} - (\sigma_j - \eta\varepsilon_j^{\mathrm{p}})\right| = 2k \tag{4}$$

as the plastic potential. Here, σ_i and $\varepsilon_i^{\mathrm{p}}$ are the fundamental eigenvalues of the stress tensor and the plastic strain rate tensor, respectively; η is the coefficient of viscosity; and k is the yield stress. Expression (4) is a generalization of the known Treska plastic-flow condition to viscoplastic flows. According to [3, 4], the plastic strain rate tensor $\varepsilon_{ij}^{\mathrm{p}}$ is defined as a source in the transport equation for the irreversible strains:

$$\begin{aligned} \frac{dp_{ij}}{dt} &= \varepsilon_{ij}^{\mathrm{p}} - p_{is}r_{sj} - p_{is}\varepsilon_{sj}^{\mathrm{p}} - r_{si}p_{sj} - \varepsilon_{si}^{\mathrm{p}}p_{sj}, \\ r_{ij} &= \frac{1}{2}(v_{i,j} - v_{j,i}) + F_{ij}(\varepsilon_{st}, e_{st}), \\ \varepsilon_{ij} &= \frac{1}{2}(v_{i,j} + v_{j,i}), \quad v_i = \frac{\partial u_i}{\partial t} + v_j u_{i,j}. \end{aligned} \tag{5}$$

The skew-symmetric tensor F_{ij} was defined in [3, 4].

Institute of Automation and Control, Far East Division, Russian Academy of Sciences,
ul. Radio 5, Vladivostok, 690041 Russia
e-mail: byrenin@iacp.dvo.ru

1028-3358/05/5002-0112$26.00

The material remains in elastic equilibrium until the applied pressure reaches the value $p_0 = p_0^*$. At this value, condition (4) with zero ε_i^p is satisfied at the boundary $r = R$. The equilibrium equations are solved in the cylindrical coordinates under boundary conditions (1) with regard to Eqs. (3) and (4). The parameters evaluated for the stress–strain state under consideration take the form

$$u = \frac{k}{2\mu}(R - r^2R^{-1}), \quad p_0^* = 2klR^{-1},$$

$$\sigma_{rr} = \sigma_{\theta\theta} = 2kR^{-1}(z-l) - k^2\mu^{-1}, \ \sigma_{rz} = -krR^{-1}, \quad (6)$$

$$\sigma_{zz} = 2kR^{-1}(z-l) + k^2\mu^{-1}(r^2R^{-2} - 1).$$

For the sake of simplicity, only the dominant nonlinear terms are written in both Eqs. (6) and following expressions.

2. The development of the plastic flow is determined by load pressure $p_0(t)$. At any time, the plastic region is bounded by cylindrical surfaces $r_1(t) \le r \le R$. In the region $r \le r_1(t)$, the strains remain reversible. The moving boundary $r_1(t)$ serves as an interface between the elastic and plastic regions. Neglecting inertial forces, we solve the equilibrium equations in the cylindrical coordinates in region $0 \le r \le r_1(t)$ of zero irreversible strains. As a result, we arrive at the equations

$$p(t) = c_1(t)z - \frac{\mu + b}{8\mu^2}c_1^2(t)r^2 + c_3(t),$$
$$u = \frac{c_1(t)r^2}{4\mu} + c_2(t), \quad v = v_z(r) = \frac{\dot{c}_1(t)r^2}{4\mu} + \dot{c}_2(t). \quad (7)$$

Here, c_1, c_2, and c_3 are unknown functions of time and the point stands for the derivative with respect to time. These functions will be found from the continuity condition at the boundary $r = r_1(t)$ of plastoelastic strains.

It is worth noting that, according to the first of Eqs. (3), the elastic-strain tensor e_{ij} does not coincide with the Almansi strain tensor even in the case of zero irreversible strains ($p_{ij} \equiv 0$). The components of the Almansi tensor satisfy the relations

$$d_{rr} = e_{rr} - \frac{1}{2}e_{rz}^2 = -\frac{1}{2}u_{,r}^2,$$

$$d_{zz} = e_{zz} - \frac{1}{2}e_{rz}^2 = 0, \quad d_{rz} = e_{rz} = \frac{1}{2}u_{,r}, \quad (8)$$

$$e_{rr} = -\frac{3}{2}e_{rz}^2, \quad e_{zz} = \frac{1}{2}e_{rz}^2.$$

The reversible strains e_{rr}, e_{zz}, and e_{rz} describe the deformation field in the plastic region. At the same time, the stress in this region must satisfy plasticity condition (4), which can be rewritten in the form

$$f(\sigma_{rz}, \varepsilon_{rz}^2) = \sigma_{rz}^2 - (k + \eta\varepsilon_{rz}^p)^2 = 0. \quad (9)$$

Therefore,

$$\sigma_{rz} = -k - \eta\varepsilon_{rz}^p. \quad (10)$$

Thus, the associated plastic-flow rule $\varepsilon_{ij}^p = \dfrac{\lambda\partial f}{\partial\sigma_{Ij}}$ is valid if $\lambda = -\varepsilon_{rz}^p(k + \eta\varepsilon_{rz}^p)^{-1}$.

For the stress to be continuous at the boundary of plastoelastic strains, reversible strains must be continuous; therefore, the last two of Eqs. (8) must be satisfied in the plastic region. In this case, it follows from Murnaghan formula (3) for $p_{ij} \ne 0$ that

$$\sigma_{rr} = \sigma_{\theta\theta} = -p_1 - 2(\mu + b)e_{rz}^2,$$
$$\sigma_{zz} = -p_1 - 2(b - \mu)e_{rz}^2, \quad (11)$$
$$\sigma_{rz} = 2\mu e_{rz}.$$

As follows from the kinematics of the motion under consideration, the component ε_{rz}^p should be a function of the only variable r. Therefore, the stress σ_{rz} depends only on r. In this case, it follows from the equilibrium equations

$$\sigma_{rz,r} + \sigma_{zz,z} + r^{-1}\sigma_{rz} = 0,$$
$$\sigma_{rr,r} + \sigma_{rz,z} + r^{-1}(\sigma_{rr} - \sigma_{\theta\theta}) = 0 \quad (12)$$

that σ_{zz}, σ_{rr}, and $\sigma_{\theta\theta}$ are linear functions of z. Solving Eqs. (12), we find

$$\sigma_{rz} = \frac{1}{2c_4(t)r} \quad (13)$$

and, with regard to Eqs. (10) and (13),

$$\varepsilon_{rz}^p = -\frac{c_4(t)}{2\eta}r - \frac{k}{\eta}. \quad (14)$$

In the case under consideration, it follows from Eqs. (3) and (5) that

$$\frac{dp_{rz}}{dt} = \varepsilon_{rz}^p, \quad d_{rz} = e_{rz} + p_{rz},$$

$$v_{,r} = 2\varepsilon_{rz} = \frac{du_{,r}}{dt} = 2\frac{dd_{rz}}{dt} = 2\left(\frac{de_{rz}}{dt} + \varepsilon_{rz}^p\right).$$

Taking into account the boundary condition $v|_{r=R} = 0$ and the continuity condition for displacements at the

plastoelastic boundary, we obtain

$$v = \left(\frac{\dot{c}_4(t)}{4\mu} - \frac{c_4(t)}{2\mu}\right)(r^2 - R^2) - \frac{2k}{\eta}(r - R),$$

$$u = \left(\frac{c_4(t)}{4\mu} - \frac{c_5(t)}{2\eta}\right)(r^2 - R^2) - \frac{2k}{\eta}(r - R)t, \qquad (15)$$

$$c_5(t) = \int c_4(t)dt.$$

Joining the stress, strain, and strain rate tensors at the boundary $r = r_1(t)$, we arrive at the solution

$$c_2(t) = -\frac{c_1(t)R^2}{4\mu} + \frac{c_5(t)}{2\eta}(R^2 - r_1^2) - \frac{2k}{\eta}(r_1 - R)t,$$

$$c_4(t) = c_1(t), \quad r_1(t) = -2ktc_5^{-1}(t).$$

Finally, the functions $c_1(t)$ and $c_3(t)$ are found from conditions (1):

$$c_1(t) = -p_0(t)l^{-1}, \quad c_3(t) = p_0(t)(1 + c_2(t)l^{-1}).$$

If the pressure drop tends to a constant, the elastic region becomes fixed and moves as a whole with a constant velocity.

ACKNOWLEDGMENTS

This work was supported by the Russian Foundation for Basic Research (project nos. 02-01-01134 and 02-01-01128) and the Council of the President of the Russian Federation for Support of Young Russian Scientists and Leading Scientific Schools (project no. NSh-890.2003.1).

REFERENCES

1. V. P. Myasnikov, Prikl. Matem. Tekh. Fiz., No. 2, 79 (1961).
2. G. I. Bykovtsev and A. D. Chernyshov, Prikl. Matem. Tekh. Fiz., No. 4, 94 (1964).
3. A. A. Burenin, G. I. Bykovtsev, and L. V. Kovtanyuk, Dokl. Akad. Nauk **347** (2), 201 (1996) [Phys. Dokl. **41**, 127 (1996)].
4. A. A. Burenin, L. V. Kovtanyuk, and M. V. Polonik, Prikl. Mat. Mekh. **67**, 316 (2003).
5. A. I. Lur'e, *Nonlinear Theory of Elasticity* (Nauka, Moscow, 1980; Elsevier, Amsterdam, 1990).

Translated by V. Chechin

Doklady Physics, Vol. 50, No. 2, 2005, pp. 115–117. Translated from Doklady Akademii Nauk, Vol. 400, No. 6, 2005, pp. 767–769.

MECHANICS

Optimum Regimes of Mass Transfer in Fluid Films

A. A. Rastaturin, E. A. Demekhin, and E. N. Kalaĭdin

Presented by Academician V.A. Babeshko September 23, 2004

Received October 1, 2004

In this paper, a solution is obtained in complete formulation of the problem on heat-and-mass transfer in a flowing fluid film. Solutions are presented for both natural and excited waves. Investigations are carried out for basic regimes of mass transfer in fluid films, and optimum regimes corresponding to the mass-transfer maximum are determined for excited waves.

The investigation of heat-and-mass transfer in fluid films is an important problem of hydromechanics. Large contact-surface area along with low specific fluid-flow rate determine the significant role of fluid films in studies of interphase heat-and-mass transfer. An additional intensification in the transfer process occurs due to wave formation. As follows from the experimental data of [1, 2], wave regimes are capable of enhancing mass transfer by 100 to 400%. All theoretical studies of mass-transfer processes are based on simplified equations for heat-and-mass transfer and on analysis of both a thin boundary concentration layer and other limiting cases [3, 4]. However, these simplifications result in the appearance of a singularity that prevents a solution being obtained for many regimes that are optimum for the mass transfer.

1. We analyze the problem associated with the absorption of slightly soluble gas in a thin film of viscous incompressible fluid flowing over a vertical wall. The film surface is an interface between the liquid and gas phases. For poorly soluble gases, the basic diffusion resistance is concentrated in the liquid phase; therefore, the diffusion process in the gas phase can be ignored.

Under the given assumptions, the diffusion is described by the equation

$$\frac{\partial c}{\partial t} + u\frac{\partial c}{\partial x} + v\frac{\partial c}{\partial y} = \frac{1}{\mathrm{Pe}}\left(\frac{\partial^2 c}{\partial x^2} + \frac{\partial^2 c}{\partial y^2}\right).$$

Here, (u, v) are the components of the velocity vector; $\mathrm{Pe} = \mathrm{Re} \times \mathrm{Sc}$ is the Peclet number (Re and Sc are the Reynolds and Schmidt numbers, respectively); $c = \frac{c_{xy} - c_0}{c_h - c_0}$ is the normalized concentration, where c_{xy} is the concentration at the point (x, y); and c_0 and c_h are the initial and surface concentrations, respectively.

The boundary conditions are

$$y = h(x, t)\colon c = 1, \quad y = 0\colon \frac{\partial c}{\partial y} = 0,$$

$$x = 0\colon c = 0, \quad x = L\colon \frac{\partial c}{\partial x} = 0.$$

The hydrodynamics of the process is described by the set of Kapitza–Shkadov equations averaged over the normal to the flow having the semi-parabolic velocity profile:

$$\frac{\partial q}{\partial t} + \frac{6}{5}\frac{\partial}{\partial x}\frac{q^2}{h} = \mathrm{We}h\frac{\partial^3 h}{\partial x^3} + \frac{3}{\mathrm{Re}}\left(h - \frac{q}{h^2}\right),$$

$$\frac{\partial h}{\partial t} + \frac{\partial q}{\partial x} = 0.$$

The boundary conditions for these equations are

$$x = 0\colon h = 1, \quad q = 1 + F(t);$$

$$x = L\colon \frac{\partial h}{\partial x} = 0, \quad \frac{\partial^2 h}{\partial x^2} = 0,$$

where $q = \int_0^h u\,dy$ is the local flow, We is the Weber number, and $F(t)$ models disturbances at the input. The velocity-vector components have the form

$$u = \frac{3q}{h}\left(\frac{y}{h} - \frac{1}{2}\left(\frac{y}{h}\right)^2\right), \quad v = -\int_0^y \frac{\partial u}{\partial x}\,dy.$$

We used two types of disturbances:

(i) for stimulated oscillations,

$$F(t) = \varepsilon\cos\omega t,$$

where ε and ω are the amplitude and frequency of oscillations, respectively; and

Kuban State University,
ul. Stavropol'skaya 149, Krasnodar, 350040 Russia
e-mail: rastatur@fpm.kubsu.ru; edemekhi@nd.edu; kalaidin@econ.kubsu.ru

1028-3358/05/5002-0115$26.00

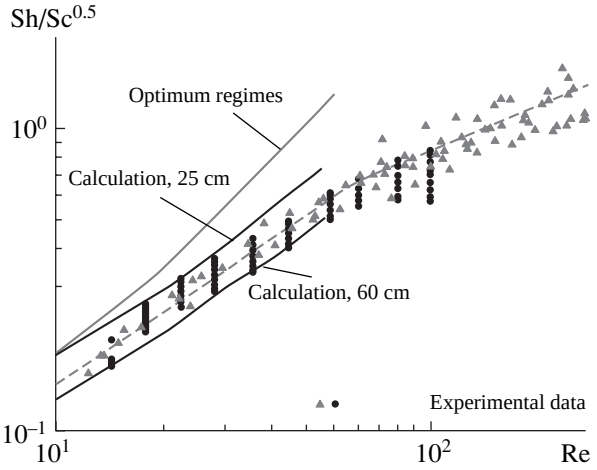

Fig. 1. Mass-transfer intensification by natural and excited waves. Denotations Re, Sh, and Sc correspond to Reynolds, Sherwood and Schmidt numbers, respectively.

(ii) for natural waves,

$$F(t) = \int_{-\infty}^{\infty} F_k(\omega) e^{-i\omega t} d\omega, \quad F_k(-\omega) = F_k(\omega)^*.$$

Here, the asterisk denotes the complex conjugation, $F_k(\omega) = |F_k| e^{i\theta}$, $|F_k| = \text{const}$, and θ is a random quantity uniformly distributed within the segment $[0, 2\pi]$.

The problem was solved numerically using a finite-difference scheme of second-order accuracy. The Sherwood number

$$\mathrm{Sh}_L = \frac{\mathrm{Pe}}{L} \ln \frac{c_s - c_0}{c_s - c_L}$$

was calculated on the basis of the mean-logarithmic concentration difference, where c_L is the concentration averaged over the flow rate at a distance L from the input.

2. The mass transfer was calculated for natural waves that developed as a result of random input noise for stimulated waves of the first family (i.e., for those close to sine-shaped waves), and for stimulated waves of the second family (chains of solitary waves) [5].

The natural waves arose as a result of the development of a random noise at the operation segment input. The degree of consistency with experimental data obtained was quite high (Fig. 1).

Regular two-dimensional waves were produced by periodic oscillations of the input fluid-flow rate; Quasi-stationary periodic waves of a given period were rapidly (i.e., at a distance of one wavelength) formed from these oscillations. The Sherwood number was obtained as a function of both the wave frequency and oscillation amplitude. Oscillation amplitude affects the stabilization rate of regular waves. An increase in the amplitude decreases the length of the initial segment, hence, its effect.

For each Reynolds number, there is a wave frequency for which the maximum mass-transfer factor is attained; this frequency for all Reynolds numbers is related to the third family (solitary waves). The flow regime for waves at this frequency is the optimum regime for a given Reynolds number (see Fig. 1).

One can identify two basic mass-transfer regimes (Fig. 2).

(a) For wave velocities exceeding the surface fluid-flow velocity, gas dissolution is determined both by the diffusion process and by the velocity component normal to the fluid surface. The fluid flow carries away the dissolved substance from wave hollows (in which the wave velocity attains its minimum) to wave crests in which the flow rate is ultimately close to the wave velocity. Here, the accumulation of the dissolved substance occurs. The maximum and minimum values of the flow through the surface are attained in wave hollows and wave crests, respectively. The magnitude of the mass transfer depends on the amplitude and velocity of the waves.

(b) There are points at the interface for which the wave velocity is lower than the surface flow velocity. In this case, there exist points on the wave surface at which the flow velocity on the surface equals the wave velocity (rest points). If so, the upper layers saturated with gas are carried away under the wave crest, which results in displacement of the saturated solution deep in the fluid film. Thus, the dissolved substance is not accumulated at the surface, which would prevent dissolution, but is delivered deep in the flow.

On the reverse side of a wave, there exists a point at which fluid is drawn from the wave depth to the surface. In this case, low-concentration zones are formed at the surface, which sharply increases the mass transfer at these domains. In contrast to the case (a), where the flow through the surface rapidly decreases with the rise in the concentration boundary layer, the decrease in the flow rate occurs much slower, until the wave crests are saturated with the dissolved gas.

The larger the amount of saturated solution that arrives at the domain under the wave crest, the greater the increase in the mass transfer; i.e., the lower the points are located at which the flow from the surface enters deep into the film, the higher the wave amplitude. In the case of displacement of the points to the wave vertex, the given regime is transformed into regime (a).

(c) For the regime of solitary waves, there exist in wave crests vortex motions of the fluid, as observed in the second regime. Here, the plane region existing between the solitary waves additionally affects the mass transfer. The concentration layer is mixed when waves pass by, and the boundary layer again begins to form in the film. However, as distinct from the forma-

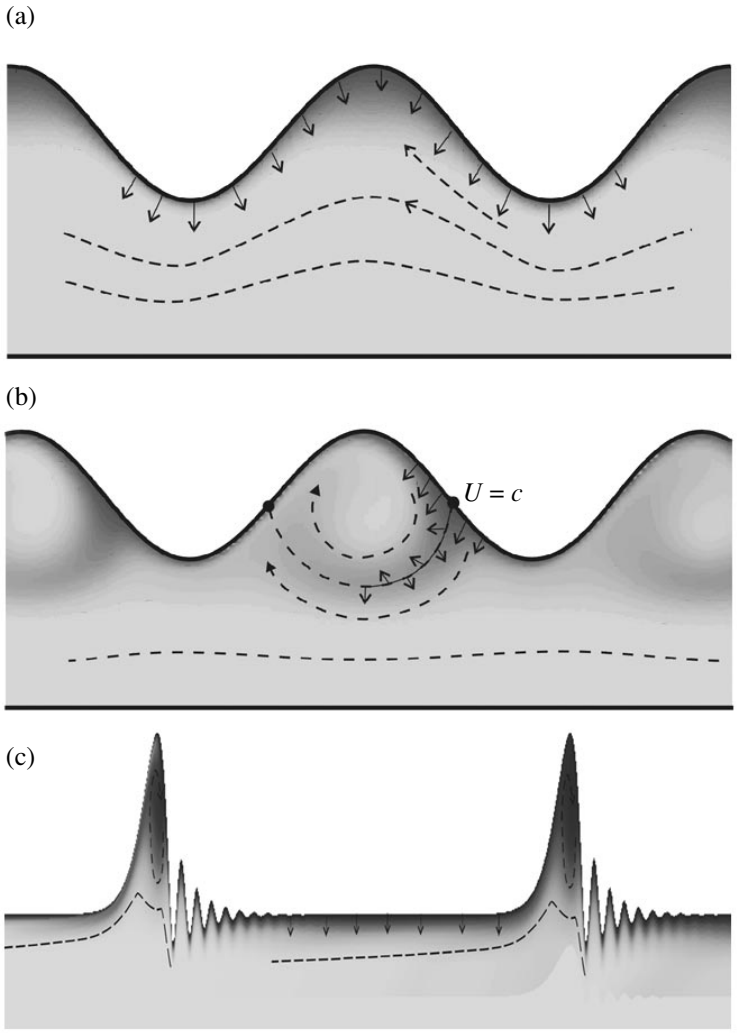

Fig. 2. Basic mass-transfer regimes.

tion of the boundary layer near the input, the gas concentration in the film is now nonzero.

As follows from our calculations, the mass-transfer intensification factor elevates somewhat with a decrease in the wave frequency and increase in the size of the plane region between waves. However, when the plane-region size is sufficiently high, the overall effect of the solitary waves on the mass transfer becomes negligible. In this case, the mass transfer, on average, proceeds in nearly the same manner as in the case of a wave-free flow. In other words, the mass-transfer intensification factor tends to unity, as the wave frequency tends to zero. Hence, a certain optimum wave frequency must exist for which the mass-transfer maximum is attained, which is confirmed by our calculations.

REFERENCES

1. S. V. Alekseenko, V. E. Nakoryakov, and B. G. Pokusaev, *Effects of Waves on Transport Processes. Wave Flow of Fluid Films* (Nauka, Novosibirsk, 1992), pp. 191–207.
2. P. N. Yoshimura, T. Nosoko, and T. Nagata, Chem. Eng. Sci. **51** (8), 1231 (1996).
3. L. P. Kholpanov, V. Ya. Shkadov, V. A. Malyusov, *et al.*, TFCE, No. 1, 73 (1976).
4. P. I. Geshev, A. M. Lapin, and O. Yu. Tsvelodub, *Hydrodynamics and Heat-and-Mass Transfer in Flows with a Free Surface* (IT SO AN SSSR, Novosibirsk, 1985), p. 102.
5. H.-C. Chang, E. A. Demekhin, and E. N. Kalaidin, AIChE J. **42**, 1553 (1996).

Translated by G. Merzon

Doklady Physics, Vol. 50, No. 2, 2005, pp. 63–65. Translated from Doklady Akademii Nauk, Vol. 400, No. 4, 2005, pp. 467–469.

PHYSICS

Effect of Magnetic Field on Low-Cycle Fatigue

P. A. Aleksandrov and M. N. Shakhov

Presented by Academician K.V. Frolov September 14, 2004

Received September 23, 2004

It is well known that a large percentage of technological accidents are caused by fatigue of metallic structures. At the same time, the allowance for fatigue in strength calculations is often incorrect. There are a number of causes why this is so: defects of material, deviations from standard composition, computational problems, etc. In this study, we deal with a new phenomenon associated with the strong dependence of fatigue damages on magnetic-field intensity—an issue that has previously been ignored. This phenomenon is of interest from the standpoint of metal physics, is important in technological applications, and represents one of the manifestations of magnetoplastic effects (MPEs).

In recent years, MPEs in crystals have attracted much attention (see, for example, review [1]). In numerous studies, phenomena such as macroscopic plastic-flow rate, creep, yield point, and microhardness were investigated. It has been found that dislocation paths in silicon subjected to the action of a magnetic field with the induction of 1 T were up two times greater than those in the absence of the magnetic field [2]. It should be noted that this effect was observed only in silicon crystals with oxygen impurities that may be paramagnetic. The basic materials for investigations of MPEs have been NaCl crystals (often used to visually observe dislocations), semiconductor crystals, and, far more infrequently, polycrystals of metals. In [3], it was established that, in the case of a concentrated load, the process of twinning is partly suppressed in bismuth crystals subjected to the action of a magnetic field. The authors of [3] believe that this fact testifies to a decrease in the mobility of partial twinning dislocations in the presence of magnetic field. In this case, the twin length decreased by 30%, and the microhardness increased by 10%. The basic difficulty in explaining MPEs is the weak interaction between a point defect possessing a spin and the magnetic field. For example, in the field of 1 T, the corresponding interaction energy U_H equals 10^{-4} eV, i.e., it is much lower than the thermal-fluctuation energy (3×10^{-2} eV). Therefore, it is assumed that MPEs have a dynamic character and that the magnetic field affects both dislocation motion and dislocation–stopper interaction.

Based on the above reasoning, we supposed that the magnetic field also affects other phenomena associated with dislocation motion. In our opinion, metal fatigue, of all phenomena, may be the most sensitive to the magnetic field. Metal fatigue is a phenomenon related to the generation and motion of dislocations under the action of mechanical stresses. Dislocations can stop on stoppers, i.e., on high potential barriers associated with lattice defects. Being concentrated in a certain region, the dislocations form clusters that can later transform into crack nuclei along which metal fatigue failure may occur. It is clear that, insofar as the dislocation–defect interaction depends on magnetic field, the entire pattern of metal fatigue may dramatically change in a magnetic field.

It seems likely that weakening the interaction between dislocations and a paramagnetic impurity must result in a longer dislocation path and a larger concentration of the dislocations at stopping points. As a result, the fatigue damages under deformation must be accumulated for a shorter time, and a failure of sample must also occur more often. However, due to the unknown structure of paramagnetic defects and the complex character of dislocation–defect interaction, it is possible to evaluate neither the magnitude of the effect nor even its sign. Nevertheless, we may assume that fatigue phenomena are solely responsible for the MPE, which must be well pronounced because the dislocation accumulation process depends on a magnetic field.

In this study, we investigated the low-cycle fatigue of a cylindrical wire under bending deformation in both the presence and absence of magnetic field. We choose the wire because its uniformity across the diameter along the entire length of the sample was provided by the production technology. Cyclic bending was performed through an angle of 180° along a guide 7 mm in diameter. The magnetic field was produced by two permanent magnets with dimensions of $60 \times 32 \times 17$ mm^3; there was a 3-mm gap between the magnets. The mag-

Institute of Information Technologies,
Russian Research Center Kurchatov Institute,
pl. Kurchatova 1, Moscow, 123182 Russia
e-mail: iitdir@mail.ru; msha@bk.ru

1028-3358/05/5002-0063$26.00

Effect of the magnetic field on the number of cycles before failure of a sample

Material of sample	Diameter of sample, mm	Number of cycles before failure	
		with magnetic field	without magnetic field
Unannealed copper	1.5	180, 180, 156, 209, 119, 211	75, 111, 118, 106, 116
	2.5	22, 23, 21, 25, 22, 24	33, 24, 24, 23, 30, 39, 23
Unannealed copper in the polyvinyl chloride insulation	2.5	123, 72, 86, 138, 100	127, 114, 90, 118, 64
Annealed copper*	2.5	35, 29, 40, 29, 28, 31, 36	44, 41, 42, 43, 34, 39
Aluminum	1.5	7, 7, 6, 8, 7, 7	6, 6, 7, 6, 7, 5
Tungsten–rhenium wire	1.5	7, 17, 4, 16, 1	15, 21, 1, 1, 7, 12
Lead**	3.0×1	10, 14, 12, 15, 13, 22	20, 18, 27, 27, 29, 20
*E*110 zirconium	3.0	23, 22, 23	56, 53, 52
Brass	2.0	78, 88, 89, 84, 96	160, 164, 147, 154

* Annealing: heating to 700°C for 50 min, holding for 30 min followed by cooling to room temperature in a furnace for about 6 h.
** Stripe-shaped samples; the cross-section size is indicated.

netic field attaining 0.79 T was measured by a Sh1-8 magnetometer. In our experiment, we determined the number of deformation cycles before failure for wires made of different metals. Furthermore, we performed experiments in the absence of the magnetic field under similar conditions (i.e., with the same angle and bending radius). The results obtained are presented in the table. As seen there, the effect of the magnetic field on metal fatigue is noticeable.

For the copper wire, we obtained rather contradictory results. In the first series of our experiments, the samples failed more rapidly upon cycling without magnetic field, whereas in the remaining series, the situation was reversed. In addition, the results obtained are characterized by a considerable spread. However, despite this spread, the effect of the magnetic field is noticeable.

To determine the role of the adsorbed oxygen and dislocation structure appearing over time in copper samples, the copper wires were subjected to annealing. After annealing, the spread in the results had slightly decreased, but the effect also existed.

For aluminum samples, there was no significant difference between the numbers of cycles before failure in both the presence and the absence of the magnetic field.

For the tungsten–rhenium wire, in addition to the high spread of the results, a considerable inhomogeneity was observed in the samples. Therefore, the results obtained cannot confirm or deny the expected effect.

The lead-based samples (in contrast to others, they had been made stripe-shaped) failed much more rapidly and with rather high reproducibility in the presence of magnetic field.

Samples made of *E*110 zirconium alloy failed much more rapidly in the magnetic field. In this case, the number of cycles before failure is smaller by a factor of two compared to the case in which the field is absent. The spread of data obtained is low. However, because the number of the samples was limited, we managed to perform only three tests. Nevertheless, the results obtained demonstrate that the magnetic field essentially affected the fatigue characteristics of the given material. For brass samples, a significant decrease in the number of cycles before failure was observed if the samples had been loaded in the presence of magnetic field. The number of cycles before failure decreased by a factor of approximately two. The spread of results obtained for the brass samples is the lowest among all tested materials (with respect to the number of cycles before failure, the spread in the results is about 10%).

In addition to tests aimed at low-cycle fatigue, the brass samples were tested with an Instron 4301 tensile-testing machine. We measured the tensile diagrams in both the presence and absence of the magnetic field. As is seen in the figure, the curve shapes are different for these cases, i.e., the magnetic field also affects mechanical characteristics of the materials (changes attain about 10%).

Thus, the rather strong effect of the magnetic field on fatigue failure in series of metals is experimentally demonstrated. It is important to note that fatigue is much more sensitive to the magnetic field than are other mechanical properties of the materials (see the figure).

We now formulate the conditions under which the effect of the magnetic field on the mechanical properties of metals can be observed. First, a sample must be in a stressed state that stimulates dislocations into motion. This stress may be caused both by an applied

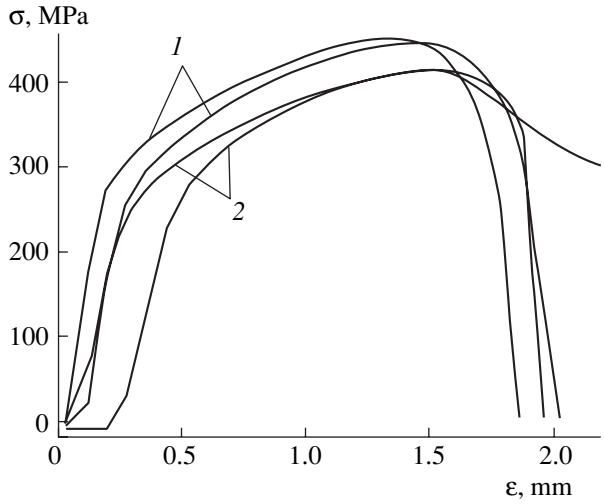

Stress–strain diagram for brass samples: (*1*) without magnetic field and (*2*) with magnetic field.

external load and by the residual stresses that appear in the course of preparing samples. Second, the existence of paramagnetic impurities is necessary; however, their amount can be very small, since the path passed by a dislocation is rather long (hundreds and thousands of interatomic distances). Therefore, it is sufficient to have a background impurity concentration (see the experiments with the copper wire).

Thus, the effect observed may be of interest not only from the standpoint of metal physics, but also from that of technical applications. First, we note large-scale thermonuclear facilities, in which a large number of structural elements undergoing cyclic loads are placed into a magnetic field with the induction exceeding 1 T. The other line of research in which high magnetic fields are applied is the use of large-scale detectors in high-energy physics experiments.

The radiation hardness of materials, which is associated with dislocation motions such as creep and embrittlement, seems also to be dependent on the magnetic field.

The results obtained indicate that it is appropriate to perform experiments and, probably, to revise the calculations for materials and structures used in large-scale facilities (for example, in the ITER thermonuclear reactor and ATLAS detector for the accelerator under construction at CERN) in which magnetic fields of 4–5 T occupy a large volume so that similar effects can be much stronger than those in the experiments described above.

REFERENCES

1. R. B. Morgunov, Usp. Fiz. Nauk **174**, 131 (2004) [Phys. Usp. **47**, 125 (2004)].
2. A. M. Orlov, A. A. Skvortsov, and L. I. Gonchar, Fiz. Tverd. Tela (St. Petersburg) **43**, 1207 (2001) [Phys. Solid State **43**, 1252 (2001)].
3. A. I. Pinchuk and S. D. Shavreĭ, Fiz. Tverd. Tela (St. Petersburg) **43**, 39 (2001) [Phys. Solid State **43**, 39 (2001)].

Translated by Yu. Vishnyakov

Doklady Physics, Vol. 50, No. 2, 2005, pp. 66–68. Translated from Doklady Akademii Nauk, Vol. 400, No. 5, 2005, pp. 618–620.

PHYSICS

Experimental Study of Thermal and Fire Tornados

A. M. Grishin[1], A. N. Golovanov[1], A. A. Kolesnikov[1], A. A. Strokatov[1], and R. Sh. Tsvyk[2]

Presented by Academician G.G. Chernyĭ September 9, 2004

Received September 30, 2004

In [1] various types of tornado-like flows arising above a heated rotating disk in the quiescent-air atmosphere were studied and an illustrating diagram was also presented. In what follows, we will refer to one of these types, namely a sole tornado-like vortex, as a *thermal tornado.*

In [2], different methods for physically modeling fire tornados were proposed. It was shown that formation of fire tornados depends neither on the method of their production nor the nature of combustible material. This phenomenon is determined rather by both the density of heat flow arising as a result of combustion and the angular velocity (or frequency $\omega = 1.1$–1.3 Hz) of rotation of the cylinder into which the combustible substance is placed.

The goals of the present paper are to present a comparative study of thermal and fire tornados, to understand conditions causing the appearance of fire tornados, to identify their types, and to analyze their stability as a function of both the level of combustible liquid in the cylinder and gas-flow properties.

In this study, ethyl alcohol was used as a combustible liquid. Two methods were employed for swirling combustible liquid and combustion products. We implemented swirling from below by the rotation of a substrate (cylindrical vessel) and from above by means of a fan.

Our setup consisted of an Mi-22 electric heater, a base, an electric-current voltage regulator, and a circular steel disk 0.4 m in diameter. The combustible liquid was placed on a cylindrical steel substrate fixed to the disk. In different experiments, the diameter and height of the cylinder were (6, 7, 10, 12, or 20) $\times 10^{-2}$ m and (2, 6, or 12) $\times 10^{-2}$ m, respectively.

A thermocouple and a thermal-flux sensor, whose signals had been registered by a KSP-4 recorder, were used as measuring tools. The shaft rotation frequency of an electric motor with the disk was specified by the voltage regulator and varied within the limits of 0–20 Hz. In addition, as distinct from the experiment performed in [2], in a number of cases, an immobile steel circular plate 2×10^{-3} m thick and 0.5 m in diameter was placed at heights of 0.4, 0.45, and 0.5 m above the rotating substrate. In the experiments, the temperature of this plate remained almost invariable, which allowed us to model the action of the inversion layer of atmosphere temperature on a fire tornado.

According to established methods for studies of state parameters, which had been applied in [2], we used in the present work an AGA-780 SW infrared imager with a registration frequency of 25 frames per second and a heat-loss anemometer with a platinum-wire diameter of 2×10^{-5} m and length of 6×10^{-3} m. The height of the liquid layer in the cylinder varied within a range of 0.02 m to 0.11 m.

We initially performed experiments in which different levels of ethyl alcohol were poured into the metallic cylinder heated by an electric heater. It was found that a decrease in the level of combustible liquid made it possible to vary the rotational velocity from 1.1 to 4.3 Hz, at which a fire tornado arose. This result is explained by the fact that the process of diffusion combustion proceeds in the cases in which oxygen is sufficiently delivered from the surface of a liquid fuel. It is well known that with an increase in rotational velocity, the free convexity of the liquid surface in the cylindrical vessel is more and more directed downward, therewith parts of the liquid, which adjoin the vessel surface, are situated higher than the quiescent-liquid level in the basic volume. Therefore, diffusion combustion arises in the vicinity of the substrate walls. Upon formation of a fire tornado, combustion shifts to the central region of the vessel, since the delivery of oxygen is provided as a result of air suction from the environment. This suction is explained by the fact that the pressure in the vortex central part is lower than the pressure in the environment.

[1] *Tomsk State University, Tomsk, ul. Lenina 36, 634950 Russia*
e-mail: fire@fire.tsu.tomsk.su

[2] *Institute of Atmosphere Optics, Siberian Division, Russian Academy of Sciences, pr. Akademicheskiĭ 1, Tomsk, 634055 Russia*
e-mail: tsvyk@iao.ru

1028-3358/05/5002-0066$26.00

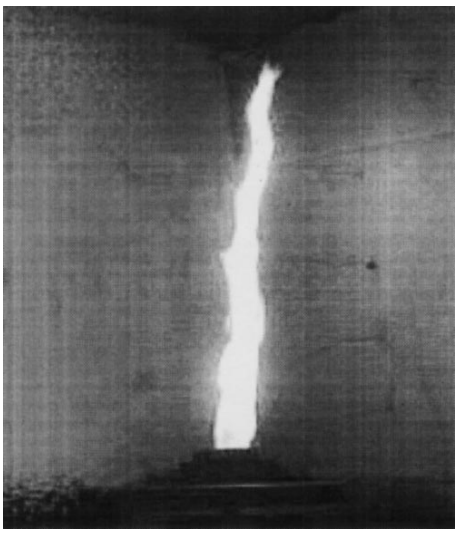

Fig. 1. Fire tornado in free space (swirling from below).

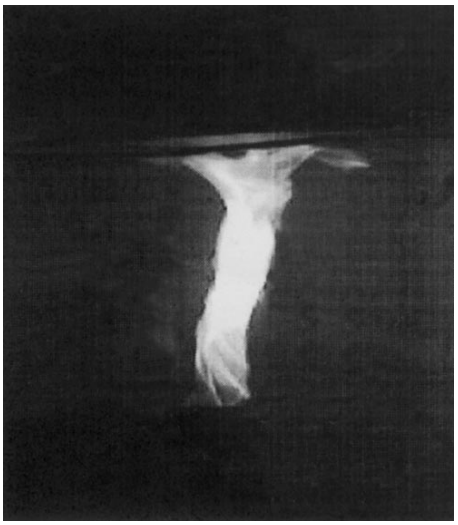

Fig. 2. Fire tornado in the case of the presence of an obstacle from above at a height $H = 4 \times 10^{-1}$ m (swirling from below).

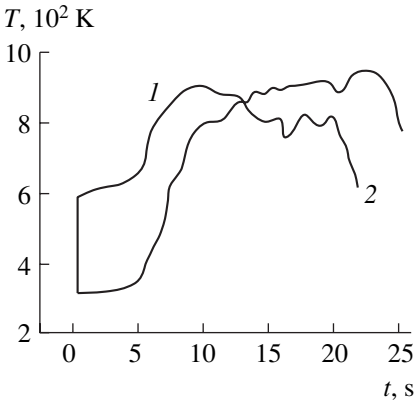

Fig. 3. Combustion of ethyl alcohol without swirling. Here, as in Fig. 4, (*1*) $h = 10^{-1}$ m and (*2*) 1.5×10^{-2} m.

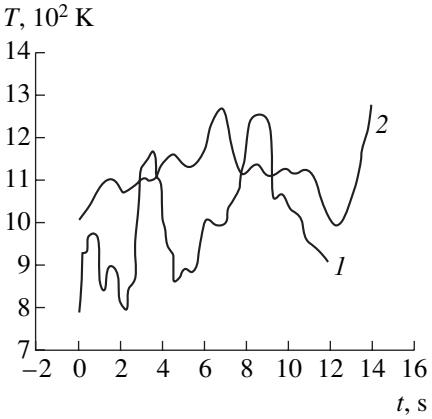

Fig. 4. Gas temperature inside a fire tornado in the case of its swirling from below.

A photograph is shown in Fig. 1 of a free fire tornado that was obtained as a result of burning 0.05 kg of ethyl alcohol for the edge height (distance from the surface of the liquid to the open upper boundary of the vessel) of 0.08 m and the rotation frequency $\omega = 4$ Hz. The velocities of gas-flow particles in the tornado, which had been measured by method of observing luminescent-particle tracks, attained 0.2–0.25 m s^{-1} at a height of 0.1 m reckoned from the substrate.

Figure 2 presents a photograph of a tornado developed in a space bounded from above. As is seen, the fire tornado takes the mushroom-like shape.

Variations in the geometric size of the fire tornado in a space bounded from above at a height of 0.5 m are shown in the table. Here h_i ($i = 1, 2, 3$) are heights of fire-tornado cross sections, d_i are their diameters, and σ_{ih} and σ_{id} are the corresponding standard deviations.

h_i, 10^{-3} m	98.53	96.28	155.75
σ_{ih}, 10^{-3} m	9.5	11.7	30.45
d_i, 10^{-3} m	60.01	66.36	104.20
σ_{id}, 10^{-3} m	13.3	17.5	20.3

In Figs. 3 and 4, plots are shown illustrating variations of gas temperature at the flame axis for $\omega = 0$ and in the case of gas swirling from below, respectively. Comparing these plots, we may conclude that swirling from below results in elevating the temperature, which can be explained by a rise of the diffusion combustion rate as a result of an increase in the oxygen inflow rate.

It is of interest to clarify causes for the appearance and existence of fire tornados. In [3], all examples of

concentrated tornados known in the literature are given. The authors of [3] indicate that these tornados correspond to "such vortex motions for which the vorticity is concentrated in spatially localized domains, exhibiting the localization in at least one direction." Twelve types of such phenomena and their diagrams are given in [3]. Among them a phenomenon described in detail in [1] is mentioned. However, there is no information on spatially localized structures such as fire tornados. These structures can undoubtedly be related to a specific class of concentrated columnar tornados and are reminiscent of Rankine vortices and one-dimensional columnar tornados [3]. From a physical standpoint, the phenomenon of fire tornados are like vortex filaments caused by ascending flows above an evaporating liquid heated from below [4]. At the same time, a fire tornado is a more complicated physical phenomenon that includes (in conditions of a quasi-steady process) the following features.

Rotation of a liquid fuel and its ignition in the vicinity of cylinder walls.

Evaporation of a liquid fuel under the action of radiant thermal flow from the combustion zone and formation of vortex filaments.

Air suction by the tornado from the environment to the combustion zone, since the pressure at the tornado axis remains lower than air pressure in the environment, which is, in turn, a result of the convection caused by pressure difference and diffusion.

Oxidizer inflow to the combustion zone.

Energy release in the combustion zone (the burning of vortex filaments of the evaporated liquid) and formation of a fire tornado.

Ascending (turbulent flow) of combustion products as a result of the buoyancy force.

Afterburning of gaseous-fuel vapors in the tornado above the combustion zone.

Local mechanical equilibrium of forces acting on the tornado (the centrifugal force arising by virtue of the pressure difference between the tornado interior and the external medium and buoyancy force) in the system involving the substrate, the combustion zone, the concentrated vortex, and the environment.

Thus, the fire tornado, as distinct from the thermal variety, is a complicated air-thermochemical phenomenon. For its mathematical modeling, it is appropriate to apply methods for substituting and solving conjugate problems of the mechanics of reacting media [5].

Based on the conditions of the local mechanical equilibrium of a tornado, as well as a rotating platform and the experimental results obtained in [1], we have managed to derive a semi-empirical formula for the critical (equilibrium) platform velocity at which a fire tornado arises:

$$\omega = a_i\left(\frac{2gh(T_* - T_e)}{T_e}\right)^{0.5} r_0^{-1}, \quad i = 1, 2. \qquad (1)$$

Here ω is the platform rotation velocity; r_0 and h are the radius and height of the columnar fire tornado; T_* is the temperature inside the fire tornado; T_e is the environmental temperature; and a_1 and a_2 are empirical constants corresponding to thermal and fire tornados, respectively.

Expression (1) can be rewritten in the dimensionless form

$$\mathrm{Ro} = \frac{W}{r_0\omega} = 1, \quad W = a_i\sqrt{\frac{2gh(T_* - T_e)}{T_e}}, \qquad (2)$$

where W is the characteristic floating-up velocity and Ro is the Rossby criterion number [1].

In accordance with [1], formula (2) represents the condition for the appearance of thermal tornados. This expression corresponds to the condition of local equilibrium and is, at the same time, the necessary condition of fire-tornado formation.

Analyzing both these formulas and the experimental data presented in [1], we arrive at the conclusion that the rotation velocity of a tornado decreases as its radius increases and rises as its height increases.

REFERENCES

1. B. M. Bubnov, Izv. Akad. Nauk, Fiz. Atm. Okeana **33** (4), 434 (1997).
2. A. M. Grishin, A. N. Golovanov, and Ya. V. Sukov, Dokl. Akad. Nauk **395**, 196 (2004) [Dokl. Phys. **49**, 191 (2004)].
3. S. V. Alekseenko, P. A. Kuĭbin, and V. L. Okulov, *Introduction into Theory of Concentrated Vortices* (Izd. Kutateladze Inst., Siberian Division of the RAS, Novosibirsk, 2003).
4. V. A. Vladimirov, Dokl. Akad. Nauk SSSR **236**, 316 (1977) [Sov. Phys. Dokl. **22**, 482 (1977)].
5. A. M. Grishin, *Modeling and Forecasting Catastrophes* (Izd. Tomsk. Univ., Tomsk, 2003).

Translated by G. Merzon

Doklady Physics, Vol. 50, No. 2, 2005, pp. 69–71. Translated from Doklady Akademii Nauk, Vol. 400, No. 6, 2005, pp. 749–751.

PHYSICS

On the Kinetics of Premicellar Association in Solutions of Triblock Copolymers

Corresponding Member of the RAS P. K. Khabibullaev, Z. Sh. Bakaeva, M. R. Zaitdinov, S. Z. Mirzaev, and M. G. Khaliulin

Received September 14, 2004

Surface-active substances (SAS) and triblock copolymers are objects composed of structurally complicated molecules that clearly demonstrate the orientation interaction between themselves and an ambient solution. This leads to the appearance of both regular and irregular structures, such as molecular complexes and associations: micelles, vesicles, liquid crystals, etc. [1]. The properties of these systems near stability points are determined by the finite sizes of arising structures. In the vicinity of phase-transition points, the universal properties of these objects are violated and features characteristic of objects of each class begin to manifest themselves.

Structural-association processes are collective and are characterized by rather long mean lifetimes and mean reconstruction times of corresponding structures. The use of low-frequency precision acoustical technology makes it possible to investigate self-organization processes in solutions.

In this paper, we describe results of studies on the ability of triblock copolymers to form premicellar associations in a water solution. The investigations were performed by a low-frequency acoustical method over a wide range of temperatures and concentrations. An advantage of using triblock copolymers is that it provides the possibility of approaching the critical point of micelle production over temperature (CMT) and concentration (CMC). In order to investigate sound attenuation at low frequencies, a precision ultrasonic resonator was developed intended to register the relaxation in weakly absorbing copolymer solutions at low frequencies. Water taken at a temperature of 25°C was used as a reference liquid. The ultrasonic resonator allowed us to investigate the sound attenuation in weakly absorbing liquids, in which it was previously impossible, employing known methods, to measure this phenomenon.

There is but poor information in the literature on processes that occur in the cases where SAS concentrations are lower than the CMC [2–4]. This information is limited to the possibility of description, e.g., of the relaxation-frequency increase as a result of several processes that can occur under given conditions. Unfortunately, the absence of an acceptable theory of premicellar-association processes prevented calculation of the kinetic parameters and thermodynamic characteristics of the suggested process. It was assumed that a weak decrease in relaxation frequency within the region of strong dilutions was contingent upon a decrease in monomer concentrations.

The triblock copolymer PLURONIC PE6400 (BASF) with the macroscopic-chain structure

$$H(CH_2–CH_2–O)_{13}–(CH_2–CH(CH_3)–O)_{30}–(CH_2–CH_2–O)_{13}H$$

(without additional purification) was chosen for our experiments aimed at the observation of acoustical relaxation at concentrations and temperatures of a copolymer aqueous solution lower and higher than CMC and CMT. Prior to its use, water was subjected to thorough purifying and degassing. For any studied concentration, the interface between the micellar and free states of the copolymer monomer was determined in accordance with the equation

$$t(\text{CMT}) = 31.92(°\text{C}) - 8.22(°\text{C})\log x,$$

where x (wt %) is the amount of a copolymer [5]. Aqueous solutions of the copolymer were studied at concentrations of 0.55, 1, 3, 4, 4.3, 4.5, 5.5, 6, 6.2, 6.5, 7, 8, 9, and 10 wt % within a frequency range of 200 kHz to 500 MHz.

In the figure, experimental results are presented for the dependence $\frac{\alpha}{f^2}$ as a function of the frequency for two copolymer concentrations at a temperature of 25°C.

Thermal-Physics Department, Academy of Sciences, Republic of Uzbekistan, Katartal 28, Tashkent, 700135 Uzbekistan
e-mail: mirzaev@web.de

1028-3358/05/5002-0069$26.00

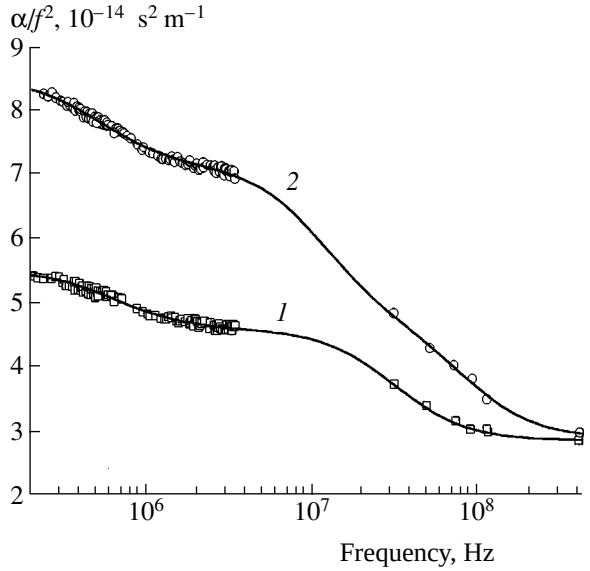

Sound attenuation (related to the frequency squared) as a function of frequency for copolymer solutions at concentrations of (*1*) 4 and (*2*) 6 wt %.

At temperatures lower than CMT and CMC, the sound attenuation divided by the frequency squared has a very small value. However, it is always larger than for pure water at the same temperatures and it increases with the copolymer concentration *x*. This behavior of the sound attenuation indicates the existence of processes weakly contributing to the sound attenuation in cases when micellar aggregations are absent in the system. Similar behavior was observed for ionogenic SASs that have short alkyl chains, and such behavior was attributed to the formation of premicellar aggregations [2]. The other process that can contribute to the sound attenuation spectrum is the monomolecular relaxation associated with variation in the copolymer-chain conformation, which was observed in the copolymer solution [2]. The measurements performed for the concentrations of 0.55–1 wt % at 22°C have revealed the existence of a single process only. As is seen from the figure, at a temperature of 25°C, there exist two characteristic bends corresponding to two different relaxation processes in the 4-wt % solution. In order to determine the relaxation time, the data obtained were treated with the help of the equation involving two relaxation times:

$$\frac{\alpha}{f^2} = \sum_{i=1}^{n} \frac{A_i}{1 + (2\pi\tau_i f)^2} + B. \quad (1)$$

Here, A_i is the relaxation-process amplitude; τ_i is the relaxation time; and B is the amplitude of the sound background attenuation, which was obtained for the frequency of 500 MHz. For the solution with the copolymer content of 6 wt %, an equation with three relaxation times was used.

Two relaxation regions are manifested in the acoustical spectra obtained: the first one extends up to 1.5 MHz and the second up to 40 MHz. The values of A_i and τ_i were obtained by the best-fit method using experimental data and the calculation results according to Eq. (1) (see table). Parameters of the experimental spectra were found on the basis of a computer version of a nonlinear algorithm. The first relaxation region has a very low amplitude A_1 and linearly increases with the copolymer concentration. The second region has an explicitly pronounced characteristic bend, and the relaxation time for this process lies within the same frequency range for all concentrations studied. As is seen from the figure, the relaxation time of the process is independent of the concentration. A similar concentration–temperature behavior is characteristic of all monomolecular relaxation processes [6, 7]. Therefore, we have attributed this behavior to the conformational equilibria of a triblock-copolymer macromolecule.

In the concentration dependence of relaxation time, two regions are manifested. The first one corresponds to concentrations lower than CMC and is characterized by a slow monotonic increase in the relaxation time. The second region is located beyond the CMC and is observed in the case of a further increase in copolymer concentration in the solution, which is accompanied by a monotonic decrease in the relaxation time.

We now consider the first region in the concentration dependence of the acoustical relaxation time τ_1, which is apparently associated with the reaction of formation and decomposition of dimers and with the creation from the dimers of aggregations composed of copolymer molecules whose number exceeds two:

$$N_1 + N_1 = N_2, \quad (2)$$

$$N_1 + N_2 = N_3. \quad (3)$$

Parameters τ, A, and B as functions of the concentration in the low-frequency relaxation region

Copolymer concentration, wt %	τ, ns	A, 10^{-15} s^2 m^{-1}	B, 10^{-15} s^2 m^{-1}
2	226	5.2	31
3	237	7.7	37
4	255	9.3	45
4.5	277	10	47
5.5	400	14.3	65
6	253	14	68
6.2	218	16	74
7	189	31	115
8	172	42	128
9	159	50	157
10	153	64	180

Here, N_1 and N_2 are the numbers of copolymer monomers and dimers, respectively, and N_3 is the number of aggregations in which the number of copolymer molecules exceeds two. For solving reaction equation (3), we need to know the equilibrium distribution of concentrations among different aggregations. Solution of this as-yet unsolved problem will enable a complete description of concentration dependences for the acoustical parameters of premicellar solutions. In [1], an equation was derived that makes it possible to connect the inverse-reaction rate constant and the relaxation time of premicellar aggregations: $\frac{1}{\tau_1} \sim 0.5\bar{k}$. In accordance with this expression, the constant of the inverse reaction is $\bar{k} \sim 1 \times 10^9$ s^{-1}.

We may conclude that the application of new precision low-frequency acoustical methods has allowed us to discover relaxation processes with a very small attenuation in the regions of lower concentrations compared to the CMC and CMT in copolymer water solutions and to determine important kinetic parameters of relaxation processes. Our investigations have shown that in copolymer solutions, the relaxation time of structure-formation processes anomalously increases as the CMC and CMT are approached. It has been found that in contrast to segregating systems [1], times of relaxation processes in micelle-forming triblock copolymers have finite durations in the vicinity of the critical concentration of micelle formation.

ACKNOWLEDGMENTS

The study was supported by the Science-and-Technology Center Foundation of Republic Uzbekistan and by the NATO grant no. RIG 981193.

REFERENCES

1. P. K. Khabibullaev and A. A. Saidov, *Phase Separation in Soft Matter Physics. Micellar Solutions, Microemulsions, Critical Phenomena* (Springer, Heidelberg, 2003), Part B, p. 180.
2. P. K. Khabibullaev, E. V. Chertkov, and A. A. Saidov, Colloids Surf. A, Phys. Eng. Asp. **168**, 185 (2000).
3. A. W. Adar Douglas, V. C. Reinsborough, H. M. Trenholm, *et al.*, Can. J. Chem. **56**, 1162 (1976).
4. Z. S. Bakaeva, M. Zaitdinov, S. Z. Mirzaev, *et al.*, in *10th APAM Topical Seminar and 3rd Conference "Materials of Siberia. Nanoscience and Technology"* (Novosibirsk, 2003), p. 81.
5. P. Alexandris and R. A. Hatton, Colloids Surface **96**, 1 (1995).
6. S. Z. Mirzaev, P. K. Khabibullaev, A. A. Saidov, *et al.*, J. Chem. Phys. **112**, 1057 (2000).
7. S. Z. Mirzaev, P. K. Khabibullaev, V. S. Kononenko, *et al.*, J. Acoust. Soc. Am. **107**, 585 (1998).

Translated by G. Merzon

Doklady Physics, Vol. 50, No. 2, 2005, pp. 72–76. Translated from Doklady Akademii Nauk, Vol. 400, No. 4, 2005, pp. 470–474.

TECHNICAL PHYSICS

Conditions of the Attainable Superheating of the Surface of Nonvolatile Condensed Systems upon Intense Heating

O. F. Shlensky

Presented by Academician V.V. Osiko June 21, 2004

Received September 9, 2004

The necessary conditions for the attainable superheating of volatile substances and their mixtures above the temperature of the liquid–vapor equilibrium phase transition are quite well studied [1, 2]. In particular, the heating intensities necessary for approaching the upper phase-state boundary are determined by detection of the pressure dependence of the attainable superheating temperatures $T_l(p)$. In thermal physics, the phase-state boundary is determined by the condition of thermodynamic stability, i.e., the zero second variation of one of the thermodynamic potentials, e.g., $\delta^2 G = 0$, where G is the free Gibbs energy. At the stability boundary, the derivatives $\frac{\partial p}{\partial v}$ and $\frac{\partial T}{\partial v}$ vanish, which makes it possible to calculate the parameter of the phase-state boundary from the equation of state. The conditions for the attainable superheating of nonvolatile condensed systems are determined primarily in experiments [2–4]. At the same time, the development of mathematical models of the thermal destruction of condensed systems, e.g., for calculations of thermal protective covering, optimization of combustion regimes of solid fuels and the cracking processes of heavy mineral oils, etc. require the analytical representation of the above conditions.

The aim of this work is to determine the heat consumption and heating rates necessary for reaching the phase-state boundary under a given pressure in the steady regime of the thermal destruction of the heated surface of nonvolatile condensed systems and to experimentally test the resulting relations.

We consider steady processes of propagating a thermal wave with a velocity of u_T, which are described by the heat conduction equation

$$\lambda\frac{d^2T}{dx^2} + u_T c\rho\frac{dT}{dx} + F(T) = 0, \qquad (1)$$

where $F(T) = \rho Q w$ is the heat-absorption (heat-liberation) function and Q is the heat of the reaction, and the other notations are standard. The boundary conditions have the form $-\lambda\frac{dT}{dx} = q$ for $x = 0$ and $T = T_0$ for $x = \infty$. Integration of Eq. (1) shows that the maximum superheating arises on the surface of a condensed system (for $x = 0$) [5]

$$T_s = T_0 + \frac{fQu}{cu_T} + \frac{q}{uc\rho}, \qquad (2)$$

where f is the factor of a decrease in the heat of reaction due to the incompleteness of the reaction. According to [6, 7], taking the front propagation velocity as $u = \left(\frac{aw}{f}\right)^{1/2}$, we obtain

$$T_s = T_0 + fQ + q\left(\frac{\lambda c\rho w}{f}\right)^{-1/2}. \qquad (3)$$

Here, $a = \frac{\lambda}{c\rho}$; and $w = \frac{dC}{dt} = -kC^n$, where n is the reaction order, is the average reaction rate in the reacting layer. The rate constant k with allowance for an increase in the transformation rate near the phase-state boundary is determined by the generalized Arrhenius equation [7, 8]

$$k = BK(T)\exp\left(-\frac{E}{RT_s}\right), \qquad (4)$$

where B is the pre-exponential factor; E is the activation energy; and

$$K = \exp\left(\frac{T}{T_1}\right)^m \exp\left(-\frac{E}{RT}\right),$$

where m is a parameter, represents a change in the conversion mechanism near the phase-state boundary. For temperatures $T < T_l$, $K \approx 1$ and Eq. (4) is an ordinary two-parameter Arrhenius equation. Substituting w into Eq. (3), we express the heat flow necessary for estab-

Mendeleev University of Chemical Technology, Miusskaya pl. 9, Moscow, 125047 Russia

1028-3358/05/5002-0072$26.00

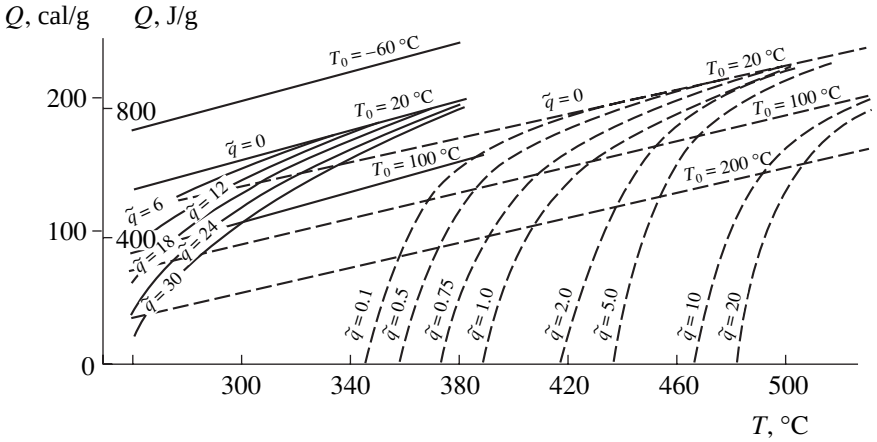

Fig. 1. Temperature dependence of the heat of the thermal-destruction reaction that is necessary for reaching the phase-state boundary for q = const, $\tilde{q} = \frac{q}{q_0}$, where $q_0 = 4.186$ J/(m^2 s) for (solid lines) a nitrocellulose-based compound and (dashed lines) ammonium perchlorate.

lishing a given temperature on the surface of the condensed system for $Q < 0$ in the form

$$q = \left[\frac{\lambda c\rho}{f} BK\exp\left(-\frac{E}{RT_s}\right)\right]^{1/2}\left[\frac{fQu}{cu_T} + (T_s - T_0)\right]. \quad (5)$$

For condensed systems destroyed with the heat release ($Q > 0$), the heat of the reaction Q necessary for establishing a given temperature on the surface for q = const is obtained from Eq. (3) as

$$Q = \frac{c}{f}(T_s - T_0) - \frac{cq}{f}\left[\frac{\lambda c\rho}{f} BK\exp\left(-\frac{E}{RT_s}\right)\right]^{-1/2}. \quad (6)$$

Working from a number of assumptions, such as the existence of constant parameters, Eqs. (5) and (6) make it possible to determine the q and Q values at which the surface temperature T_s asymptotically tends to the attainable superheating temperature. To this end, $T_s \approx T_l - \Delta T$, where ΔT is the given calculation accuracy, should be assumed in these equations.

Let us compare calculations by the above formulas with experimental data. For the parameters $\frac{E}{R}$ = 21500 K, $B = 10^{13.32}$ s^{-1}, $\rho = 1.2$ g/cm^3, and $c = 1.9$ J/g, calculations based on data from [9] show that the surface temperature of polymethyl methacrylate is equal to 498°C for a heat flow of $q = 70$ cal/(m^2 s). This result is consistent with experimental data from [9], where it was found by the linear pyrolysis method that the surface temperature of the polymethyl methacrylate samples is limited by a maximum value of $T_s \approx 500$°C, with an increase in the supplied heat flow. Thus, the temperature of the surfaces of samples slightly differs from the attainable superheating temperature of polymethyl methacrylate that is determined by independent methods (515–520°C), which corroborates the calculation results.

Function (6) is analyzed by the graphical method. Figure 1 shows the dependences $Q(T)$ for materials with the parameters $\frac{E}{R}$ = 17500 K, $B = 9 \times 10^{13}$ s^{-1}, ρ = 1.6 g/cm^3, $\lambda = 5.6 \times 10^4$ cal/cm, and $c = 0.35$ cal/(g K) taken from [10, 11] for nitrocellulose-based H powder and $\frac{E}{R}$ = 15000 K, $B = 6.3 \times 10^6$ s^{-1}, $\rho = 1.94$ g/cm^3, c = 0.3 cal/(g K), $f = 0.64$, and $\Delta T = 5$°C taken from [7] for ammonium perchlorate. As follows from drawing, the heat of the reaction $Q = 270$ cal/g is sufficient with a small reserve for approaching the surface temperature T_s to the attainable superheating temperature of the nitrocellulose-based compound T_l = 300°C. Such a result corresponds to the data presented in [10], where it was equal to 280–290°C.

According to the $Q(T)$ plots for ammonium perchlorate (Fig. 1, right part), the reaction heat $Q \approx$ 80–100 cal/g is insufficient for achieving the phase-state boundary (T_l = 495°C) at atmospheric pressure. The surface temperature can approach the phase-state boundary upon an increase in the reaction heat by 100–120 cal/g, a supply of an additional heat flow q of about 10 cal/(cm^2 s), or an increase in the initial temperature T_0. This result satisfactorily agrees with experimental data. As was noted in [13], "according to experiment, ammonium perchlorate can spontaneously burn (p = 1 atm) upon the supply of an additional heat of $\Delta Q \approx 100$ cal/g in the form of radiation energy, preheating, or small addition of fuel." In this case, the surface temperature is close to 500°C. This temperature is close to the attainable superheating of ammonium perchlorate, which is corroborated by the data from [14], where the tempera-

ture T_s of ammonium perchlorate samples reaches no more than 500°C as Q and velocity u increases by a factor of 7.

In addition to a rather large heat inflow to the region of the destruction of the condensed system, high heating rates are necessary for approaching the phase-state boundary. Let the substance concentration to the time of reaching temperature T be the fraction z of the initial concentration C_0 of the initial substance. Integrating the kinetic equation, we obtain

$$C = C_0 \exp\left(-\int_0^t k dt\right) = C_0 \exp\left(-\frac{1}{b}\int_{T_0}^T k dT\right) = zC_0$$

and

$$C = C_0 - \left(1 - \int_0^t k dt\right) = C_0 - \left(1 - \frac{1}{b}\int_{T_0}^T k dT\right) = zC_0$$

for $n = 1$ and 0, respectively. The integrals of the form $\int k\,dT$ with the Arrhenius dependence $k(T)$ are not expressed in terms of elementary functions. Using the method for approximately calculating such an integral [8] and substituting dependences $k(T)$ from Eqs. (4), we express the heating rate $b_{cal} = \frac{dT}{dt}$ that ensures the superheating of the condensed system above the beginning of transformation to a temperature of T_l as

$$b_{cal} = -\frac{RT_l^2 B}{E \ln z C_0} \exp\left(\frac{T}{T_l}\right)^n \exp\left(-\frac{E}{RT}\right). \quad (7)$$

Therefore, for $n = 0$,

$$b_{cal} = \frac{RT^2 B}{E} \exp\left(-\frac{E}{RT}\right). \quad (8)$$

We then calculate the heating rates for the condensed system that are necessary for reaching the phase-state boundary. The calculation by Eq. (12) shows that, to ensure the attainable superheating of the nitrocellulose-based compound, the heating rate must be no less than 1687 K/s. At the same time, actual rates of an increase in temperature upon combustion are much higher (about 10^5 K/s) and the conditions of attainable superheating are satisfied. For the attainable superheating of ammonium perchlorate, a heating rate of 2500 K/s is sufficient. At the same time, the actual heating rate upon the combustion of ammonium perchlorate is much higher (the average heating rate $\left(\frac{dT}{dt}\right)_{av}$ in the destruction front upon the combustion of ammonium perchlorate is determined by a ratio of $\frac{l}{u}$, where l is the front thickness, and is equal to about 10^5 K/s [11]), which ensures the combustion of ammonium perchlorate with reserve at a temperature close to attainable superheating. Under these conditions, Eq. (4) should be used for more accurate calculations of thermal processes.

To experimentally determine the conditions for the attainable superheating of nonvolatile substances, the pulse method is used to heat samples deposited as a thin layer on a filament heater [13–15] through which an electric current is transmitted. The heater simultaneously serves as a temperature sensor. Figure 2 shows the layout of the operation cell of the setup. The characteristic time of heating the 1-μm-thick layer deposited on the filament is equal to about 10^{-6} s, for which temperature over the entire thickness of the substance layer and filament is equalized with an accuracy of 2–3% [4]. The transparent body of the setup makes it possible to perform video filming or shooting of the processes of thermolysis of samples at normal and higher pressures. The accuracy of measurements of the attainable superheating temperature by the filament method increases upon measurement of the temperature difference between a sample and a reference substance deposited on the second section of the filament heater (the method of differential thermal analysis) [14].

Tests by the filament method enable a determination of the minimum heating rate necessary for reaching the vicinity of the phase-state boundary. To this end, experiments were carried out at various temperature increasing rates. In each experiment, the temperatures of the beginning and completion of the gasification process are recorded. At high heating rates, the difference between these temperatures was nearly absent. Figure 2 shows the filming pattern in the gasification stage of phenol formaldehyde resin. The time at which a cloud of condensed products from the thermal destruction of phenol formaldehyde resin is separated from the heater is clearly seen in this figure. These products then rise due to convection. Experiments with various heating rates showed that an increase in the heating rate of phenol formaldehyde resin samples above $b = 3700$ K/s does not shift the destruction process to higher temperatures, which indicates that the phase-state boundary is reached and corroborates the correctness of the calculation for the required heating rate. According to experiments, the maximum attainable superheating temperature at the gasification stage for phenol formaldehyde resin is equal to 750°C. The periodic weighting of the filament with a sample deposited on it at individual stages of heating enables one to analyze the kinetics of a decrease in the sample mass upon heating. Analysis of phenol formaldehyde resin samples before and after heating to the maximum temperature showed a decrease in the relative mass of the burned residual from 0.5 to 0.25 when the heating rate increases from 3 to 10^3 K/s, which indicates a change in the reaction

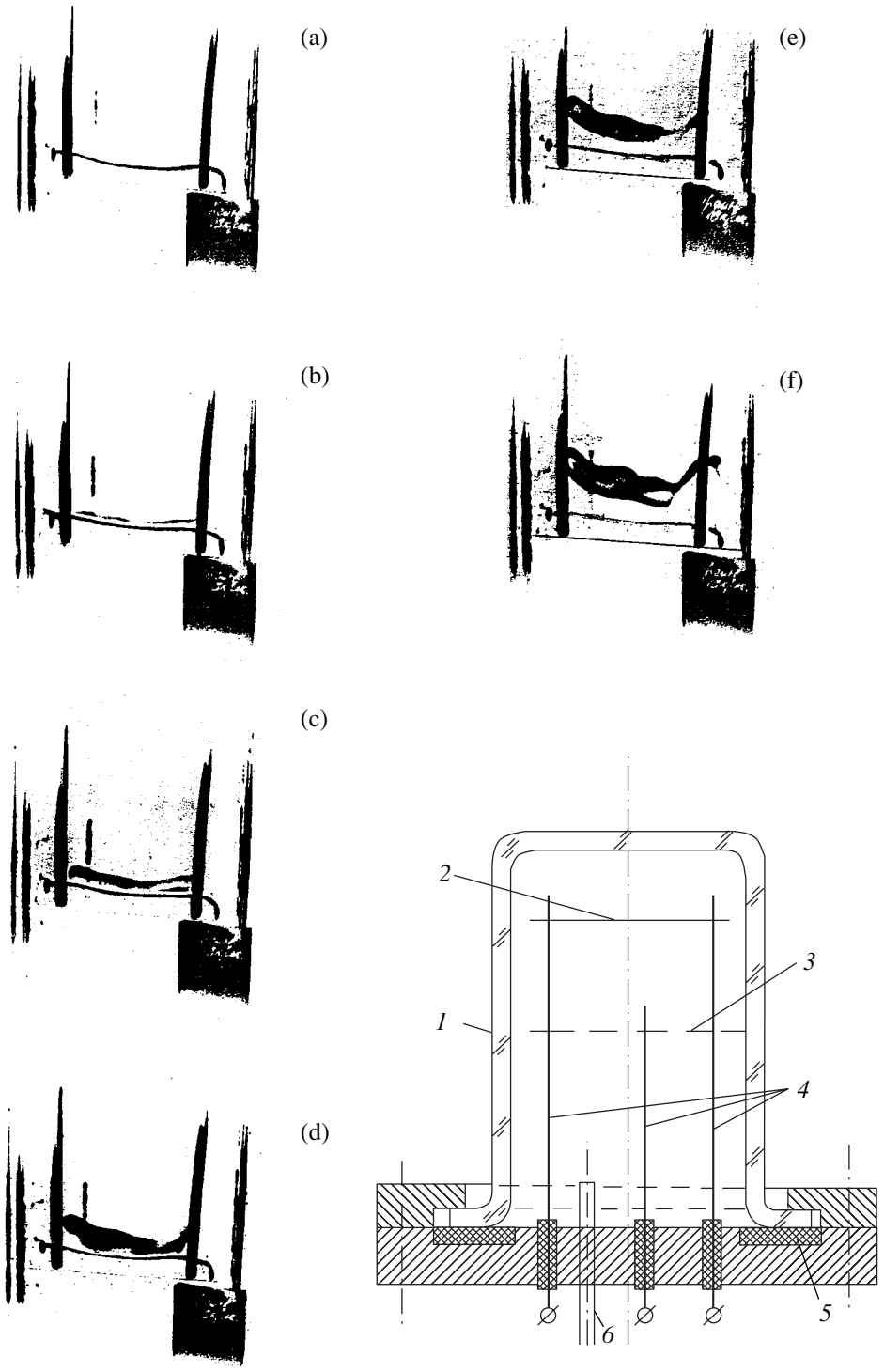

Fig. 2. Filming frames (a–f) of the process of the thermal destruction and gasification of phenol formaldehyde resin in a nitrogen medium (negative images). The arrow shows the time direction. The inset shows the layout of the operation cell (altitude chamber): (*1*) transparent body, (*2*) and (*3*) filaments for the thermal and differential thermal analysis, (*4*) contact bars, (*5*) seal assembly, and (*6*) connections for supplying compressed air and evacuation.

mechanism at high temperatures near the phase-state boundary.

Figure 3 shows the attainable superheating temperatures experimentally determined for certain substances and compounds by the method of contact thermal analysis [15]. The comparison of the results with the surface temperatures experimentally determined upon combustion of these materials shows that the tem-

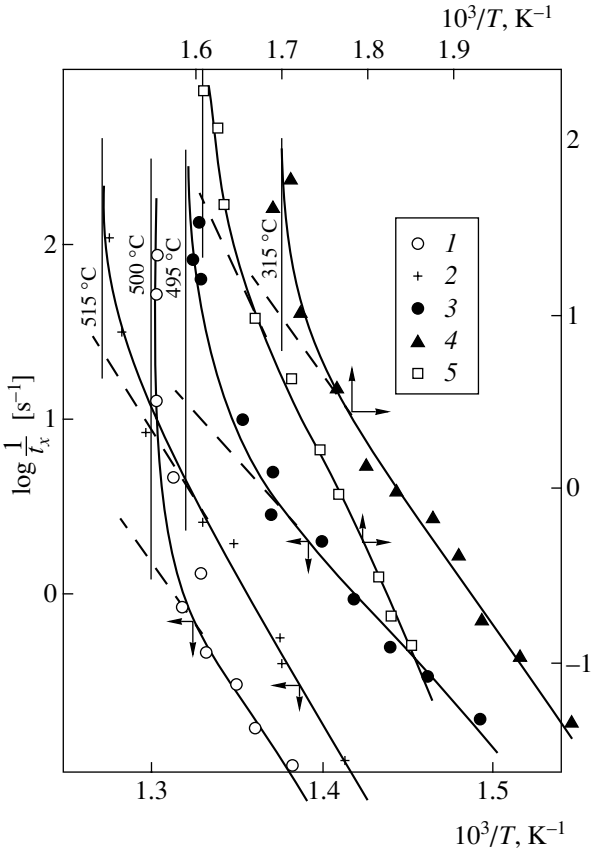

Fig. 3. Attainable superheating values determined by contact thermal analysis for (*1*) low-pressure polyethylene, (*2*) polymethyl methacrylate, (*3*) ammonium perchlorate, (*4*) H powder, and (*5*) HMX.

peratures of a combustion surface are always lower than the attainable superheating temperatures [9, 11, 12], which corroborates the results of the above analysis.

In summary, analytical expressions have been obtained for calculating the maximum heat flow and the heat of the thermal destruction reaction at the steady regime of the thermal destruction of condensed system that are necessary for reaching the phase-state boundary. Under these conditions, the temperature of the surfaces of condensed system samples subjected to intense heating approaches the attainable superheating temperature. The calculations satisfactorily agree with the published and newly obtained experimental data.

The minimum heating rates necessary for establishing the attainable superheating of polymethyl methacrylate, ammonium perchlorate, and phenol formaldehyde resin have been determined by heating samples from surfaces by intense heat flows. The calculations have been corroborated by experimental data.

REFERENCES

1. V. P. Skripov, E. N. Sinitsyn, P. A. Pavlov, *et al.*, *Thermophysical Properties of Liquids in the Metastable (Superheated) State* (Atomizdat, Moscow, 1980; Gordon and Breach, Amsterdam, 1988).
2. P. A. Pavlov, *Boiling Dynamics of Strongly Superheated Liquids* (Izd. UrO AN SSSR, Sverdlovsk, 1988) [in Russian].
3. E. D. Nikitin, P. A. Pavlov, and A. P. Popov, Teplofiz. Vys. Temp. **26** (3), 1091 (1988).
4. P. V. Skripov, S. B. Ryutin, V. P. Begishev, *et al.*, Inzh.-Fiz. Zh. **62** (2), 276 (1992).
5. V. A. Strunin, Zh. Fiz. Khim. **39** (2), 433 (1965).
6. D. A. Frank-Kamenetskiĭ, *Diffusion and Heat Transfer in Chemical Kinetics* (Nauka, Moscow, 1967; Plenum Press, New York, 1969).
7. O. F. Shlensky and Yu. V. Zelenev, Dokl. Akad. Nauk **385** (4), 482 (2002) [Dokl. Phys. **47**, 571 (2002)]; Erratum: Dokl. Phys. **47**, 905 (2002).
8. O. F. Shlensky and A. S. Lyapin, Dokl. Akad. Nauk **383** (2), 184 (2002) [Dokl. Phys. **47**, 176 (2002)].
9. R. M. Aseeva and G. E. Zaikov, *Combustion of Polymeric Materials* (Nauka, Moscow, 1981; Hanser, Munchen, 1985).
10. V. V. Aleksandrov and S. S. Khlevnoĭ, Prikl. Matem. Tekh. Fiz., No. 1, 158 (1970).
11. G. B. Manelis, G. M. Nazin, Yu. I. Rubtsov, and V. A. Strunin, *Thermal Decomposition and Combustion of Explosives and Powders* (Nauka, Moscow, 1996) [in Russian].
12. J. Powling and W. A. W. Smith, Combust. Flame **7**, 269 (1963).
13. N. V. Zhuravleva and Yu. I. Tolchinskiĭ, *Thermal Analysis of Organic and High-Molecular Compounds* (Khimiya, Moscow, 1983) [in Russian].
14. O. F. Shlensky and G. E. Vishnevskiĭ, Dokl. Akad. Nauk SSSR **279** (1), 105 (1984) [Sov. Phys. Dokl. **29**, 965 (1984)].
15. O. F. Shlensky, N. V. Afanas'ev, and A. G. Shashkov, *Thermal Destruction of Materials* (Énergoatomizdat, Moscow, 1996) [in Russian].

Translated by R. Tyapaev

Doklady Physics, Vol. 50, No. 2, 2005, pp. 77–82. Translated from Doklady Akademii Nauk, Vol. 400, No. 6, 2005, pp. 752–757.

TECHNICAL PHYSICS

Generalized Parametric Structural Model of a Compound Electromagnetoelastic Transducer

S. M. Afonin

Presented by Academician F.L. Chernous'ko July 13, 2004

Received July 14, 2004

The generalized parametric structural model and parametric structural circuit of a compound electromagnetoelastic transducer have been constructed. The effect of the geometric and physical parameters of the transducer and external load on its dynamic characteristics has been determined. The transfer functions of the compound electromagnetoelastic transducer for an electromechanical drive of nanometer displacements have been obtained.

INTRODUCTION. FORMULATION OF THE PROBLEM

The use of piezoelectric drives of nanometer displacements is a promising approach in nanotechnology, nanobiology, microelectronics, and adaptive optics to precision alignment and compensation of temperature and gravitational strains, as well as to atmospheric turbulence by correction of a wave front [1, 2]. The piezoelectric transducer of such a drive operates on the basis of the inverse piezoelectric effect; i.e., displacement is achieved by the application of electric voltage, which is caused by deformation of the piezoelectric transducer, in the range of several nanometers to several micrometers, with an accuracy of up to several tenths of a nanometer. A compound transducer is used to increase the displacement range to several tens of micrometers.

The parametric structural model of a simple piezoelectric transducer (piezoelectric plate and simple piezoelectric drive of nanometer displacements) is constructed by jointly solving the wave equation [3], the corresponding equation of the piezoelectric effect, and the boundary conditions on two loaded working surfaces of the simple piezoelectric transducer. The transfer functions of the simple piezoelectric transducer are determined from a system of equations describing its parametric structural model [4, 5].

The parametric structural model of the compound piezoelectric transducer is similarly developed by jointly solving a system of equations of the equivalent four-terminal compound piezoelectric transducer, the corresponding equation of the piezoelectric effect, and the boundary conditions on two loaded working surfaces of the piezoelectric transducer. The transfer functions of the compound piezoelectric transducer are also determined from a system of equations describing its parametric structural model [4].

GENERALIZED PARAMETRIC STRUCTURAL CIRCUIT OF THE ELECTROMAGNETOELASTIC TRANSDUCER

The equation of electromagnetoelasticity has the general form [3]

$$S_i = s_{ij}^{E,H,\Theta} T_j + d_{mi}^{H,\Theta} E_m + d_{mi}^{E,\Theta} H_m + \alpha_i^{E,H} d\Theta, \quad (1)$$

where S_i is the strain along the ith axis; $s_{ij}^{E,H,\Theta}$ is the elastic compliance for E = const, H = const, and Θ = const; T_j is the mechanical stress along the jth axis; $d_{mi}^{H,\Theta}$ is the piezoelectric modulus; E_m is the electric field along the mth axis; $d_{mi}^{E,\Theta}$ is the magnetostriction coefficient; H_m is the magnetic field along the mth axis; $\alpha_i^{E,H}$ is the thermal expansion coefficient; Θ is temperature; $i, j = 1, 2, \ldots, 6$; and $m = 1, 2, 3$.

For example, for separate action of electric and magnetic fields on the transducer at constant temperature, the following equations of electromagnetoelasticity are obtained [3]:

$$S_3 = d_{33}E_3 + s_{33}^E T_3$$

for the longitudinal piezoelectric effect,

$$S_1 = d_{31}E_3 + s_{11}^E T_1$$

for the transverse piezoelectric effect,

$$S_3 = d_{33}H_3 + s_{33}^H T_3$$

for the longitudinal magnetostriction,

Moscow State Institute of Electronic Engineering (Technical University), Zelenograd, Moscow oblast, 103498 Russia

1028-3358/05/5002-0077$26.00

$$S_1 = d_{31}H_3 + s_{11}^H T_1$$

for the transverse magnetostriction,

where S_3 and S_1 are the strains along the third and first axes, respectively; d_{33} and d_{31} are the longitudinal and transverse piezoelectric moduli, respectively; E_3 and H_3 are the electric and magnetic field strengths along the third axis, respectively; s_{33}^E and s_{11}^E (s_{33}^H and s_{11}^H) are the elastic compliances for E = const (H = const) along the third and first axes, respectively; and T_3 and T_1 are the mechanical stresses along the third and first axes, respectively.

As an example, let us consider problems of piezoelasticity. Jointly solving the matrix equation of the four-terminal compound piezoelectric transducer, the corresponding equation of the piezoelectric effect, and the boundary conditions on two loaded working surfaces of the piezoelectric transducer, we obtain the corresponding parametric structural model of the compound piezoelectric transducer. The matrix equation of strains and transfer functions of the compound electromagnetoelastic transducer are also determined from a system of equations describing its parametric structural model.

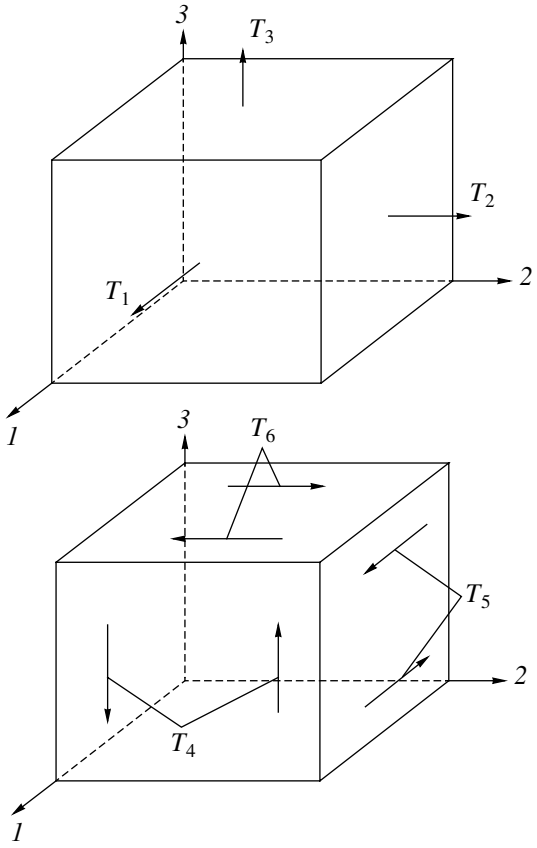

Fig. 1. Components of mechanical tension–compression and shear stresses in a piezoceramic body.

The stress state in a piezoceramic body is shown in Fig. 1 [5, 6]. If mechanical stress T is created in the elastic piezoceramic body, strain S linearly depending on T arises in that body. There are six components of stress T: T_1, T_2, and T_3 are tension–compression stresses, and T_4, T_5, and T_6 are shear stresses. Correspondingly, there are six components of strain S: S_1, S_2, S_3, S_4, S_5, and S_6. There is shear (Fig. 1) in planes perpendicular to axes 1, 2, and 3 [5].

Strain in a piezoelectric medium is generally written using the equation of the inverse piezoelectric effect [4, 5, 7] in the form

$$S_i = d_{mi}E_m + s_{ij}^E T_j \tag{2}$$

for voltage control and

$$S_i = g_{mi}D_m + s_{ij}^D T_j \tag{3}$$

for current control. Here, $i, j = 1, 2, \ldots, 6$; $m = 1, 2, 3$, where 1, 2, 3 are the mutually perpendicular coordinate axes; S_i is the strain with subscript i; d_{mi} and g_{mi} are the piezoelectric moduli; E_m and D_m are the electric field strength and electric displacement along the mth axis, respectively; s_{ij}^E and s_{ij}^D are the elastic compliance for E = const and D = const, respectively; and T_j is the mechanical stress with subscript j.

In a polarized ferroelectric ceramic material and TsTS or PZT piezoceramic material, there are five independent components of elastic compliances for E = const, s_{11}^E, s_{12}^E, s_{13}^E, s_{33}^E, and s_{55}^E, and three piezoelectric moduli, d_{31}, d_{33}, and d_{15} [5].

Let us consider a compound piezoelectric transducer consisting of piezoelectric plates connected electrically in parallel and mechanically in series. The compound piezoelectric transducer has a length of l upon the longitudinal piezoelectric effect, and each of its n piezoelectric plates has a height of δ and a cross section of S_0. Electrodes are placed on the faces of piezoelectric plates perpendicular to the third axis.

To derive a system of equation for the equivalent four-terminal compound piezoelectric transducer, we consider the corresponding matrix equations. The equivalent T-shaped four-terminal circuit of the kth piezoelectric plate in the series equivalent circuit of the compound piezoelectric transducer in Fig. 2 has the ordinal number k and is composed using the equation of oscillations and equation of forces [4–10] acting on the faces of piezoelectric plates.

Thus, we obtain the Laplace transforms [10] of the corresponding forces on the input and output faces of the kth piezoelectric plate in the form of a system of

equations for the equivalent T-shaped four-terminal circuit (Fig. 2):

$$\begin{aligned} F_{k_{\text{inp}}}(p) &= -(Z_1 + Z_2)\Xi_k(p) + Z_2\Xi_{k+1}(p), \\ -F_{k_{\text{out}}}(p) &= -Z_2\Xi_k(p) + (Z_1 + Z_2)\Xi_{k+1}(p), \end{aligned} \quad (4)$$

where

$$Z_1 = \frac{S_0\gamma\tanh(\delta\gamma)}{s_{ij}^{\Psi}}, \quad Z_2 = \frac{S_0\gamma}{s_{ij}^{\Psi}\sinh(\delta\gamma)},$$

$$\gamma = \frac{p}{c} + \alpha, \quad \Psi = \{E, D\}$$

$F_{k_{\text{inp}}}(p)$ and $F_{k_{\text{out}}}(p)$ are the Laplace transforms of the forces on the input and output faces of the kth piezoelectric plate in the compound piezoelectric transducer, respectively; Z_1 and Z_2 are the resistances of the equivalent four-terminal device; $\Xi_k(p)$ and $\Xi_{k+1}(p)$ are the Laplace transforms of the displacements on the input and output faces of the kth piezoelectric plate, respectively; p is the Laplace operator; γ is the wave-propagation coefficient; c is the speed of sound in the piezoceramic material; α is the damping coefficient; Ψ is the generalized parameter of the electric field, i.e., electric-field strength E or electric displacement D; s_{ij}^{Ψ} is the elastic compliance for Ψ = const; and $i, j = 1, 2, \ldots, 6$. From these equations, we obtain the following system for the kth piezoelectric plate:

$$-F_{k_{\text{inp}}} = \left(1 + \frac{Z_1}{Z_2}\right)F_{k_{\text{out}}} + Z_1\left(2 + \frac{Z_1}{Z_2}\right)\Xi_{k+1},$$

$$\Xi_k = \frac{1}{Z_1}F_{k_{\text{out}}} + \left(1 + \frac{Z_1}{Z_2}\right)\Xi_{k+1},$$

which is equivalent to the matrix equation

$$\begin{Vmatrix} -F_{k_{\text{inp}}} \\ \Xi_k \end{Vmatrix} = \|M\| \begin{Vmatrix} F_{k_{\text{out}}} \\ \Xi_{k+1} \end{Vmatrix}. \quad (5)$$

Here,

$$\|M\| = \begin{Vmatrix} m_{11} & m_{12} \\ m_{21} & m_{22} \end{Vmatrix} = \begin{Vmatrix} 1 + \dfrac{Z_1}{Z_2} & Z_1\left(2 + \dfrac{Z_1}{Z_2}\right) \\ \dfrac{1}{Z_2} & 1 + \dfrac{Z_1}{Z_2} \end{Vmatrix},$$

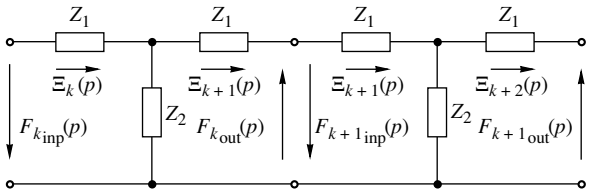

Fig. 2. Equivalent series circuit for the compound piezoelectric transducer.

where

$$m_{11} = m_{22} = 1 + \frac{Z_1}{Z_2} = \cosh\gamma\delta,$$

$$m_{12} = Z_1\left(2 + \frac{Z_1}{Z_2}\right) = Z_0\sinh\gamma\delta,$$

$$m_{21} = \frac{1}{Z_2} = \frac{\sinh\gamma\delta}{Z_0}, \quad Z_0 = \frac{S_0\gamma}{s_{ij}^{\Psi}}.$$

For the compound piezoelectric transducer, the Laplace transforms $\Xi_{k+1}(p)$ and $F_{k_{\text{out}}}(p)$ of the displacement and force, respectively, on the output face of the kth plate (Fig. 2) correspond to the respective Laplace transforms of the displacement and force on the input face of the $(k + 1)$th plate [4–10]. The force $F_{k_{\text{out}}}$ on the output face of the kth plate is equal in magnitude and opposite in direction to the force $F_{k+1_{\text{inp}}}$ on the input face of the $(k + 1)$th plate:

$$F_{k_{\text{out}}}(p) = -F_{k+1_{\text{inp}}}(p).$$

From matrix equation (5) for n plates in the compound piezoelectric transducer, we obtain the matrix equation

$$\begin{Vmatrix} -F_{1_{\text{inp}}} \\ \Xi_1 \end{Vmatrix} = \|M\|^n \begin{Vmatrix} F_{n_{\text{out}}} \\ \Xi_n \end{Vmatrix}. \quad (6)$$

By mathematical induction, the elements of the matrix $\|M\|^n$ are determined as

$$\|M\|^n = \begin{Vmatrix} \cosh(n\gamma\delta) & Z_0\sinh(n\gamma\delta) \\ \dfrac{\sinh(n\gamma\delta)}{Z_0} & \cosh(n\gamma\delta) \end{Vmatrix}.$$

Matrix equation (6) for the compound piezoelectric transducer with the expression for the matrix $\|M\|^n$ corresponds to the equivalent four-terminal compound piezoelectric transducer.

The equations of forces acting on the faces of the compound piezoelectric transducer have the form

$$T_3(0, p)S_0 = F_1(p) + M_1p^2\Xi_1(p) \text{ for } x = 0,$$

$$T_3(l, p)S_0 = -F_2(p) - M_2p^2\Xi_2(p) \text{ for } x = l,$$

where $T_3(0, p)$ and $T_3(l, p)$ are the Laplace transforms of mechanical stresses on two faces of the compound piezoelectric transducer, and $\Xi_2(p)$ and $F_2(p)$ are the Laplace transforms of the displacement and force, respectively, on the $x = l$ face of the piezoelectric transducer.

Let us construct a mathematical model of the compound piezoelectric transducer for the longitudinal piezoelectric effect and voltage control. In this case, the Laplace transform of the force [4] that drives the oscillations of the compound piezoelectric transducer, is obtained from equation (2) of the inverse piezoelectric effect as

$$F(p) = \frac{d_{33}S_0E_3(p)}{s_{33}^E}.$$

Jointly considering the system of equations for the equivalent four-terminal compound piezoelectric transducer with voltage control, the equation of force on the faces of the compound piezoelectric transducer, and the equation of force stimulating oscillations gives the following system of equations describing the parametric structural model of the compound piezoelectric transducer for the longitudinal piezoelectric effect:

$$\Xi_1(p) = \frac{1}{M_1p^2}\left\{-F_1(p) + \frac{1}{\chi_{33}^E}\left[d_{33}E_3(p)\right.\right.$$

$$\left.\left. - \frac{\gamma}{\sinh(l\gamma)}[\cosh(l\gamma)\Xi_1(p) - \Xi_2(p)]\right]\right\},$$

$$\Xi_2(p) = \frac{1}{M_2p^2}\left\{-F_2(p) + \frac{1}{\chi_{33}^E}\left[d_{33}E_3(p)\right.\right.$$

$$\left.\left. - \frac{\gamma}{\sinh(l\gamma)}[\cosh(l\gamma)\Xi_2(p) - \Xi_1(p)]\right]\right\}.$$

Here,

$$\frac{1}{\chi_{33}^E} = \frac{S_0}{s_{33}^E} = \frac{m_c(c^E)^2}{l},$$

where m_c is the mass of the compound piezoelectric transducer.

Thus, taking into consideration generalized piezoelectric equation (1), we arrive at the following system of equations describing the generalized parametric structural model of the piezoelectric transducer:

$$\Xi_1(p) = \frac{1}{M_1p^2}\left\{-F_1(p) + \frac{1}{\chi_{ij}^\Psi}\left[\nu_{mi}\Psi_m(p)\right.\right.$$

$$\left.\left. - \frac{\gamma}{\sinh(l\gamma)}[\cosh(l\gamma)\Xi_1(p) - \Xi_2(p)]\right]\right\},$$

$$\Xi_2(p) = \frac{1}{M_2p^2}\left\{-F_2(p) + \frac{1}{\chi_{ij}^\Psi}\left[\nu_{mi}\Psi_m(p)\right.\right.$$

$$\left.\left. - \frac{\gamma}{\sinh(l\gamma)}[\cosh(l\gamma)\Xi_2(p) - \Xi_1(p)]\right]\right\}. \quad (7)$$

Here,

$$\nu_{mi} = \begin{cases} d_{33}, d_{31}, d_{15} \\ g_{33}, g_{31}, g_{15}, \\ d_{33}, d_{31}, d_{15} \end{cases} \quad \Psi_m = \begin{cases} E_3, E_1 \\ D_3, D_1, \\ H_3, H_1 \end{cases}$$

$$s_{ij}^\Psi = \begin{cases} s_{33}^E, s_{11}^E, s_{55}^E \\ s_{33}^D, s_{11}^D, s_{55}^D, \\ s_{33}^H, s_{11}^H, s_{55}^H \end{cases} \quad c = \begin{cases} c^E \\ c^D, \\ c^H \end{cases} \quad \gamma = \begin{cases} \gamma^E \\ \gamma^D, \\ \gamma^H \end{cases}$$

where the upper lines and superscripts E, D, and H correspond to voltage, current, and magnetic-field controls, respectively, and

$$\frac{1}{\chi_{ij}^\Psi} = \frac{S_0}{s_{ij}^\Psi}.$$

System of equations (7) corresponds to the generalized parametric structural circuit of the piezoelectric transducer (Fig. 3).

GENERALIZED TRANSFER FUNCTIONS OF THE PIEZOELECTRIC TRANSDUCER

After algebraic reformulation, the generalized structural parametric model of the piezoelectric transducer enables one to calculate the transfer functions of the piezoelectric transducer as the ratio of the Laplace transform in the displacement of the piezoelectric transducer face to the Laplace transform in the corresponding input electric parameter, or to the Laplace transform of the corresponding force for zero initial conditions. The joint solution of the above equations

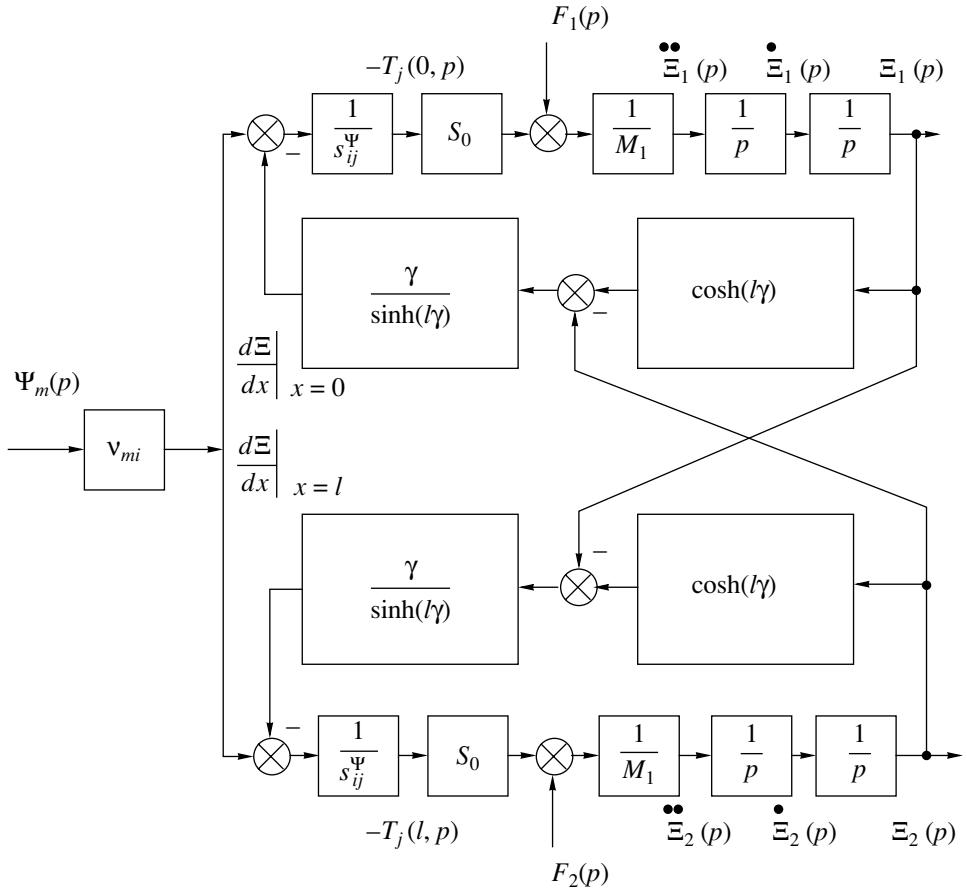

Fig. 3. Generalized parametric structural circuit of the electromagnetoelastic transducer.

for the Laplace transforms in the displacement of two faces of the piezoelectric transducer gives

$$\begin{aligned}\Xi_1(p) &= W_{11}(p)\Psi_m(p)\\ &+ W_{12}(p)F_1(p) + W_{13}(p)F_2(p),\\ \Xi_2(p) &= W_{21}(p)\Psi_m(p)\\ &+ W_{22}(p)F_1(p) + W_{23}(p)F_2(p),\end{aligned} \tag{8}$$

where the generalized transfer functions of the piezoelectric transducer have the form

$$W_{11}(p) = \frac{\Xi_1(p)}{\Psi_m(p)} = \frac{\nu_{mi}}{A_{ij}}\left[M_2\chi_{ij}^{\Psi}p^2 + \gamma\tanh\left(\frac{l\gamma}{2}\right)\right],$$

$$A_{ij} = M_1M_2(\chi_{ij}^{\Psi})^2p^4 + \frac{(M_1 + M_2)\chi_{ij}^{\Psi}}{c\tanh(l\gamma)}p^3$$

$$+\left[\frac{(M_1 + M_2)\chi_{ij}^{\Psi}\alpha}{\tanh(l\gamma)} + \frac{1}{c^2}\right]p^2 + \frac{2\alpha}{c}p + \alpha^2,$$

$$W_{21}(p) = \frac{\Xi_2(p)}{\Psi_m(p)} = \frac{\nu_{mi}}{A_{ij}}\left[M_1\chi_{ij}^{\Psi}p^2 + \gamma\tanh\left(\frac{l\gamma}{2}\right)\right],$$

$$W_{12}(p) = \frac{\Xi_1(p)}{F_1(p)} = -\frac{\chi_{ij}^{\Psi}}{A_{ij}}\left[M_2\chi_{ij}^{\Psi}p^2 + \frac{\gamma}{\tanh(l\gamma)}\right],$$

$$W_{13}(p) = \frac{\Xi_1(p)}{F_2(p)} = W_{22}(p) = \frac{\Xi_2(p)}{F_1(p)} = \frac{\chi_{ij}^{\Psi}\gamma}{A_{ij}\sinh(i\gamma)},$$

$$W_{23}(p) = \frac{\Xi_2(p)}{F_2(p)} = -\frac{\chi_{ij}^{\Psi}}{A_{ij}}\left[M_1\chi_{ij}^{\Psi}p^2 + \frac{\gamma}{\tanh(l\gamma)}\right].$$

Thus, from a system of equations (8), we obtain the generalized parametric structural circuit of the piezoelectric transducer (Fig. 3) and the matrix equation

$$\begin{Vmatrix}\Xi_1(p)\\ \Xi_2(p)\end{Vmatrix} = \begin{Vmatrix}W_{11}(p) & W_{12}(p) & W_{13}(p)\\ W_{21}(p) & W_{22}(p) & W_{23}(p)\end{Vmatrix}\begin{Vmatrix}\Psi_m(p)\\ F_1(p)\\ F_2(p)\end{Vmatrix}.$$

CONCLUSIONS

The generalized parametric structural model developed for the electromagnetoelastic transducer makes it possible to determine its generalized parametric struc-

tural circuit and generalized transfer functions and to use methods of automatic-control theory for calculations of the dynamic and static electromechanical characteristics of the electromagnetoelastic transducer for a drive of nanometer displacements.

REFERENCES

1. S. M. Afonin, Prib. Sist. Upr., No. 2, 41 (1998).
2. S. M. Afonin, Izv. Ross. Akad. Nauk: Mekh. Tverd. Tela, No. 6, 97 (2003).
3. S. M. Afonin, Izv. Ross. Akad. Nauk: Mekh. Tverd. Tela, No. 6, 101 (2002).
4. *Physical Acoustics: Principles and Methods*, Vol. 1, Part A: *Methods and Devices*, Ed. by W. P. Mason (Academic, New York, 1964; Mir, Moscow, 1966).
5. K. Okadzaki, *Technology of Ceramic Dielectrics* (Énergiya, Moscow, 1976) [in Russian].
6. V. I. Feodos'ev, *Strength of Materials* (Izd. MGTU im. N. É. Baumana, Moscow, 2003) [in Russian].
7. V. I. Domarkas and R.-I. Yu. Kazhis, *Testing–Measuring Piezoelectric Transducers* (Mintis, Vilnus, 1975) [in Russian].
8. S. M. Targ, *Theoretical Mechanics: A Short Course* (Nauka, Moscow, 1970) [in Russian].
9. I. M. Babakov, *Theory of Vibration* (Nauka, Moscow, 1968) [in Russian].
10. A. D. Polyanin, *Handbook of Linear Mathematical Physics Equations* (Fizmatlit, Moscow, 2001) [in Russian].

Translated by R. Tyapaev

Doklady Physics, Vol. 50, No. 2, 2005, pp. 83–87. Translated from Doklady Akademii Nauk, Vol. 400, No. 4, 2005, pp. 475–479.

MECHANICS

An Approach to the Experimental Determination of the Bending Stiffness of Nanosize Shells

E. A. Ivanova* and Academician N. F. Morozov**

Received October 15, 2004

The problem of the experimental determination of elastic moduli of nanoscale objects is of present interest. The determination of the elastic moduli of thin macroscopic shells is usually based on experiments with plates. It is known that, when grown using certain techniques, nanoobjects are obtained only in the form of shells. Therefore, it is necessary to develop a method for determining the elastic moduli of nanoobjects on the basis of experiments with shells. Experimental determination of the bending stiffness of nanosize shells presents a serious problem, because for such widespread nanoobjects as nanotubes and fullerenes under arbitrary deformation, the material is subjected to both bending and tension. Therefore, all parameters (e.g., natural frequencies) that can be measured directly are complicated functions of both bending and tension stiffness. In recent years, together with nanotubes and fullerenes, nanoobjects of a more intricate configuration have been obtained [1–4]. Nanosize cylindrical helices [1, 3] are of particular interest in connection with the possible experimental determination of bending stiffness. This is due to the fact that (1) in helical shells under arbitrary deformation, the material is mainly bent, so that the material tension effect can be neglected when interpreting experimental data; and (2) the natural oscillation shapes of helical shells are much more easily observed than those of cylindrical shells associated with pure bending of the material. The latter statement is illustrated in Fig. 1, which presents the first four helical shell oscillation shapes. The analysis of helical shell dynamics [5] presented below may be a theoretical foundation for experimental testing of the applicability of the continuum theory to (a) the calculation of mechanical characteristics of nanoobjects and (b) the experimental determination of the bending stiffness of nanoshells.

* *St. Petersburg Technical University, ul. Politekhnicheskaya 29, St. Petersburg, 195251 Russia*
e-mail: ivanova@EI5063.spb.edu

** *St. Petersburg State University (Petrodvorets Branch), pl. Bibliotechnaya 2, Petrodvorets, 198904 Russia*
e-mail: morozov@NM1016.spb.edu

BASIC EQUATIONS OF THIN SHELL THEORY

We present here a summary of basic equations from the classical linear theory of shells. For the sake of brevity, we use the apparatus of direct tensor calculus [6, 7]. The dynamic equations have the form

$$\nabla \cdot \underline{\underline{T}} = \rho \ddot{\underline{u}}, \quad \nabla \cdot \underline{\underline{M}} + \underline{\underline{T}}_{\times} = 0, \tag{1}$$

where $\underline{\underline{T}}$ and $\underline{\underline{M}}$ are the force and momentum tensors, respectively; $(\,)_{\times}$ is the vector invariant of a tensor; ρ is the surface mass density; and $\underline{u}$ is the displacement vector. In the classical theory of shells, the transverse shear strain vector is assumed to be zero. Thus, the angle-of-rotation vector $\underline{\varphi}$ can be expressed in terms of the displacement vector as

$$\underline{\varphi} = -\underline{n} \times (\nabla \underline{u}) \cdot \underline{n}, \tag{2}$$

where $\underline{n}$ is the unit normal vector to the shell surface. The transverse force vector $\underline{N} \equiv \underline{\underline{T}} \cdot \underline{n}$ is determined from dynamic equations (1). The elasticity equation for the force tensor in the tangent plane $\underline{\underline{T}} \cdot \underline{\underline{a}}$ has the form

$$\underline{\underline{T}} \cdot \underline{\underline{a}} + \frac{1}{2}(\underline{\underline{M}} \cdot\cdot \underline{\underline{b}})\underline{\underline{c}} = {}^4\underline{\underline{A}} \cdot\cdot \underline{\underline{\varepsilon}}. \tag{3}$$

The elasticity equation for the momentum tensor $\underline{\underline{M}}$

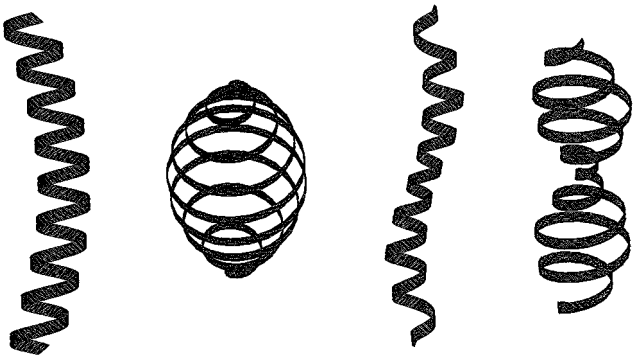

Fig. 1. Oscillation shapes of a helical cylindrical shell.

1028-3358/05/5002-0083$26.00

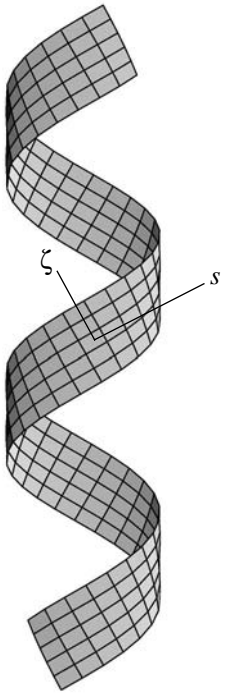

Fig. 2. Helical cylindrical shell.

has the form

$$\underline{\underline{M}}^T = {}^4\underline{\underline{C}} \cdot\cdot \underline{\underline{\kappa}}. \quad (4)$$

Here ${}^4\underline{\underline{A}}$ and ${}^4\underline{\underline{C}}$ are the shell stiffness tensors, $\underline{\underline{a}}$ is the unit tensor in the tangent plane, $\underline{\underline{b}} = -\nabla\underline{n}$, $\underline{\underline{c}} = -\underline{\underline{a}} \times \underline{n}$, and the tension–shear strain tensor $\underline{\underline{\varepsilon}}$ in the tangent plane and the bending–torsion strain tensor $\underline{\underline{\kappa}}$ are calculated by the formulas

$$\underline{\underline{\varepsilon}} = \frac{1}{2}((\nabla\underline{u}) \cdot \underline{\underline{a}} + \underline{\underline{a}} \cdot (\nabla\underline{u})^T),$$
$$\underline{\underline{\kappa}} = (\nabla\underline{\varphi}) \cdot \underline{\underline{a}} + \frac{1}{2}((\nabla\underline{u}) \cdot\cdot \underline{\underline{c}})\underline{\underline{b}}. \quad (5)$$

HELICAL SHELL GEOMETRY

We will consider a cylindrical helical shell (Fig. 2) of radius R with helix angle α, helix-forming band length l, band width a, and band thickness h. Shell kinematics will be described below using two coordinate systems: a cylindrical coordinate system $r \equiv R$, φ, z, where the z axis is directed along the helix axis; and a curvilinear coordinate system s, ζ introduced on the shell surface as follows:

$$z = R(\sin\alpha s + \cos\alpha\zeta), \quad \varphi = \cos\alpha s - \sin\alpha\zeta. \quad (6)$$

The dimensionless coordinates s and ζ vary within the following limits

$$-\frac{l}{2} \le Rs \le \frac{l}{2}, \quad -\frac{a}{2} \le R\zeta \le \frac{a}{2}. \quad (7)$$

The unit vectors $\underline{e}_s$ and $\underline{e}_\zeta$ directed along the coordinate lines and the unit vector $\underline{n}$ determining the direction of the outward normal to the shell surface have the form

$$\underline{e}_s = \cos\alpha\underline{e}_\varphi + \sin\alpha\underline{k},$$
$$\underline{e}_\zeta = -\sin\alpha\underline{e}_\varphi + \cos\alpha\underline{k}, \quad \underline{n} = \underline{e}_r. \quad (8)$$

APPROXIMATE EQUATIONS GOVERNING THE DYNAMICS OF A THIN HELICAL SHELL

It is known that the tensor ${}^4\underline{\underline{A}}$ of the tension–shear stiffness of the shell in the tangent plane is proportional to the shell thickness h, while the tensor ${}^4\underline{\underline{C}}$ of the bending–torsion stiffness is proportional to h^3. Therefore, in the case $\frac{h}{a} \ll 1$ and $\frac{h}{l} \ll 1$, the helical shell under consideration can be treated as inextensible. Thus, we will assume that the tension–shear strain tensor in the tangent plane is equal to zero

$$\underline{\underline{\varepsilon}} = 0. \quad (9)$$

In this case ${}^4\underline{\underline{A}} \to \infty$, elasticity equation (3) becomes meaningless, and the force tensor in the tangent plane $\underline{\underline{T}} \cdot \underline{\underline{a}}$ is determined from dynamic equations (1) with regard to the strain compatibility equation

$$\Delta(\mathrm{tr}(\underline{\underline{T}} \cdot \underline{\underline{a}})) - (1+\nu)\nabla \cdot (\nabla \cdot (\underline{\underline{T}} \cdot \underline{\underline{a}})) = 0, \quad (10)$$

where ν is the Poisson's ratio. We note that the continuity equation (10) follows from the assumption that the tension–shear strain is absent in the tangent plane. Thus, the problem is reduced to the solution of the system of equations (1), (2), (4), (5), (9), and (10), where the bending–torsion stiffness tensor ${}^4\underline{\underline{C}}$ has the form

$${}^4\underline{\underline{C}} = D\left[\frac{1+\nu}{2}\underline{\underline{c}}\underline{\underline{c}} + \frac{1-\nu}{2}(\underline{\underline{a}}_2\underline{\underline{a}}_2 + \underline{\underline{a}}_4\underline{\underline{a}}_4)\right]. \quad (11)$$

Here D is the bending stiffness of the shell, $\underline{\underline{a}}_2 = \underline{e}_s\underline{e}_s - \underline{e}_\zeta\underline{e}_\zeta$, and $\underline{\underline{a}}_4 = \underline{e}_s\underline{e}_\zeta + \underline{e}_\zeta\underline{e}_s$.

SOLUTION OF THE DYNAMIC EQUATIONS FOR A THIN HELICAL SHELL

The displacement vector is represented in the form of the decomposition in the $\underline{u} = u_s\underline{e}_s + u_\zeta\underline{e}_\zeta + w\underline{n}$ basis. The displacement w along the normal to the shell surface is chosen as the main variable. Using rather simple transformations, we reduce the equations of shell motion to the single differential equation

$$\left(\sin^2\alpha\frac{\partial^4}{\partial s^4} + \cos^2\alpha\frac{\partial^4}{\partial\zeta^4} - \frac{1}{4}\frac{\partial^4}{\partial s^2\partial\zeta^2}\right) \times\left[\frac{D}{\rho R^4}(\tilde{\Delta}+1)^2 w + \ddot{w}\right] - \frac{\sin^2 2\alpha}{4}\tilde{\Delta}\ddot{w} = 0, \tag{12}$$

where $\tilde{\Delta} \equiv R^2\Delta$ is the dimensionless Laplace operator. Representing condition (9) of the absence of tension–shear strain from the tangent plane in the coordinate form, we obtain the following relationship between the displacement vector components:

$$\frac{\partial u_s}{\partial s} = -\cos^2\alpha w, \quad \frac{\partial u_\zeta}{\partial\zeta} = -\sin^2\alpha w, \quad \frac{\partial u_\zeta}{\partial s} + \frac{\partial u_s}{\partial\zeta} = \sin 2\alpha w \tag{13}$$

and arrive at the following the strain compatibility equation in displacements:

$$\sin 2\alpha\frac{\partial^2 w}{\partial s\partial\zeta} + \sin^2\alpha\frac{\partial^2 w}{\partial s^2} + \cos^2\alpha\frac{\partial^2 w}{\partial\zeta^2} = 0. \tag{14}$$

We note that Eq. (14) is a direct consequence of Eqs. (13).

Thus, the problem is reduced to the determination of solutions of dynamic equations (12) that satisfy an additional constraint imposed by strain compatibility equation (14). In the cylindrical coordinates [see Eqs. (6)], strain compatibility equation (14) takes the form

$$\frac{\partial^2 w}{\partial z^2} = 0. \tag{15}$$

The solutions of dynamic equation (12) that satisfy strain compatibility equation (15) can obviously be represented as

$$w(\varphi, z, t) = W(\varphi, z)e^{i\omega t}, \quad W(\varphi, z) = zW_1(\varphi) + W_2(\varphi). \tag{16}$$

Substituting expressions (16) into dynamic equation (12) and equating the coefficients of different powers of z to zero, we obtain the system of two differential equations in the variables $W_1(\varphi)$ and $W_2(\varphi)$. Solving this system and returning to the variables s and ζ, we obtain

$$W(s,\zeta) = \sum_{j=1}^{3}[(A_j^s(p_j s + q_j\zeta) + B_j^s) \times\sin[\lambda_j(\cos\alpha s - \sin\alpha\zeta)] + (A_j^c(p_j s + q_j\zeta) + B_j^c) \times\cos[\lambda_j(\cos\alpha s - \sin\alpha\zeta)]], \tag{17}$$

$$p_j = \sin\alpha - \beta_j, \quad q_j = \cos\alpha + \beta_j,$$

$$\beta_j = \frac{2\cos 2\alpha\Omega^2}{9\cos\alpha(\lambda_j^4 + (\Omega^2 - 1)\lambda_j^2 + 2\Omega^2)},$$

where A_j^s, B_j^s, A_j^c, and B_j^c are arbitrary constants and λ_j are the roots of the characteristic equation

$$\lambda^6 - 2\lambda^4 + (1-\Omega^2)\lambda^2 - \frac{4}{3}\Omega^2 = 0, \ \Omega = \sqrt{\frac{\rho R^4}{D}}\omega. \tag{18}$$

Here, Ω is the dimensionless natural frequency; for its determination, some boundary conditions should be formulated. As follows from Eqs. (17) and (18), the dimensionless frequency Ω is independent of the physical characteristics of the shell ρ and D if these parameters do not enter into the boundary conditions.

FORMULATION OF THE BOUNDARY CONDITIONS. DETERMINATION OF THE NATURAL FREQUENCIES OF OSCILLATIONS OF A THIN HELICAL SHELL

In accordance with Eq. (17), the function $W(s, \zeta)$ involves twelve constants, which, naturally, make it impossible to satisfy all the boundary conditions of the classical theory of shells. However, the formulation of twelve homogeneous equations specifying the displacements or stresses at any point of the boundary is sufficient for a formal solution of the problem within the framework of the simplified formulation under consideration.

We will assume that the shell is fixed at corners; i.e., the displacement vector $\underline{u}(s, \zeta, t) = \underline{u}_*(s, \zeta)e^{i\omega t}$ is zero at the corner points

$$\underline{u}_*\left(\frac{l}{2R}, \frac{a}{2R}\right) = 0, \quad \underline{u}_*\left(-\frac{l}{2R}, \frac{a}{2R}\right) = 0, \quad \underline{u}_*\left(\frac{l}{2R}, -\frac{a}{2R}\right) = 0, \quad \underline{u}_*\left(-\frac{l}{2R}, -\frac{a}{2R}\right) = 0. \tag{19}$$

From the condition that the determinant of system (19) is equal to zero, we obtain the frequency equation. As

can be seen from Eqs. (13) and (15)–(18), the determinant of system (19) depends on the dimensionless frequency Ω and three dimensionless parameters α, $\frac{l}{R}$, and $\frac{a}{R}$. Therefore, the solution of the frequency equation represents a spectrum of dimensionless natural frequencies of the form

$$\Omega_n = \Omega_n\left(\alpha, \frac{l}{R}, \frac{a}{R}\right), \quad n = 1, 2, \ldots. \tag{20}$$

Numerical calculations of the natural frequencies and shapes of helical shell oscillations with the dimensionless parameters $\alpha = \frac{\pi}{6}$, $\frac{l}{R} = 20\pi$, and $\frac{a}{R}$ =1 showed that the approximate theory specified by Eqs. (17)–(19) adequately describes low-frequency oscillations.

DISCUSSION OF THE RESULTS

We will consider two thin helical shells with different physical and geometric characteristics but the same dimensionless parameters α, $\frac{l}{R}$, and $\frac{a}{R}$. We will assume that both shells are fixed at corners; i.e., boundary conditions (19) apply. In this case, in accordance with Eq. (20), the spectra of the dimensionless natural frequencies of shells under consideration coincide with

$$\forall n: \ \Omega_n^{(1)} = \Omega_n^{(2)}. \tag{21}$$

Then, in accordance with Eq. (18), the natural frequency ratio $\frac{\omega_n^{(1)}}{\omega_n^{(2)}}$ is independent of their ordinal number n

$$\frac{\omega_n^{(1)}}{\omega_n^{(2)}} = \sqrt{\frac{D_2\rho_1 R_1^4}{D_1\rho_2 R_2^4}}. \tag{22}$$

Relation (22) may serve as a theoretical basis for the experimental investigation of the applicability of the continuum theory to nanoobjects and, if the answer is affirmative, for experimental determination of the bending stiffness of nanoshells.

EXPERIMENTAL TESTING OF THE APPLICABILITY OF THE CONTINUUM THEORY TO NANOSCALE OBJECTS

To test the applicability of the continuum theory to nanoobjects, the following measurements can be performed:

(1) several first natural frequencies of a helical nanoshell are measured;

(2) the natural frequencies of a macroscopic helical shell with the same dimensionless parameters α, $\frac{l}{R}$, and $\frac{a}{R}$ and the same fixation conditions are measured;

(3) the measured frequency ratios $\delta_n = \frac{\omega_n^{(1)}}{\omega_n^{(2)}}$ are calculated.

If the continuum theory is applicable to nanoobjects, then the equality $\delta_n = \delta_1$ theoretically holds true for any n. The applicability condition for the continuum theory is really formulated as the inequality $\frac{|\delta_n - \delta_1|}{\delta_1} \le \varepsilon_N$, which must be fulfilled for $\forall n \le N$. The permissible error ε_N can be estimated by comparing with the results of an analogous experiment performed with two macroscopic helical shells.

EXPERIMENTAL DETERMINATION OF THE BENDING STIFFNESS OF NANOSHELLS

If the continuum theory is applicable to nanoobjects, then formula (22) makes it possible to experimentally determine the bending stiffness of a nanoshell. In order to determine the bending stiffness, it is necessary:

(1) to measure the first natural frequency $\omega_1^{(1)}$ of the helical nanoshell;

(2) to measure the mass m_1 and the geometric dimensions l_1, a_1, and R_1 of the nanoshell and to calculate its surface density $\rho_1 = \frac{m_1}{l_1 a_1}$;

(3) to determine the characteristics $\omega_1^{(2)}$, D_2, ρ_2, and R_2 of a compared macroscopic helical shell with the same dimensionless parameters α, $\frac{l}{R}$, and $\frac{a}{R}$ and the same fixation conditions as those of the nanoshell under study;

(4) to calculate the bending stiffness of the nanoshell D_1 using formula (22).

We note that the proposed approach to the experimental determination of bending stiffness does not require the determination of nanoshell thickness [8, 9].

ACKNOWLEDGMENTS

This work was supported by the Russian Foundation for Basic Research, project nos. 02-01-00514 and 03-01-00721.

REFERENCES

1. S. V. Golod, V. Ya. Prinz, V. I. Mashanov, and A. K. Gutakovsky, Semicond. Sci. Technol. **16**, 181 (2001).
2. A. B. Vorob'ev and V. Ya. Prinz, Semicond. Sci. Technol. **17**, 614 (2002).
3. V. Ya. Prinz, Izv. Vyssh. Uchebn. Zaved., Fiz., No. 6, 35 (2003).
4. V. Ya. Prinz, Microelectron. Eng. **69** (2/4), 466 (2003).
5. Yu. A. Ustinov, *Saint-Venant Problem for Pseudocylinders* (Nauka, Moscow, 2003) [in Russian].
6. A. P. Zhilin, in *Proceedings of Leningrad Polytechnic Institute* (Leningrad, 1982), Vol. 386, pp. 29–46 [in Russian].
7. Kh. Al'tenbakh and P. A. Zhilin, Adv. Mech., No. 4, 107 (1988).
8. A. M. Krivtsov and N. F. Morozov, Dokl. Akad. Nauk **381** (3), 825 (2001).
9. E. A. Ivanova, A. M. Krivtsov, and N. F. Morozov, Dokl. Akad. Nauk **385** (4), 494 (2002) [Dokl. Phys. **47**, 620 (2002)].

Translated by M. Lebedev

Doklady Physics, Vol. 50, No. 2, 2005, pp. 88–90. Translated from Doklady Akademii Nauk, Vol. 400, No. 4, 2005, pp. 480–482.

MECHANICS

Effect of Anomalous Melting Points upon Impact Loading

Yu. V. Petrov* and E. V. Sitnikova

Presented by Academician N.F. Morozov July 26, 2004

Received August 20, 2004

The spallation fracture of samples of polycrystalline aluminum and aluminum single crystals was experimentally studied at various temperatures in [1]. Analysis of experimental data for polycrystalline aluminum shows that resistance to tensile fracture varies only slightly when temperatures increase from room temperature to a value of 90% of the melting temperature and decreases abruptly to zero with a further increase in temperature. Experiments with aluminum single crystals reveal the effect of anomalously high temperatures: a conservation of high strength was observed in a state in which melting upon tension was expected. In this work, the effects of temperature anomalies discovered in [1] are analyzed for impact loading of materials. An analytical expression for the temperature dependence of the spallation strength of materials has been derived on the basis of the criterion for fracture incubation period. We introduce a new melting criterion relating phase-transition time to melting incubation period, which makes it possible to naturally explain the anomalous temperature effect upon impact loading.

TEMPERATURE DEPENDENCE OF SPALLATION STRENGTH

The time dependence of the impulse strength of materials can be obtained on the basis of the incubation period criterion [2–4]. For spallation fracture, this criterion has the form

$$\int_{t-\tau}^{t} \sigma(t')dt' \le \sigma_s \tau, \qquad (1)$$

where $\sigma(t)$ is the time dependence of the local stress at the fracture point, σ_s is the static strength of fracture, and τ is the fracture incubation period for a material, which may depend on temperature.

The measurements reported in [1] were conducted under conditions in which samples were acted upon by plane shock waves, which were generated in the samples under investigation by impact with an aluminum plate. For the given ratio of the thicknesses of a hammer and a sample, the shape of wave profiles was close to triangular. The problem of the reflection of a triangular compressing-stress pulse from the free end of a semi-infinite rod was analyzed in [2]. The equations that are derived using criterion (1) and that describe the time dependence of strength over the entire range of loading durations with allowance for the fracture incubation period have the form

$$P_* = \begin{cases} \dfrac{2\sigma_s\tau(T)}{t_i}, & t_i \le \tau(T), \\ \dfrac{\sigma_s}{1-\dfrac{\tau(T)}{2t_i}}, & t_i \ge \tau(T), \end{cases} \qquad (2)$$

where P_* is the threshold amplitude of the initial stress pulse and t_i is its duration.

In [5], an analytical expression was obtained for the temperature dependence of the fracture incubation period and it was shown that the incubation period can be expressed in terms of the parameters of kinetic strength theory [6]. We consider the temperature dependence of the fracture incubation period in the form

$$\tau = \tau_0 \frac{G}{kT}, \qquad (3)$$

where $k = 1.3807 \times 10^{-23}$ J/K is the Boltzmann constant, T is temperature, and $\tau_0 = 10^{-13}$ s is the period of the valence atomic vibrations in a solid. As is known, kT is the energy of the vibrational degree of freedom in the equilibrium state. This energy is necessary for breaking of an elementary bond, i.e., a bond between two atoms. The quantity G should be treated as an elementary portion of energy necessary for breaking the structural cell.

We assume that the fracture incubation period τ in expressions (2) for the time dependence of strength depends on temperature T according to law (3) and apply this result to analyze experimental data obtained in [1]. In the experiments reported in [1], the action was

Faculty of Mathematics and Mechanics, St. Petersburg State University, Universitetskiĭ pr. 28, Petrodvorets, St. Petersburg, 198504 Russia

** e-mail: yp@yp1004.spb.edu*

1028-3358/05/5002-0088$26.00

a triangular pulse, and the pulse duration t_i was the same for all test temperatures and was equal to 0.12 μs. Tests were carried out in a temperature range of 15 to 650°C, which is only 10°C lower than the melting point. For each material, we select the elementary energy of cell breaking G such that the threshold amplitudes for minimum testing temperature (15°C) correspond to the experiments in [1]. In this case, formula (3) yields a corresponding fracture incubation period of 0.137 and 0.75 μs for single crystals and polycrystals, respectively. Static strengths σ_s = 100 and 1000 MPa are used in the calculations for polycrystalline aluminum and single crystals, respectively.

The figure shows the temperature dependences of spallation strength calculated for aluminum single crystals and polycrystalline aluminum by formulas (2) and (3). Points are experimental data.

More accurate quantitative comparison of calculations can be carried out as soon as experimental data are accumulated and procedures of experiments and measurements are refined.

We note that the fracture incubation period for polycrystalline aluminum coincides with the value obtained in [5] for experimental data obtained in [7], where the brittle fracture of solids in a tensile stress wave was experimentally studied using the procedure of plane collisions between the hammer plate and target plate. Thus, the experiment described in [1] for polycrystalline aluminum at room temperature well agrees with classical experiments made at Ioffe Physicotechnical Institute [7] and is efficiently reproduced by incubation period theory.

ANOMALOUS TEMPERATURE EFFECT

In [1], tensile stresses at which material melting begins were estimated using the relation

$$p\alpha\frac{dT_m}{dp} - \frac{p}{K_T} = \alpha(T_0 - T_{m0}) - \frac{p}{K_S}, \qquad (4)$$

where the derivative $\frac{dT_m}{dp}$ represents the dependence of melting point T_m on pressure p, $\alpha = 1.12 \times 10^{-4}$ K^{-1} is the volume thermal expansion coefficient, T_{m0} = 933.2 K is the melting point at zero pressure, T_0 is the initial test temperature, and K_T = 56.7 GPa and K_S = 71.1 GPa are the isothermal and isentropic bulk elastic moduli of the material, respectively. This is a relation used in melting physics to determine the relations between temperature and pressure corresponding to the onset of melting. It corresponds to smooth (quasistatic) action and its application implies that body melting is treated as an instantaneous process.

Tensile stresses at which material melting begins were estimated in [1] using this relation for both materials. Experimental data for polycrystalline aluminum lie below this estimate. At the same time, experiments

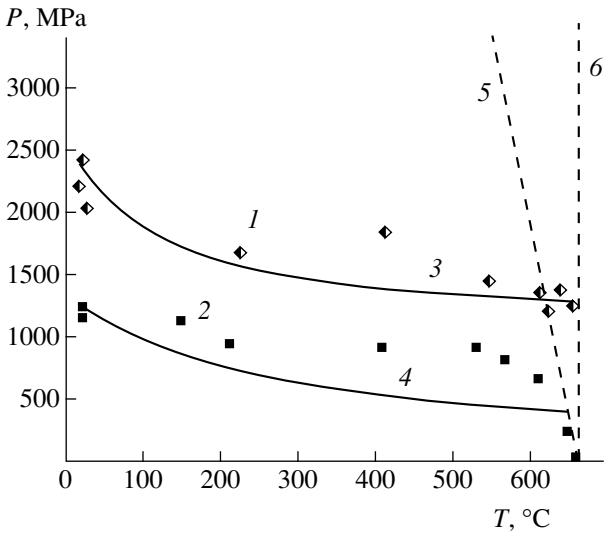

(Points *1* and *2*) Experimental data [1] and (lines *3* and *4*) calculations by formula (2) for the temperature dependence of the fracture threshold amplitude of a 0.12-μs pulse for aluminum single crystals and polycrystalline aluminum, respectively. Lines *5* and *6* are tensile stresses corresponding to the onset of melting as calculated by formulas (7) and (6), respectively.

with aluminum single crystals show that high strengths are present at the intersection of the calculated boundary of the melting region. To explain this effect, we introduce a new criterion corresponding to melting. We suppose that melting is not an instantaneous process and is characterized by its incubation period τ_m. Let us consider a melting criterion of the form

$$\int_{t-\tau_m}^{t} \sigma(s)ds \le P_m\tau_m, \qquad (5)$$

where P_m is the average ("equilibrium") stress that must be realized for the incubation period τ_m in order for the melting of material to occur. It corresponds to negative pressure determined from Eq. (4).

When inequality (5) takes the form of equality, the material melts and the corresponding temperature is defined as the melting point $T = T_m$. Solving the above problem for triangular wave stress pulses and using inequality (5) as a melting criterion, we express the dynamic threshold amplitudes P_{*melt} inducing melting in terms of the duration t_i, melting incubation period τ_m, and temperature T as

$$P_{*melt}(T) = \begin{cases} \dfrac{2P_m(T)\tau_m}{t_i}, & t_i < \tau_m, \\ \dfrac{P_m(T)}{1 - \dfrac{\tau_m}{2t_i}}, & t_i \ge \tau_m. \end{cases} \qquad (6)$$

As a specific case of the classical approach (when melting is treated as an instantaneous event), i.e., for $\tau_m = 0$, we have

$$P_{*\mathrm{melt}}(T) = P_m. \quad (7)$$

The temperature dependences of dynamic threshold amplitudes $P_{*\mathrm{melt}}$ inducing melting are shown in the figure as calculated by formulas (6) and (7) with $\tau_m = 0.7$ μs. To determine the conditions for the onset of melting for polycrystalline aluminum, the classical melting criterion in the form of Eq. (7) can be used, because, as is seen, experimental data for the strength of polycrystals near melting temperature approximately correspond to negative pressures obtained by this criterion and corresponding overheating is insignificant. High-temperature data for the strength of single crystals significantly exceed limiting stresses corresponding to the classical melting criterion, and the incubation period criterion (5) should be applied to determine the melting conditions in these cases.

As is seen, values that are calculated for aluminum single crystals using the model of melting incubation period (6) and corresponding to threshold fracture amplitudes are much larger than values predicted in classical melting model (7). The melting incubation period τ_m for aluminum single crystals was estimated using their overheating with respect to an estimate obtained using the classical criterion. This implies that the experiment provides the temperature at which the spallation strength of single crystals begins to abruptly decrease due to the onset of melting. According to the classical criterion, the difference between this temperature and melting onset temperature constitutes overheating for aluminum single crystals. An overheating of 30°C was presented in [1], and the melting incubation period taken above corresponds to this overheating.

Thus, the model developed above attributes the effect of a sharp decrease in strength near the melting point to the competition between two processes—fracture and melting—characterized by the corresponding incubation periods. It is possible to estimate pressure and temperature at which this transition occurs. This transition is determined as the intersection point of plots corresponding to these processes. The model of melting incubation period proposed in this work explains anomalously high melting points observed in the experiment with aluminum single crystals reported in [1].

REFERENCES

1. G. I. Kanel' and S. V. Razorenov, Fiz. Tverd. Tela (St. Petersburg) **43**, 839 (2001) [Phys. Solid State **43**, 871 (2001)].
2. Yu. V. Petrov, *Quantum Macromechanics of Dynamic Fracture of Solids* (IPMASh, St. Petersburg, 1996) [in Russian].
3. N. F. Morozov and Yu. V. Petrov, *Problems of the Fracture Mechanics of Solids* (S.-Peterb. Gos. Univ., St. Petersburg, 1997) [in Russian].
4. Yu. V. Petrov, Dokl. Akad. Nauk **395** (5), 621 (2004) [Dokl. Phys. **49**, 246 (2004)].
5. P. A. Glebovskiĭ and Yu. V. Petrov, Fiz. Tverd. Tela (St. Petersburg) **46**, 1021 (2004) [Phys. Solid State **46**, 1051 (2004)].
6. S. N. Zhurkov and S. A. Abbasov, Vysokomol. Soedin. **3** (3), 450 (1961).
7. É. N. Bellendir, Candidate's Dissertation in Mathematical Physics (Leningrad, 1990).

Translated by R. Tyapaev

Doklady Physics, Vol. 50, No. 2, 2005, pp. 91–94. Translated from Doklady Akademii Nauk, Vol. 400, No. 5, 2005, pp. 621–624.

MECHANICS

On the Method of Comparison in Asymptotic-Stability Problems

A. S. Andreev and O. A. Peregudova

Presented by Academician V.V. Rumyantsev May 3, 2004

Received September 16, 2004

We consider a set of ordinary differential equations

$$\dot{\mathbf{x}} = \mathbf{X}(t, \mathbf{x}), \quad \mathbf{X}(t, 0) \equiv 0, \tag{1}$$

where $\mathbf{x} \in R^n$, $\mathbf{X}(t, \mathbf{x}) = (X^1(t, \mathbf{x}), X^2(t, \mathbf{x}), \ldots, X^n(t, \mathbf{x}))^T$ is a vector function defined in the region $\Gamma = R^+ \times G = \{(t, \mathbf{x}): t \geq 0$, and $\|\mathbf{x}\| < \nu$, $\nu = \text{const} > 0$ or $\nu = +\infty\}$, $\|\cdot\|$ is a certain norm in R^n.

We suppose that the right-hand side of set (1) satisfies the Lipshitz condition over $\mathbf{x}$ uniformly with respect to t, i.e., for an arbitrary compact set $K \subset G$, there exists a number $L = L(K)$ such that for an arbitrary $\mathbf{x}_1, \mathbf{x}_2 \in K$ and an arbitrary $t \in R^+$, the inequality

$$\|\mathbf{X}(t, \mathbf{x}_1) - \mathbf{X}(t, \mathbf{x}_2)\| \leq L\|\mathbf{x}_1 - \mathbf{x}_2\| \tag{2}$$

holds true. Then, the family of shifts $\{\mathbf{X}_\tau(t, \mathbf{x}) = \mathbf{X}(t + \tau, \mathbf{x}), \tau \in R^+\}$ is precompact in a certain compact metric space $F_\mathbf{X}$ [1].

Definition 1 [1]. *As $t_j \longrightarrow +\infty$, the function $\mathbf{X}^*(t, \mathbf{x})$ defined by the relationship*

$$\mathbf{X}^*(t, \mathbf{x}) = \frac{d}{dt}\lim_{j \to \infty} \int_0^t \mathbf{X}_j(\tau, \mathbf{x})d\tau, \tag{3}$$

$$\mathbf{X}_j(\tau, \mathbf{x}) = \mathbf{X}(t_j + \tau, \mathbf{x}),$$

for arbitrary $\mathbf{x} \in G$ and $t \in R^+$ is called limiting with respect to $\mathbf{X}(t, \mathbf{x})$. The set of equations

$$\dot{\mathbf{x}} = \mathbf{X}^*(t, \mathbf{x}) \tag{4}$$

is called limiting with respect to initial set (1).

Thus, the entire family of limiting sets (4), where $\mathbf{X}^* \in F_\mathbf{X}$, corresponds to set (1). In this case, the positive limiting manifold $\omega^+(\mathbf{x}(t, t_0, \mathbf{x}_0))$ of the solution $\mathbf{x}(t, t_0, \mathbf{x}_0)$ to set (1) is quasi-invariant with respect to the family of sets (4).

We introduce a class $\mathbb{K}_1$ of vector functions $\mathbf{V}^T = (V^1, V^2, \ldots, V^k)$, $\mathbf{V}: \Gamma \to R^k$, R^k is a k-dimensional space of the norm $\|\cdot\|_k$. These functions are bounded and uniformly continuous for each manifold $R \times K$ in such a manner that for each arbitrary compact set $K \subset G$, there exists a number $m = m(K) > 0$, and for any arbitrary $\varepsilon > 0$, we can find a number $\delta = \delta(\varepsilon, K) > 0$ such that

$$\|\mathbf{V}(t, \mathbf{x})\|_k \leq m, \quad \|\mathbf{V}(t_2, \mathbf{x}_2) - \mathbf{V}(t_1, \mathbf{x}_1)\|_k < \varepsilon$$

for all $(t, \mathbf{x}) \in R \times K$, $(t_1, \mathbf{x}_1), (t_2, \mathbf{x}_2) \in R \times K$: $|t_2 - t_1| < \delta$, $\|\mathbf{x}_2 - \mathbf{x}_1\| < \delta$.

For each function $\mathbf{V} \in \mathbb{K}_1$, the family of shifts $\{\mathbf{V}_\tau(t, \mathbf{x}) = \mathbf{V}(t + \tau, \mathbf{x}), \tau \in R^+\}$ is precompact in a certain metrized space F_V of continuous functions $\mathbf{V}: \Gamma \to R^k$ with open compact topology [2]. Hence, it follows that for an arbitrary sequence $t_l \longrightarrow +\infty$, we can find both the sequence $t_{l_j} \longrightarrow +\infty$ and the function $\mathbf{V}^* \in F_V$ such that the sequence of shifts $\{\mathbf{V}_j(t, \mathbf{x}) = \mathbf{V}(t_{l_j} + t, \mathbf{x})\}$ will converge to $\mathbf{V}^*(t, x)$ in the space F_V, namely, the convergence will be uniform over $(t, \mathbf{x}) \in [-\beta, \beta] \times K$ for each number $\beta > 0$ and for each compact manifold $K \subset G$.

We now introduce similar classes $\mathbb{K}_2$ and $\mathbb{K}_3$ of vector functions $\mathbf{U}: R \times R^k \longrightarrow R^k$ and $\mathbf{W}: R \times G \times R^k \longrightarrow R^k$ bounded and uniformly continuous over $(t, \mathbf{u}) \in R \times K_2$ and $(t, \mathbf{x}, \mathbf{u}) \in R \times K_1 \times K_2$ for arbitrary compact manifolds $K_1 \subset G$ and $K_2 \subset R^k$.

Employing the uniformly differentiable Lyapunov vector function $\mathbf{V} \in \mathbb{K}_1$, $\mathbf{V} \in C^1$, we consider the problem of the stability of the zero solution to set (1).

With allowance for set (1), the derivative of this vector function can be represented in the form

$$\dot{\mathbf{V}}(t, \mathbf{x}) = \mathbf{U}(t, \mathbf{V}(t, \mathbf{x})) + \mathbf{W}(t, \mathbf{x}, \mathbf{V}(t, \mathbf{x})),$$
$$\mathbf{U}(t, 0) \equiv 0, \quad \mathbf{W}(t, \mathbf{x}, 0) \equiv 0, \tag{5}$$

where the function $\mathbf{U} = \mathbf{U}(t, \mathbf{u})$, $\mathbf{U} \in \mathbb{K}_2$ is quasi-monotonic and continuously differentiable with respect to

Ul'yanovsk State University, Ul'yanovsk, 432000 Russia
e-mail: AndreevAS@ulsu.ru; peregudovaoa@sv.ulsu.ru

1028-3358/05/5002-0091$26.00

$\mathbf{u} \in R^k$, $\dfrac{\partial \mathbf{U}}{\partial \mathbf{u}} \in \mathbb{K}_2$, and the function $\mathbf{W} \in \mathbb{K}_3$, $\mathbf{W}(t, \mathbf{x}, \mathbf{u}) \le 0$ for any arbitrary $(t, \mathbf{x}, \mathbf{u}) \in R \times G \times R^k$.

It follows from representation (5) that the function $\mathbf{V}(t, \mathbf{x})$ is the vector function of comparison, and the set

$$\dot{\mathbf{u}} = \mathbf{U}(t, \mathbf{u}) \tag{6}$$

is the set of comparison [3].

If $\mathbf{V} = \mathbf{V}(t, \mathbf{x})$ is the function satisfying Eq. (5), and $\mathbf{V}(t_0, \mathbf{x}_0) = \mathbf{V}_0$, and $\mathbf{u} = \mathbf{u}(t, t_0, \mathbf{V}_0)$ is the solution to set (6), which is defined within the interval $[t_0, t_0 + \beta)$, $\beta > 0$, then for all $t \in [t_0, t_0 + \beta)$, the solution $\mathbf{x} = \mathbf{x}(t, t_0, \mathbf{x}_0)$ to set (1) obeys the inequality

$$\mathbf{V}(t, \mathbf{x}(t, t_0, \mathbf{x}_0)) \le \mathbf{u}(t, t_0, \mathbf{V}_0).$$

From the condition $\mathbf{U} \in \mathbb{K}_2$, it follows that set (6) is precompact [2], and it is possible to define a family of limiting sets of comparison for this set:

$$\dot{\mathbf{u}} = \mathbf{U}^*(t, \mathbf{u}), \quad \mathbf{U}^* \in F_U. \tag{7}$$

From the conditions $\mathbf{U} = \mathbf{U}(t, \mathbf{u})$ related to the right-hand side of set (6), it follows that solutions $\mathbf{u} = \mathbf{u}(t, t_0, \mathbf{u}_0)$ to this set are continuously differentiable over $(t_0, \mathbf{u}_0) \in R^+ \times R^k$. From the property of a nondecrease in the dependence $\mathbf{u}(t, t_0, \mathbf{u}_0)$ as a function of $\mathbf{u}_0$ [3], it follows that the matrix

$$\Phi(t, t_0, \mathbf{u}_0) = \frac{\partial \mathbf{u}(t, t_0, \mathbf{u}_0)}{\partial \mathbf{u}_0}$$

is a nonnegative, normalized (i.e., $\Phi(t_0, t_0, \mathbf{u}_0) = I$, where I is the unit matrix), fundamental matrix for a linear system in variations

$$\dot{y} = H(t, t_0, \mathbf{u}_0)y, \quad H = \left.\frac{\partial \mathbf{U}(t, \mathbf{u})}{\partial \mathbf{u}}\right|_{\mathbf{u} = \mathbf{u}(t, t_0, \mathbf{u}_0)}.$$

We assume that for an arbitrary compact set $K \in R^k$, there exist numbers $M(K)$ and $\alpha(K) > 0$ such that the matrix Φ for arbitrary $(t, t_0, \mathbf{u}_0) \in R^+ \times R^+ \times K$ satisfies the conditions

$$\|\Phi(t, t_0, \mathbf{u}_0)\| \le M(K), \quad \det\Phi(t, t_0, \mathbf{u}_0) \ge \alpha(K). \tag{8}$$

Let $\mathbf{x} = \mathbf{x}(t, t_0, \mathbf{x}_0)$ be an arbitrary solution to set (1), which is bounded by the compact set $K_0 \subset G$, $\mathbf{x}(t, t_0, \mathbf{x}_0) \in K_0$ for all $t \ge t_0$.

We analyze the problem of localization of the positive limiting manifold $\omega^+(t_0, \mathbf{x}_0)$ for this solution under the assumption that the existence of the vector function $\mathbf{V}(t, \mathbf{x})$ satisfies equality (5). On the basis of Alekseev formula [4], it follows from equality (5) that the relation between the value $\mathbf{V}[t] = \mathbf{V}(t, \mathbf{x}[t]) = \mathbf{V}(t, \mathbf{x}(t, t_0, \mathbf{x}_0))$ of the function $\mathbf{V}(t, \mathbf{x})$ for the solution $\mathbf{x} = \mathbf{x}[t] = \mathbf{x}(t, t_0, \mathbf{x}_0)$ and the solution $\mathbf{u} = \mathbf{u}[t] = \mathbf{u}(t, t_0, \mathbf{V}_0)$, $\mathbf{V}_0 = \mathbf{V}(t_0, \mathbf{x}_0)$ to set of comparison (6):

$$\mathbf{V}(t, \mathbf{x}[t]) = \mathbf{u}[t] + \int_{t_0}^{t} \Phi(t, \tau, \mathbf{V}(\tau, \mathbf{x}[\tau]))\mathbf{W}(\tau, \mathbf{x}[\tau], \mathbf{V}(\tau, \mathbf{x}[\tau]))d\tau. \tag{9}$$

We assume that the function $\mathbf{V}(t, \mathbf{x})$ is bounded from below on the manifold $R^+ \times K_0$, and the solution $\mathbf{u}[t]$ of set (6) is bounded from above for all $t \ge t_0$. Then, as a corollary of condition (8) and equality (9), we can find the relationship

$$\lim_{t \to +\infty} \mathbf{W}(t, \mathbf{x}[t], \mathbf{V}(t, \mathbf{x}[t])) = 0. \tag{10}$$

Let $\mathbf{p} \in \omega^+(t_0, \mathbf{x}_0)$ be a limiting point defined by the sequence $t_j \longrightarrow +\infty$, $\mathbf{x}(t_j, t_0, \mathbf{x}_0) \longrightarrow p$ as $t_j \longrightarrow +\infty$. We choose a subsequence $t_{j_l} \longrightarrow +\infty$ for which there exist the corresponding convergences $\mathbf{X}(t_{j_l} + t, \mathbf{x}) \longrightarrow \mathbf{X}^*(t, \mathbf{x})$, $\mathbf{U}(t_{j_l} + t, \mathbf{x}) \longrightarrow \mathbf{U}^*(t, \mathbf{x})$, $\mathbf{W}(t_{j_l} + t, \mathbf{x}, \mathbf{u}) \longrightarrow \mathbf{W}^*(t, \mathbf{x}, \mathbf{u})$. From this, as in the case of the limit being passed in [1], we find that uniformly over $t \in [-\beta, \beta]$, the convergences

$$\mathbf{x}[t_{j_l} + t] \to \mathbf{x}^*[t], \quad \mathbf{u}[t_{j_l} + t] \to \mathbf{u}^*[t]$$

take place for an arbitrary $\beta > 0$. Here, $\mathbf{x}^*[t] = \mathbf{x}^*(t, 0, \mathbf{p})$, $\mathbf{u}^*[t] = \mathbf{u}^*(t, 0, \mathbf{u}_0^*)$, $\mathbf{u}_0^* = \mathbf{V}^*(0, \mathbf{p})$ is the corresponding solution to sets (4) and (7). In this case, using relationships (9) and (10) for all $t \in R$, we arrive at the equalities

$$\mathbf{V}^*(t, \mathbf{x}^*[t]) = \mathbf{u}^*[t], \quad \mathbf{W}^*(t, \mathbf{x}^*[t], \mathbf{V}^*[t]) = 0.$$

This is the basis for proving the following theorem.

Theorem 1. *We assume that* (I) *a certain solution* $\mathbf{x}(t, t_0, \mathbf{x}_0)$ *of set* (1) *is bounded by a some compact set* $K \subset G$ *for all* $t \ge t_0$, *and* (II) *there exists a certain Lyapunov function* $\mathbf{V} = \mathbf{V}(t, \mathbf{x})$, $\mathbf{V} \in \mathbb{K}_1$ *satisfying differential equality* (5), *the solution* $\mathbf{u}(t) = \mathbf{u}(t, t_0, \mathbf{V}_0)$, $\mathbf{V}_0 = \mathbf{V}(t_0, \mathbf{x}_0)$ *to set of comparison* (6) *being bounded for all* $t \ge t_0$ *and condition* (8) *being valid for this solution.*

Then, for an arbitrary limiting point $\mathbf{p} \in \omega^+(t_0, \mathbf{x}_0)$, *there is a set of limiting functions* $(\mathbf{X}^*, \mathbf{V}^*, \mathbf{U}^*, \mathbf{W}^*)$ *such that the solution* $\mathbf{x} = \mathbf{x}^*(t, \mathbf{p})$ *to set* (4) *with the initial condition* $\mathbf{x}^*(0, \mathbf{p}) = \mathbf{p}$, *satisfies the relationships* $\mathbf{x}^*(t, \mathbf{p}) \in \omega^+(t_0, \mathbf{x}_0)$, $\mathbf{x}^*(t, \mathbf{p}) \in \{\mathbf{V}^*(t, \mathbf{x}) = \mathbf{u}^*(t)\} \cap \{\mathbf{W}^*(t, \mathbf{x}, \mathbf{u}^*(t)) = 0\}$ *for all* $t \in R$, *where* $\mathbf{u}^*(t)$ *is the solution to limiting set of comparison* (7) *with the initial condition* $\mathbf{u}^*(0) = \mathbf{V}^*(0, \mathbf{p})$.

The theorem proved is the theorem on the localization of a positive limiting manifold based on the Lyapunov vector function and the set of comparison. This theorem develops the La Salle invariance principle formulated in [5] for an autonomous system and the quasi-invariance principle for a nonautonomous system

on the basis of the scalar Lyapunov function with the derivative of a constant sign [1].

We now define the scalar function $\bar{V} = \bar{V}(t, \mathbf{x})$:

$$\bar{V}(t, \mathbf{x}) = \sum_{i=1}^{k} V^i(t, \mathbf{x}).$$

Based on Theorem 1, we can obtain the following result developing the theorem on the asymptotic stability [3].

Theorem 2. *We assume that there exists a positive-definite Lyapunov vector function* $\mathbf{V} = \mathbf{V}(t, \mathbf{x})$, $\mathbf{V} \in \mathbb{K}_1$ *such that*:

(*I*) *differential equality* (5) *is valid*;

(*II*) *the zero solution* $\mathbf{u} = 0$ *to set of comparison* (6) *is stable (uniformly stable*);

(*III*) *for each bounded solution to set of comparison* (6), *condition* (8) *is fulfilled*;

(*IV*) *for arbitrary limiting totality* $\{\mathbf{X}^*, \mathbf{V}^*, \mathbf{U}^*, \mathbf{W}^*\}$ *and each bounded solution* $\mathbf{u} = \mathbf{u}^*(t) \neq 0$ *of limiting set of comparison* (7), *the manifold* $\{\mathbf{V}^*(t, \mathbf{x}) = \mathbf{u}^*(t)\} \cap \{\mathbf{W}^*(t, \mathbf{x}, \mathbf{u}^*(t)) = 0\}$ *does not contain the solution to limiting set* (4).

In this case, the zero solution $\mathbf{x} = 0$ to *set* (1) *is equi-asymptotically stable* (*uniformly asymptotically stable*).

Using the definition of [6], we can prove the following stability theorems for Lyapunov vector functions of a constant sign.

Theorem 3. *We assume that there exists a Lyapunov vector function* $\mathbf{V} = \mathbf{V}(t, \mathbf{x}) \geq 0$, $\mathbf{V} \in \mathbb{K}_1$ *such that the conditions* (*I*)–(*III*) *of Theorem* 2 *are fulfilled, as well as the condition*:

(*V*) *the zero solution* $\mathbf{x} = 0$ *is uniformly asymptotically stable with respect to both the manifold* $\{\bar{\mathbf{V}}^*(t, \mathbf{x}) = 0\}$ *and the family of limiting totalities* $\{(\mathbf{X}^*, \mathbf{V}^*, \mathbf{U}^*, \mathbf{W}^*)\}$.

Then, the solution $\mathbf{x} = 0$ *to set* (1) *is stable* (*uniformly stable*).

Theorem 4. *We suppose that in addition to the conditions of the preceding theorem, for arbitrary limiting pair* $(\mathbf{X}^*, \mathbf{W}^*)$, *the manifold* $\{\bar{\mathbf{V}}^*(t, \mathbf{x}) = c$: $c = c_0 = \text{const} > 0\} \cap \{\mathbf{W}^*(t, \mathbf{x}, \mathbf{u}^*(t)) = 0\}$ *does not contain solutions to set* (4).

In this case, the solution $\mathbf{x} = 0$ *of set* (1) *is* (*uniformly*) *asymptotically stable.*

We now consider a holonomic mechanical system that is described by n generalized coordinates $q_1, q_2, \ldots, q_n$ with the kinetic energy $2T = \dot{\mathbf{q}}^T A(\mathbf{q})\dot{\mathbf{q}}$. The system is subjected to both the action of potential forces with the potential energy $\Pi = \Pi(t, \mathbf{q})$, $\frac{\partial \Pi}{\partial \mathbf{q}} = 0$, for $\mathbf{q} = 0$ at all $t \in R^+$ and other generalized forces with the resultant force $\mathbf{Q} = \mathbf{Q}(t, \mathbf{q}, \dot{\mathbf{q}})$, $\mathbf{Q}(t, 0, 0) \equiv 0$.

The equations of motion for this system can be written out in the form of Lagrange equations

$$\frac{d}{dt}\left(\frac{\partial T}{\partial \dot{\mathbf{q}}}\right) - \frac{\partial T}{\partial \mathbf{q}} = -\frac{\partial \Pi}{\partial \mathbf{q}} + \mathbf{Q}. \tag{11}$$

We assume that these equations resolved with respect to $\ddot{\mathbf{q}}$ satisfy conditions (2) within the region $R^+ \times G_\varepsilon \times G_\varepsilon$, $G_\varepsilon = \{\mathbf{q}: \|\mathbf{q}\| < \varepsilon, \varepsilon > 0\}$, and that limiting equations (3), (4) can be composed for this region.

Theorem 5. *We assume that*

(*i*) $\Pi = \Pi(t, \mathbf{q})$ *has an isolated minimum* $\left\|\frac{\partial \Pi}{\partial \mathbf{q}}\right\| \geq \delta(\eta) > 0$ *at the point* $\mathbf{q} = 0$ *for all* $t \in R^+$ *and* $\mathbf{q} \in G_{\eta\varepsilon} = \{0 < \eta \leq \|\mathbf{q}\| < \varepsilon\}$;

(*ii*) *the combined action of all forces is such that for all* $(t, \mathbf{q}, \dot{\mathbf{q}}) \in R^+ \times G_\varepsilon \times G_\varepsilon$ *and* $(t, \dot{\mathbf{q}}) \in R^+ \times G_\varepsilon$ *the relations*

$$\frac{\partial \Pi}{\partial t}(t, \mathbf{q}) + \dot{\mathbf{q}}^T \mathbf{Q}(t, \mathbf{q}, \dot{\mathbf{q}}) \leq f(t, T + \Pi) + g(t, \dot{\mathbf{q}}),$$

$$g(t, \dot{\mathbf{q}}) \leq 0; \quad |g(t, \dot{\mathbf{q}})| \geq \delta(\eta) > 0$$

are correspondingly fulfilled;

(*iii*) *the zero solution of the scalar equation* $\dot{u} = f(t, u)$ *is stable.*

In this case, the equilibrium position $\dot{\mathbf{q}} = \mathbf{q}$ = *of system* (11) *is asymptotically stable.*

Let the generalized coordinates of mechanical system (11) be separated into positional and quasi-cyclic ones: $\mathbf{q} = (\mathbf{r}, \mathbf{z})$, $\mathbf{r} = (q_1, q_2, \ldots, q_k)^T$ and $\mathbf{z} = (z_1, z_2, \ldots, z_{n-k})^T = (q_{k+1}, q_{k+2}, \ldots, q_n)^T$ so that $\frac{\partial T}{\partial \mathbf{z}} \equiv 0$, $\frac{\partial \Pi}{\partial \mathbf{z}} \equiv 0$. The kinetic and potential energies and the resultant force of generalized forces of the system, are represented in the form

$$2T = \dot{\mathbf{r}}^T A(\mathbf{r})\dot{\mathbf{r}} + 2\dot{\mathbf{r}}^T B(\mathbf{r})\dot{\mathbf{z}} + \dot{\mathbf{z}}^T C(\mathbf{r})\dot{\mathbf{z}}, \quad \Pi = \Pi(t, \mathbf{r}),$$

$$\mathbf{Q} = (\mathbf{Q}^r, \mathbf{Q}^z), \quad \mathbf{Q}^r = \mathbf{Q}^r(t, \mathbf{r}, \dot{\mathbf{r}}), \quad \mathbf{Q}^z = \mathbf{Q}^z(t, \dot{\mathbf{z}}).$$

Then, the equations of motion of the system can be written as

$$\frac{d}{dt}\frac{\partial R}{\partial \dot{\mathbf{r}}} - \frac{\partial R}{\partial \mathbf{r}} = \mathbf{Q}^r, \quad \frac{d\mathbf{p}}{dt} = \mathbf{Q}^z, \quad \frac{d\mathbf{z}}{dt} = -\frac{\partial R}{\partial \mathbf{p}}, \tag{12}$$

where $R = R(t, \mathbf{r}, \dot{\mathbf{r}}, \mathbf{p}) = R_2 + R_1 - W$, $2R_2 = \dot{\mathbf{r}}^T F \dot{\mathbf{r}}$, $F = A - BC^{-1}B^T$, $R_1 = \mathbf{p}^T C^{-1} B^T \mathbf{r}$, and $W(t, \mathbf{r}, \mathbf{p}) = \Pi + 1/2\mathbf{p}^T C^{-1}\mathbf{p}$.

We assume that in the case of $\dot{\mathbf{r}} = \mathbf{r} = 0$, $\mathbf{p} = \mathbf{p}_0$, and $\dot{\mathbf{z}}_0 = C^{-1}(0)\mathbf{p}_0$, for all $t \in R^+$, the equalities $\frac{\partial W}{\partial \mathbf{p}} = 0$,

$\mathbf{Q}^r = \mathbf{Q}^z = 0$ are valid. Then the system has the steady-state motion

$$\mathbf{r} = 0, \quad \dot{\mathbf{r}} = 0, \quad \mathbf{p} = \mathbf{p}_0, \quad \dot{\mathbf{z}} = \dot{\mathbf{z}}_0 = C^{-1}(0)\mathbf{p}_0. \quad (13)$$

On the basis of Theorem 3, we can derive the following result on the stability of this solution.

Theorem 6. *We assume that*

(*i*) *for* $\mathbf{p} = \mathbf{p}_0$, *the function* $W(t, \mathbf{r}, \mathbf{p})$ *has an isolated minimum* $\left\|\frac{\partial W}{\partial \mathbf{r}}\right\| \geq \delta(\eta) > 0$ *at the point* $\mathbf{r} = 0$ *for all* $t \in R^+$ *and* $\mathbf{r} \in G_{\eta\varepsilon}$;

(*ii*) *the combined action of forces over positional coordinates is such that for* $\mathbf{p} = \mathbf{p}_0$, *for all* $(t, \mathbf{r}, \dot{\mathbf{r}}) \in R^+ \times G_\varepsilon \times G_\varepsilon$, $(t, \dot{\mathbf{r}}) \in R^+ \times G_{\eta\varepsilon}$ *the relations*

$$\frac{\partial W}{\partial t}(t, \mathbf{r}, \mathbf{p}_0) + \dot{\mathbf{r}}^T \mathbf{Q}^r(t, \mathbf{r}, \dot{\mathbf{r}}) \leq f^r(t, R_2 + W) + g(t, \dot{\mathbf{r}}),$$

$$g(t, \dot{\mathbf{r}}) \leq 0; \quad |g(t, \dot{\mathbf{r}})| \geq \delta(\eta) > 0$$

are correspondingly fulfilled;

(*iii*) *the action of forces over cyclic coordinates is such that for all* $t \in R^+$, $\mathbf{p} \in \{\|\mathbf{p} - \mathbf{p}_0\| < \varepsilon\}$, *the scalar* $Q_i^z(p_i - p_{i0}) \leq f_i^z(t, p - p_0)$, $(i = 1, 2, \ldots, n - k)$, *where* $\mathbf{f}^z = (f_1^z, f_2^z, \ldots, f_{n-k}^z)^T$ *is a quasi-monotonic function*;

(*iv*) *the zero solution to the scalar equation* $\dot{u} = f^r(t, u)$ *and of the vector equation of comparison* $\dot{\mathbf{u}} = \mathbf{f}^z(t, \mathbf{u})$ *is stable*.

Then, steady-state motion (13) *is stable with respect to* $\mathbf{r}$, $\dot{\mathbf{r}}$, $\dot{\mathbf{z}}$, *and is asymptotically stable over* $\mathbf{r}$, $\dot{\mathbf{r}}$ *with respect to motions corresponding to the unperturbed value* $\mathbf{p} = \mathbf{p}_0$.

Theorems 5 and 6 develop and complement the results of [6–11] on stability of the steady-state motion of mechanical systems.

ACKNOWLEDGMENTS

The work was supported by the Russian foundation for Basic Research, project no. 02-01-00877, and by the Council of the President of the Russian Federation for Support of Young Russian Scientists and Leading Scientific Schools, project no. NSh-2000.2003.1.

REFERENCES

1. A. S. Andreev, Prikl. Mat. Mekh. **48**, 225 (1984).
2. Z. Artstein, J. Different. Equations **23** (2), 216 (1977).
3. *Method of Lyapunov Vector Functions in Stability Theory*, Ed. by A. A. Voronov and V. M. Matrosov (Nauka, Moscow, 1987).
4. V. V. Rumyantsev and A. S. Oziraner, *Stability and Stabilization of Motion with Respect to a Part of Variables* (Nauka, Moscow, 1987).
5. J. P. La Salle and S. Lefshets, *Stability by the Direct Liapunov Method with Applications* (Academic, New York, 1961; Mir, Moscow, 1964).
6. A. S. Andreev and T. A. Boĭkova, Mekh. Tverd. Tela, No. 32, 109 (2002).
7. A. S. Andreev and K. Rizito, Prikl. Mat. Mekh. **66** (3), 339 (2002).
8. V. V. Rumyantsev, *On the Stability of Satellite Steady-State Motion* (Vychisl. Tsentr Akad. Nauk SSSR, Moscow, 1967).
9. A. V. Karapetyan and V. V. Rumyantsev, in *Appl. Mech. Soviet Reviews. Stability and Analytical Mechanics* (Hemisphere, New York, 1990), Vol. 1, p. 3.
10. A. V. Karapetyan, *Stability of Stationary Motions* (Editorial URSS, Moscow, 1998).
11. N. Roosh, P. Abets, and M. Lalois, *Direct Lyapunov Method in Stability Theory* (North-Holland, Amsterdam, 1975; Mir, Moscow, 1990).

Translated by G. Merzon

Doklady Physics, Vol. 50, No. 2, 2005, pp. 95–99. Translated from Doklady Akademii Nauk, Vol. 400, No. 5, 2005, pp. 625–629.

MECHANICS

Long-Term Variations in the Angular Velocity of Earth's Rotation

G. G. Denisov, V. V. Novikov, and A. E. Fedorov

Presented by Academician V.F. Zhuravlev May 6, 2004

Received May 6, 2004

It is now known [1, 2] that the angular velocity of the Earth's rotation varies over time; however, it was for a long time regarded as a constant, while day length was taken as a time standard. Following the discovery of the secular acceleration of the Moon by E. Halley in 1696, the constancy of the Earth's rotation velocity became doubtful. The physical causes of this behavior are tidal friction induced by the gravitational effect of the Moon and Sun on the rotation of the Earth, which cannot be treated as solid in this case; a moment acting on the Earth from moving air and liquid masses; the possible motion of masses inside the Earth, and, more precisely, in its core; etc.

In our opinion, significant advances occurred in the study of the mechanism of variation in the Earth's rotation velocity when (i) an atomic clock was built in 1955 that provided both for atomic time measurements that were more uniform than previous time measurements and for much more accurate measurements of day length; and when (ii) the advanced rotation of the solid core with respect to the mantle was discovered from the propagation of seismic waves in the Earth's depths [3].

Variations in day length for all the times of instrumental observation (the last 300 years) were presented in [4]. Analyzing these data, one can reliably separate a constant decrease rate for the Earth's rotation velocity, which corresponds to an increase in day length by 1.7×10^{-3} s per century [2]. This rate of decrease in the angular velocity of the Earth's rotation was first obtained by comparing times of known antique solar eclipses with times of these eclipses calculated with the constant present angular velocity. Data acquired after 1955 exhibit annual, and even seasonal, oscillations caused by the motion of air masses, melting of ice, and other seasonal factors.

At the same time, there are long-term variations in rotation velocity: the rotation velocity decreased for several decades and then increased for nearly the same period. These variations in angular velocity are much larger than 1.7×10^{-3} s per century.

Many hypotheses were proposed to explain these variations. Some of them are based on the angular-momentum exchange between the core and the mantle, which occurs upon changes either in the electromagnetic interaction between the core and the mantle [1] or in the viscosity of the liquid core [5].

In this work, we propose a simple mechanical model for explaining the above-mentioned long-term variations in the Earth's rotation and for estimating the characteristic parameters of the gravitational and viscous interaction between the mantle and the solid core. This model is based on the recently discovered differences in the angular velocities of the mantle and the core [3]. If the mantle and crust are treated as one rigid body in the form of a three-axial ellipsoid and the solid core is treated as another such body coaxially rotating about the principal axes with the maximum moment of inertia, then, in addition to viscous friction forces in the liquid core, the gravitational moment arises due to the asphericity of the solid-body density. This moment depends on the rotation angle between the bodies and twice changes sign upon the total relative rotation.

If I_1 and I_2 are the moments of inertia of the crust–mantle system and the core, respectively, and φ_1 and φ_2 are the respective rotation angles, the equations of rotational motion have the form

$$I_1\frac{d^2\varphi_1}{dt^2} = -h\frac{d}{dt}(\varphi_1-\varphi_2) - k\sin 2(\varphi_1-\varphi_2) - M,$$

$$I_2\frac{d^2\varphi_2}{dt^2} = -h\frac{d}{dt}(\varphi_2-\varphi_1) - k\sin 2(\varphi_2-\varphi_1).$$

In these equations, in addition to the moment M of the tidal friction forces, the moment of viscous friction forces with the coefficient h and the fundamental harmonic of the moment of the gravitational interaction between the mantle and solid core with the coefficient k are included. The gravitational moment will be esti-

Research Institute of Applied Mathematics and Cybernetics, Nizhni Novgorod State University,
ul. Ul'yanova 10, Nizhni Novgorod, 603005 Russia
e-mail: novikov@mm.unn.ru

1028-3358/05/5002-0095$26.00

mated below under the assumption that the mantle and core are coaxially rotating bodies with three-axial ellipsoids of inertia.

Introducing dimensionless parameters and time and combining equations, we arrive at the system

$$\begin{aligned} \ddot{\psi} + h'\dot{\psi} + 2k'\sin\psi &= 2m, \\ \ddot{\varphi}_1 + \gamma\ddot{\varphi}_2 &= -m. \end{aligned} \tag{1}$$

Here, the dot stands for the differentiation with respect to τ: $t = \tau t_*$, where t_* is the time scale,

$$\psi = 2(\varphi_1 - \varphi_1), \quad \gamma = \frac{I_2}{I_1}, \quad h' = \frac{h}{I_1}\left(1 + \frac{1}{\gamma}\right)t_*,$$

$$k' = \frac{k}{I_1}\left(I + \frac{1}{\gamma}\right)t_*, \quad m = \frac{M}{I_1}t_*^2.$$

The form of these equations enables one to solve them sequentially. The first equation is equivalent to the equation of a pendulum with a constant moment and belongs to equations with a cylindrical phase surface [6], because the state $(\dot{\psi}, \psi)$ coincides with the state $(\dot{\psi}, \psi \pm 2\pi n)$, where n is an integer.

Depending on the parameters h' and k' and the ratio between them, qualitatively different phase portraits of the system are realized. They are presented as a complete list in [6]. We are interested in the case $\frac{k'}{m} > 1$ for small h' values, when the first equation, in addition to the equilibrium state $k'\sin\psi_0 = m$, includes the stable limit cycle encircling the phase cylinder, which corresponds to the difference that was found in observations between the angular velocities of the solid core and the mantle. We seek this limiting cycle in the form

$$\psi = \omega\tau + \psi_1 + \psi_0.$$

The first equation then takes the form

$$\ddot{\psi}_1 + h'\dot{\psi}_1 + 2k'\sin(\omega\tau + \psi_0 + \psi_1) = 0, \quad \omega = \frac{2m}{h'}.$$

Since h' and k' are small, $\psi_1 \ll 1$, and for the estimate in which we are interested, it is sufficient to consider the equation

$$\ddot{\psi}_1 + h'\dot{\psi}_1 + 2k'\sin(\omega\tau + \psi_0) = 0,$$

which has the obvious solution

$$\dot{\psi}_1 = \frac{2k'}{\omega^2 + h'^2}[\omega\cos(\omega\tau + \psi_0) - h'\sin(\omega\tau + \psi_0)] \approx \frac{2k'}{\omega}\cos(\omega\tau + \psi_0).$$

We note that the latter relation is written under the condition $h' \ll \omega$.

As a result, system (1) reduces to the form

$$\dot{\psi} = 2(\dot{\varphi}_2 - \dot{\varphi}_1) = \omega + \frac{2k'}{\omega}\cos(\omega\tau + \psi_0),$$

$$\dot{\varphi}_1 + \gamma\dot{\varphi}_2 = -m\tau + c,$$

where c is the integration constant. Therefore, the angular velocity of mantle rotation as a function of time has the form

$$\dot{\varphi}_1 = \frac{1}{1+\gamma}\left\{c - \frac{\gamma}{2}\omega - m\tau - \frac{\gamma k'}{\omega}\cos(\omega\tau + \psi_0)\right\},$$

or, taking into account the initial conditions and that $\gamma \ll 1$,

$$\dot{\varphi}_1 = \dot{\varphi}_1^0 - m\tau + \frac{\gamma k'}{\omega}[\cos\psi_0 - \cos(\omega\tau + \psi_0)].$$

In terms of the initial parameters, this equation has the form

$$\omega_m - \omega_m^0 = \frac{M}{I_1}\left\{-t + \frac{k}{M}\frac{T_1}{2\pi}\left[\cos\psi_0 - \cos\left(\frac{2\pi}{T_1}t + \psi_0\right)\right]\right\}.$$

Thus, the angular velocity of mantle rotation decreases under the action of the moment of tidal forces at a constant rate of $\frac{M}{T_1}$ and oscillates with an amplitude of $\frac{k}{I_1}\frac{T_1}{2\pi}$, where $2T_1$ is the period of rotation of the Earth's solid core with respect to the mantle, which determines long-term variations in the Earth's rotation velocity.

Using known measurements [7] of the Earth's rotation velocity from 1955 to 2003, one can determine the parameters M, k, and T_1. According to these data, $T_1 \sim$ 60–70 yr. Moreover, taking 2003 as the beginning of time (so that $t < 0$) and taking into account the relation

$$\Delta\omega_m = -\frac{2\pi}{T_d^2}\Delta T_d,$$

where T_d is the day length, we obtain

$$\begin{aligned} \Delta T_d \times 10^3\ \text{s} &= 1.7 \cdot 10^{-2} t(\text{yr}) \\ &+ 1.36\left[\cos\left(360^\circ\frac{t}{T_1} + 173^\circ\right) - \cos 173^\circ\right] + 0.8. \end{aligned} \tag{2}$$

This expression has been obtained using the data $\Delta T_d(t=0) = 0.8 \times 10^{-3}$ s and $\Delta T_d(t = 30\ \text{yr}) = 3 \times 10^{-3}$ s. In this case, we obtain $k = 8.4M$. From the formulas for the dimensionless parameters and taking $t_* = 1$ yr = 3.15×10^7 s and $\gamma \sim 1/500$ (according to data on the Earth's structure; see, e.g., [2]) as a time scale, we obtain $h' \sim 0.87 \times 10^{-4}$, $k' \sim 0.019$, $m \sim 4.5 \times 10^{-6}$, and $\omega = 0.1$. Therefore, the conditions of the smallness of h' and k' and $h' \ll \omega$, which were used for the above estimates, are satisfied quite well.

Let us estimate the gravitational moment between the mantle and crust (which are treated as one rigid body in the form of a three-axial ellipsoid with an internal spherical cavity) and the inner core (another rigid body) located in the cavity of the first body.

The outer ellipsoid surface in the spherical coordinate system (r, φ, θ) is described by the expression

$$\frac{\cos^2\varphi_1\sin^2\theta_1}{a_1^2} + \frac{\sin^2\varphi_1\sin^2\theta_1}{b_1^2} + \frac{\cos^2\theta_1}{c_1^2} = \frac{1}{r_1^2}.$$

The solid core of the Earth is also a three-axial ellipsoid with the surface equation

$$\frac{\cos^2(\varphi_2-\sigma)\sin^2\theta_2}{a_2^2} + \frac{\sin^2(\varphi_2-\sigma)\sin^2\theta_2}{b_2^2} + \frac{\cos^2\theta_2}{c_2^2} = \frac{1}{r_2^2}, \quad c_{1,2} < a_{1,2} < b_{1,2}.$$

These bodies coaxially rotate about their principal axes with the maximum moments of inertia. The equations of the surfaces are written at the specific time when the angle between them is equal to $\varphi_2 - \varphi_1 = \sigma$.

We consider a case where the surfaces slightly differ from spherical shape:

$$\frac{c_1^2}{a_1^2} = 1 - 2\varepsilon_1, \quad \frac{c_1^2}{b_1^2} = 1 - 2\varepsilon_2 \quad (\varepsilon_1, \varepsilon_2 \ll 1),$$

$$\frac{c_2^2}{a_2^2} = 1 - 2\varepsilon_1', \quad \frac{c_2^2}{b_2^2} = 1 - 2\varepsilon_2' \quad (\varepsilon_1', \varepsilon_2' \ll 1).$$

In this case, it is easily seen that

$$r_1 \approx c_1 + c_1\sin^2\theta_1(\varepsilon_1\cos^2\varphi_1 + \varepsilon_2\sin^2\varphi_1),$$

$$r_2 \approx c_2 + c_2\sin^2\theta_2(\varepsilon_1'\cos^2(\varphi_1-\sigma) + \varepsilon_2'\sin^2(\varphi_1-\sigma)).$$

It is obvious that only the material points of the first body that lie between the ellipsoid surface and the sphere of radius c_1 or in the layer $\delta_1(\varphi_1, \theta_1) = r_1 - c_1$, as well as the points belonging to the layer $\delta_2(\varphi_2, \theta_2, \sigma) = r_2 - c_2$, contribute to the gravitational interaction between the bodies under consideration.

To simplify the calculation, since the layers are thin, we consider the interaction between two spheres of radii c_1 and c_2 with the surface densities $\rho_1\delta_1$ and $\rho_2\delta_2$ that is described by the elementary gravitational potential

$$dW = G\frac{\rho_1\delta_1 c_1^2\sin\theta_1 d\theta_1 d\varphi_1 \rho_2\delta_2 c_2^2\sin\theta_2 d\theta_2 d\varphi_2}{(c_1^2 + c_2^2 - 2c_1c_2\cos\alpha)^{1/2}},$$

where ρ_1 and ρ_2 are the volume densities and

$$\cos\alpha = \cos\theta_1\cos\theta_2 + \sin\theta_1\sin\theta_2\cos(\varphi_1 - \varphi_2).$$

The elementary moment is given by the expression

$$dM_{gr} = -(dW)_\sigma' = G\frac{\rho_1 c_1^3\sin^3\theta_1(\varepsilon_1\cos^2\varphi_1 + \varepsilon_2\sin^2\varphi_1)d\theta_1 d\varphi_1 \rho_2 c_2^3\sin^3\theta_2(\varepsilon_1' - \varepsilon_2')\sin(2(\varphi_2-\sigma))d\theta_2 d\varphi_2}{(c_1^2 + c_2^2 - 2c_1c_2\cos\alpha)^{1/2}}.$$

The integration with respect to θ_1, φ_1, θ_2, and φ_2 is significantly simplified for $c_2 \ll c_1$ and yields

$$M_{gr} = \frac{2}{5}\pi^2 G(\varepsilon_2' - \varepsilon_1')(\varepsilon_1 - \varepsilon_2)\sin(2\sigma)\rho_1\rho_2 c_2^5 = \frac{\pi^2}{10}G\rho_1\rho_2 c_2^5\left(\frac{c_2^2}{b_2^2} - \frac{c_2^2}{a_2^2}\right)\left(\frac{c_1^2}{a_1^2} - \frac{c_1^2}{b_1^2}\right)\sin 2(\varphi_2 - \varphi_1),$$

which provides for the estimate of the amplitude of the moment of the gravitational interaction between the solid core and the mantle (k value).

For the Earth, we have [2]

$$\frac{c_1^2}{a_1^2} - \frac{c_1^2}{b_1^2} = \frac{c_1^2}{a_1^2 b_1^2}(b_1^2 - a_1^2) \approx \frac{2(b_1 - a_1)}{c_1} = \frac{2 \times 213\ \text{m}}{6.36 \times 10^6\ \text{m}} = 6.7 \times 10^{-5}.$$

Assuming that the parameters of the core ellipsoid are approximately the same as for the mantle, i.e., $\frac{c_2^2}{a_2^2} - \frac{c_2^2}{b_2^2} = 6.7 \times 10^{-5}$, we obtain $k = 4.9 \times 10^{19}$ kg m^2 s^{-2}. We note

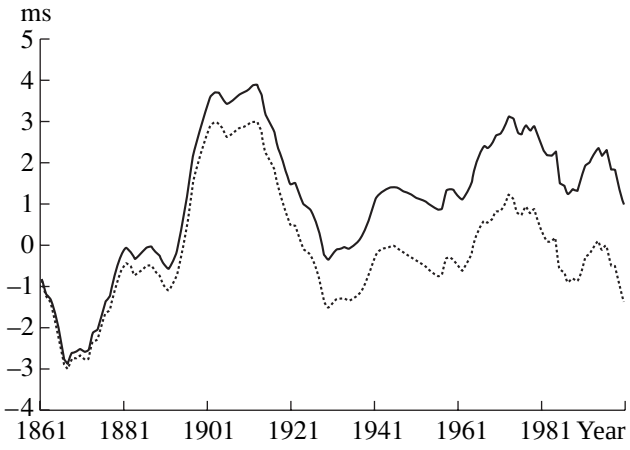

Fig. 1.

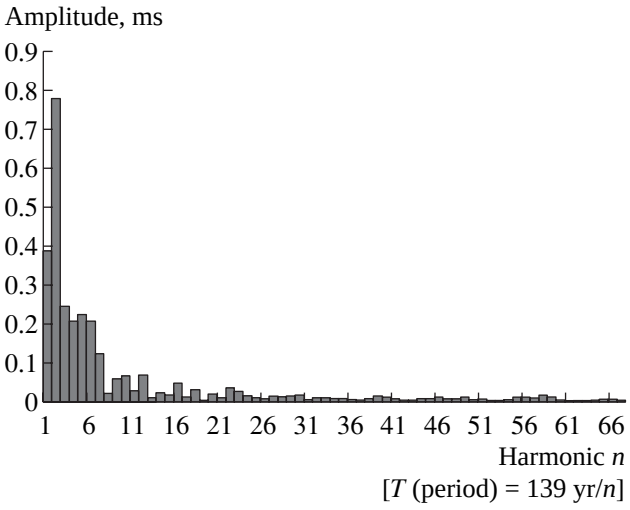

Fig. 2.

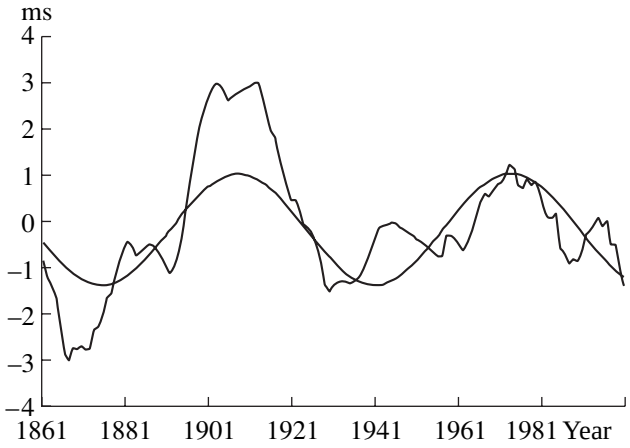

Fig. 3.

that $\frac{k}{M} = 3.8 \times 10^3$ for the tidal moment $M = 1.3 \times 10^{16}$ kg m^2 s^{-2} is much larger than the above ratio $\frac{k}{M}$.

Variation in day length for about one and a half centuries is shown in Fig. 1 (the upper line corresponds to data obtained from [7] and the lower line corresponds to those data minus a constant increase of 1.7×10^{-3} s per century in day length). Spectral analysis of these data (Fig. 2) shows that oscillations with periods of about 65 and 130 yr correspond to coefficients of 0.8 and 0.4, respectively. Contributions from other components are much smaller, which corroborates the validity of the assumption about the periodicity of variations. Figure 3 shows the superposition of the fundamental harmonic of day-length oscillations with a period of 65 yr and data on their variation for about 150 years. We emphasize the satisfactory coincidence of superposed data from the building of the atomic clock (1955) and the qualitative coincidence (coincidence of times of maxima and minima and absence of large discrepancies) in an earlier period, when measurements were not so accurate.

Discussion. The phenomenon of long-term variations in the angular velocity of Earth's rotation presents one of the most intricate and inexplicable problems. Indeed, for such a significant change (a change of $\sim\pm 3 \times 10^{-3}$ s in day length for the short time of 60–70 years) in the angular velocity of Earth's rotation, which displays such a huge moment of inertia, it is difficult to point to sources for a mechanical moment that is sufficiently large and changes sign. In view of this circumstance, information on the rotation of the solid core of the Earth with respect to the mantle enables one to point to such a moment based on the gravitational interaction between two bodies—the crust–mantle system and the solid core. Here, the solid core is treated as a powerful wheel and significant variations in mantle rotation are attributed to a change in its angular velocity.

The key point of the above mechanism is the estimation of the gravitational interaction between the mantle and the core, data on which are nearly absent. In this work, the spherical symmetry of the densities of bodies is proposed, and only the ellipsoid shape of their surfaces is taken into account. Data on the core ellipsoid are absent, and its shape is considered to be similar to that of the mantle. In spite of these and other crude assumptions, the estimate obtained for the gravitational interaction is three orders of magnitude larger than the moment necessary for explaining variation in the Earth's rotation. This fact indicates that this interaction is possible, although it can be caused by a significantly smaller asphericity of the core than that accepted in this work and by the general deviation of its density from a spherically symmetric distribution. The only important fact is the sinusoidal dependence of the gravitational moment on the angle between the bodies in the first

approximation for both the case of uniform aspherical bodies and the general case of inhomogeneous bodies.

If the above conclusions are corroborated by a more careful comparison of measurement data with calculations and longer observation of the Earth's rotation velocity, then (1) the rotation period of the solid core with respect to the mantle will be significantly refined (about 120 yr instead of 400 yr [3]); (2) the gravitational moment between the core and the mantle, as well as the periods of its maximum and corresponding stresses inside the Earth, which are sources of earthquakes, will be estimated (according to the estimate, this moment is eight times as large as the tidal moment); and (3) the concept of the solid core as a three-axial ellipsoid will appear and its moments of inertia will be estimated.

ACKNOWLEDGMENTS

This work was supported by the Russian Foundation for Basic Research, project no. 02-01-00921.

REFERENCES

1. W. Munk and G. Macdonald, *The Rotation of the Earth* (Cambridge Univ. Press, Cambridge, 1960; Mir, Moscow, 1964).
2. A. S. Monin, *Earth's Rotation and Climate* (Gidrometizdat, Leningrad, 1972) [in Russian].
3. X. Song and R. G. Richards, Nature **382** (6588), 221 (1996).
4. K. A. Kulikov, *Rotation of the Earth* (Nedra, Moscow, 1985) [in Russian].
5. G. G. Denisov and V. V. Novikov, Dokl. Akad. Nauk **362** (4), 484 (1998).
6. A. A. Andronov, A. A. Vitt, and S. E. Khaikin, *Theory of Oscillators* (Fizmatgiz, Moscow, 1959; Pergamon, Oxford, 1966).
7. http://hpiers.obspm.fr/eop-pc/earthor/ut1lod/lod-1623.html

Translated by R. Tyapaev